Submitted to Physical Review C

LBL-5820
Preprint

CENTRAL COLLISIONS OF RELATIVISTIC HEAVY IONS

J. Gosset, H. H. Gutbrod, W. G. Meyer,
A. M. Poskanzer, A. Sandoval, R. Stock, and
G. D. Westfall

May 10, 1977

Prepared for the U. S. Energy Research and
Development Administration under Contract W-7405-ENG-48

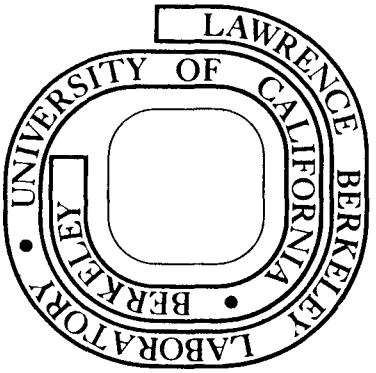

DISCLAIMER

CENTRAL COLLISIONS OF RELATIVISTIC HEAVY IONS*

J. Gosset,† H. H. Gutbrod, W. G. Meyer,
A. M. Poskanzer, A. Sandoval, R. Stock and G. D. Westfall

Lawrence Berkeley Laboratory, Berkeley, CA 94720
Gesellschaft für Schwerionenforschung, Darmstadt, Germany
Fachbereich Physik, Universität Marburg, Marburg, Germany

ABSTRACT

The energy spectra of protons and light nuclei produced by the interaction of ^{4}He and ^{20}Ne projectiles with Al and U targets have been investigated at incident energies ranging from 0.25 to 2.1 GeV per nucleon. Single fragment inclusive spectra have been obtained at angles between 25° and 150°, in the energy range from 30 to 150 MeV/nucleon. The multiplicity of intermediate and high energy charged particles was determined in coincidence with the measured fragments. In a separate study, fragment spectra were obtained in the evaporation energy range from ^{12}C and ^{20}Ne bombardment of uranium.

We observe structureless, exponentially decaying spectra throughout the range of studied fragment masses. There is evidence for two major classes of fragments; one with emission at intermediate temperature from a system moving slowly in the lab frame, and the other with high temperature emission from a system propagating at a velocity intermediate between target and projectile. The high energy proton spectra are fairly well reproduced by a nuclear fireball model based on simple geometrical, kinematical and statistical assumptions. Light cluster emission is also discussed in the framework of statistical models.

KEY WORDS

NUCLEAR REACTIONS U(^{20}Ne,X), E = 250 MeV/nucl.; U(^{20}Ne,X), U(α,X) E = 400 MeV/nucl.; U(^{20}Ne, X), Al (^{20}Ne,X), E = 2.1 GeV/nucl.; measured σ(E,θ), X = p,d,t, ^{3}He, ^{4}He. U(^{20}Ne,X), U(α,X), E = 400 MeV/nucl.; U(^{20}Ne,X), E = 2.1 GeV/nucl.; measured σ(E,θ), Li to O. U(^{20}Ne,X), U(^{12}C,X), E = 2.1 GeV/nucl.; measured σ(E,90°), ^{4}He to B. Nuclear Fireballs, Coalescence, Thermodynamics of light nuclei production.

I. INTRODUCTION

Previous experimental work[1-8] on high energy reactions between nuclei has established two qualitatively different types of events which have been associated with peripheral and near-central collisions. Peripheral reactions proceed with relatively small transfer of momentum and energy. Target and projectile nucleons maintain most of their initial state of longitudinal motion, corresponding to a final state with projectile fragments emitted into a narrow forward cone of laboratory angles, at a velocity near that of the projectile,[1,2,4] and with target "evaporation" fragments that are distributed almost isotropically over all of 4π, reflecting emission from a target residue that is slowly recoiling.[3] At incident energies of 2.1 GeV/nucleon the width of the projectile fragment cone is less than a few degrees, corresponding to transverse momenta near the Fermi momentum.[1,2] Target fragments show a relatively low multiplicity, with energies rarely exceeding about 30 MeV/nucleon.[3] Near-central collisions, however, lead to high energy fragments distributed over most of the forward hemisphere, with no clear-cut distinction as to their emission from target or projectile.[3,7,8] In addition to these fragments at intermediate energy, and to pions created in the reaction, there is a low energy component observed[3,6,8] in these "violent" processes which is more isotropically distributed over 4π. It may be attributed to decays of a target remnant that did not witness the violent primary interaction. Streamer chamber experiments at high incident energy reveal overall multiplicities of charged particles that are high, reaching up to the total number of initial charges plus a significant number of

created charged pions.[3,8] This high multiplicity indicates that an almost complete dissociation of both target and projectile is an event frequently associated with near-central impact.

It has been generally accepted that a high multiplicity of fragments and pions at large angles and intermediate energies may be used as a distinctive feature that allows one to select near central collisions of relativistic nuclei. These non-peripheral but not necessarily head-on collisions will henceforth be called central collisions. Our goal is to study such reactions, which lead to a complete diving of the projectile into target nuclear matter. The objective is to learn about nuclear matter during excitation and compression that take it far away from the familiar region of low temperature and normal nuclear density.

Two extreme concepts of the mechanism for the fast stage in a central collision are a superposition of nucleonic cascades[9-11] or the formation of an intermediate quasiequilibrated system.[6,12-14] In the former case the observable decay features would result from well known nucleon-nucleon cross sections folded with initial target and projectile ground state single particle distributions. This model might imply nucleon densities higher than the equilibrium density ρ_o, realized during the time scale of projectile traversal, which would merely result from independent particle motion. Alternatively, if the initial momenta are rapidly degraded and equilibrated over a sufficiently large volume of nuclear matter, one could justly speak about high density hadronic matter, ascribe a hadronic temperature to it, and apply hydrodynamic or thermodynamic models to describe the

time development and composition of the primary interaction region. In the framework of such models, the density has been calculated[13,15] to be two to six times ρ_o within the range of incident energies covered in the present study, which is from 0.25 to 2.1 GeV/nucleon corresponding to $0.6 \leq \beta \leq 0.95$ in the laboratory frame. The temperature may range up to about 120 MeV[15] which is in the domain where a significant fraction of the nucleons are excited to baryonic resonances, and where one might encounter effects due to the absolute limiting temperature of hadronic matter.[16]

There are several speculative ideas about the behavior of nuclear matter under such conditions to be tested in these reactions[17,18]; notably the prediction that the amount of correlation might <u>increase</u> due to first or second order phase transitions such as Lee-Wick type condensation or pion condensation, respectively.[19-24] These phenomena may be incorporated into the nuclear equation of state, and therefore be part of an appropriate hydrodynamical or statistical description of the events in relativistic heavy ion collisions.

Statistical thermodynamic concepts have been used to describe hadron-hadron and hadron-nucleus collisions at incident energies between 30 and 200 GeV.[16] These reactions produce an extremely high energy density and thereby involve an ensemble of states in the hadronic mass spectrum sufficiently large to make a statistical approach plausible. Heavy ion reactions at energies around one GeV/nucleon produce a moderate energy density in a <u>large</u> volume, thereby providing a set of intrinsic degrees of freedom which may again be large enough for thermalization to occur. Our study was, therefore, directed towards observable features

similar to the ones pertinent to collective and thermal features of hadron collisions, such as an increase in high transverse momentum production in the intermediate rapidity region.[25] A study of the fragments emitted into this region in nucleus-nucleus collisions should provide the data for testing models of the interaction mechanism.

This concept has led to a study of protons produced at angles between 25° and 150° in the laboratory, and at energies ranging from above the "evaporative" domain up to about 200 MeV/nucleon. The composite, light nuclear fragments ranging from deuterons up to oxygen nuclei were also studied. The ratios of their total cross sections might, in fact, give another clue as to the equilibration, temperature and nuclear density at the stage of emission.[26,27] Therefore, single fragment inclusive spectra and angular distributions were measured with counter telescopes. Previously, only studies with emulsions,[5] AgCl crystals[6] and plastic track detectors[28] existed. Various combinations of projectile (^{4}He, ^{20}Ne) and target nuclei (Al,U) were chosen in order to search for systematic effects of target size, number of nucleons participating in the localized region of primary interaction, etc. The selection of central collision events was achieved by measuring the associated multiplicity of high energy charged particles emitted at laboratory angles between 15° and 60° in coincidence with the detection of the fragments. Preliminary data have been presented elsewhere.[7,14,29]

II. EXPERIMENTAL TECHNIQUES

The basic layout of the experimental setup (Fig. 1) consisted of a particle telescope mounted on a movable arm inside a scattering chamber, a monitor telescope fixed at 90°, used to obtain the relative normalization, and an array of fifteen plastic scintillator paddles (tag counters) placed outside the scattering chamber, subtending the angles between 15° and 60° with respect to the beam direction, and about one-third of the azimuth. This array was used to determine the multiplicity of charged particles associated with each event. A fast coincidence was made between either the particle telescope or the monitor telescope, and the photomultiplier signal of any of the fifteen paddles. A bit was set for each scintillator that had detected a particle in coincidence. Each event was stored on magnetic tape in the event by event mode. On-line displays were available but the final analysis was performed off line.

Table 1 contains a summary of the experimental measurements made. The targets used consisted of foils of natural uranium (10 to 240 mg/cm^2), silver and aluminum (200 mg/cm^2). All targets were unbacked and supported at the edges by a 1 mg/cm^2 mylar film, attached to a large aluminum frame.

A. Detector Systems

In order to ease the discussion the fragment energy range measured will be divided into two regions: between 4 and 20 MeV/nucleon it will be referred to as the "low energy or evaporation region," and above 20 MeV/nucleon as the "high energy components." Reaction products from protons to He, and from Li to O will be called "light" and"heavy" fragments, respectively. To cover the measured spectrum

of masses and energies, three types of detector system were used.

1. Silicon-silicon telescope

For the isotopes from helium to beryllium in the low energy region, the detection system described in Ref. 30 was used, namely two ΔE-E silicon detector telescopes with thicknesses of (22 μm, 205 μm) and (177 μm, 1500 μm). With a solid angle of 2.5 to 5 msr, spectra were measured at 90° for 2.1 GeV/nucleon Ne and C beams averaging $0.5\text{-}1 \times 10^{7}$ particles per pulse incident on uranium.

The energy calibration was done as previously[31] by injecting a known amount of charge by means of a chopper pulser in the input stage of the detector preamplifiers and using the measured values of the ionization energy of silicon, ε = 3.67 eV/ion pair.[32] The energy spectra were corrected for the energy loss in half the target thickness and in the dead layers of the detectors.

2. Silicon-plastic scintillator telescope

The high energy components of the hydrogen and helium isotopes were measured with a ΔE-E telescope consisting of a 2 mm silicon ΔE detector and a 10 cm plastic scintillator E detector. The scintillator (Pilot B) was conically shaped with a 1 cm diameter front and a 2 cm diameter base. It was coupled to a 2.5 cm phototube. The anode signal of the phototube was processed with a 20 nsec fast linear gate and stretcher, yielding an energy resolution better than 5%. The subtended solid angle defined by the ΔE counter was 5 msr. A particle identifier spectrum of this telescope is shown in Fig. 2 a.

The energy of the particles, once identified according to their mass and charge, was obtained from their energy loss in the ΔE surface barrier detector, using the relation between energy loss and total energy. The energy ranges covered by this telescope for the different particles are given in Table 2. The protons and ^{3}He could be followed to higher than the punch-through energy in the plastic scintillator; however this extended energy range included some contamination from deuterons and ^{4}He, respectively.

3. Silicon-germanium telescope

The yields of the elements between Li and O above an energy of about 100 MeV were measured with a three element telescope. The telescope, as pictured in Fig. 3, consisted of twelve 180 μm thick Si crystals, backed by two 3 mm and two 8 mm thick Ge crystals. All 16 crystals were mounted in a cryogenic vacuum box which had a 25.4 μm havar entrance window. The 12 Si crystals were operated as 6 detectors by connecting in parallel each of the 6 crystals in the upper row with its neighbor in the lower row. Each pair had an active area of 10 mm × 34 mm, corresponding to a solid angle of 3 msr and an angular acceptance of 1.7°. Each set of 3 Si detector pairs was backed by both a 3 mm and an 8 mm Ge detector, each with an active area of 36 mm × 38 mm. This geometry yielded a detection system with a solid angle of 18 msr and a total angular acceptance of 12°. The energy ranges for various heavy fragments covered by this telescope are given in Table 2. Taking a narrow window in the total energy spectrum of ^{7}Be fragments the germanium resolution was found to be 2.3%, resulting in an overall energy resolution of 2.5%. A particle identification spectrum is shown in Fig. 2b.

4. Monitor telescopes

For the measurement of the He to B fragments in the low energy region only the 90° spectra were taken using two telescopes simultaneously, therefore no monitor was used.

In the measurement of the high energy hydrogen and helium isotopes a silicon-plastic scintillator monitor telescope was employed. The telescope was fixed at 90° and consisted of a 1 mm silicon ΔE detector and a 5 cm plastic scintillator E detector. It subtended a solid angle of 3 msr and monitored the high energy ^{4}He fragments.

For the measurement of the heavy fragments in the high energy region a conventional silicon ΔE-E telescope was used to monitor the low energy ^{4}He fragments in the evaporation peak (18 MeV to 30 MeV). The solid angle it subtended was 1 msr.

5. Tag counter array

The plastic scintillator paddles of the tag counter array were used to measure the associated multiplicity of the fragments detected by the telescopes. Each paddle was tapered, 2.5 cm at the tip, 7 cm at the base, 50 cm long and 3 mm thick. They were coupled with light pipes to 5 cm diameter phototubes (XP8575). Fifteen of these paddles placed side by side outside the scattering chamber covered the angles from 15° to 60° in θ, and 125° of azimuth, above the plane in which the telescope moved. The 9.5 mm thick aluminum dome of the scattering chamber served as an absorber for the particles detected in the scintillator array, giving a lower energy threshold of 20 MeV for pions, 47 MeV for protons and 220 MeV for alpha particles. The discriminator level was set at 0.5 MeV. The sensitivity of the tag counters to γ-rays was checked and found to be negligible.

B. Electronics

Two ΔE-E telescopes were simultaneously employed in all measurements. The telescopes were operated in a parallel fashion with the gated linear signals mixed before the ADC. A block diagram of the electronic configuration is shown in Fig. 4. A good event was defined by both a fast (≈ 15 nsec) ΔE-E coincidence (FC), and a slow coincidence between the ΔE and E single channel analyzers (SCA). Pile-up rejection (PUR) circuitry, with a pulse pair resolution of ≤ 100 nsec, was also employed. The Master gate for the system was defined as the coincidence between the valid output of the PUR and the SCA coincidence. The Master opened all linear gates, and gated the analogue particle identifier, the multiplexer (MPX), the ADC and the PDP8 computer.

The General Live Time of the system (detectors, electronics and MPX) was determined with analogue circuitry in the following manner. The FC signal was delayed an amount of time equal to its width and stretched in order to overlap the Master. The Master was stretched to overlap the MPX busy signal. A logical OR was made between these 3 signals and then used to anti the FC signal, thus yielding an "alive coincidence" only when the entire data acquisition system was ready to accept an event. This alive coincidence was then used to strobe the ΔE and E SCA's and to provide a 30 nsec wide gate for the 16-fold discriminator used to determine which tag counters fired in coincidence with the telescopes. The 16-fold discriminator was cleared with a reset signal which came at the trailing edge of the logical OR between the stretched signals.

The System Fractional Live Time was determined by sending a pulser triggered at a rate proportional to the beam intensity through the system and scaling the number of pulsers sent and the number of pulser events accepted by the computer. A tail pulse generator system was used for the solid state detectors, and for the plastic scintillators an avalanche pulser triggered red light emitting diodes (LED) which were mounted on the lucite light pipes which joined the plastic scintillators to the photomultiplier tubes. During each experiment both the linear tail pulse generator and the avalanche pulser were externally triggered by a set fraction ($\sim$ 1/20th) of the FC rate. Besides defining the Fractional Live Time of the system, the pulser also provided information concerning electronic gain shifts in the telescopes and enabled the monitoring of scintillator performance.

C. Data Reduction

The raw data were stored event by event on magnetic tape, each event consisting of eight parameters of 12 bits each. The detected particles were sorted according to their mass and charge by placing polygonal windows in either the ΔE-E or E_{total} - PI two dimensional projections. The energies were corrected for the energy loss in half the target thickness, and for any window or dead layer. After this, two-dimensional matrices were generated of the particle's energy vs. the associated m-fold coincidence number, so that the final data could be quickly extracted with any window on these two parameters. For the most forward and backward angles the target out background was measured and the data corrected for it.

For any kind of fragment in any energy window, one could extract from these matrices the histogram of the m-fold coincidence cross section, m being the number of tag counters in coincidence with the fragment. The raw m-fold coincidence histograms were corrected for accidentals and discriminator dead time in the tag counters. The correction was performed to the first order, assuming that the observed m-fold coincidences, with their corresponding probabilities P(m), come only from real n-fold coincidences, with probabilities $P_R(n)$, for which n differs from m by at most one unit (at most one counter fired accidentally or was dead),

$$P(m) = (N-m+1)\ p\ P_R(m-1) + P_R(m) + (m+1)\ q\ P_R(m+1). \qquad (1)$$

N is the total number of tag counters. The quantity p is the accidental probability in one counter, equal to the singles counting rate times the gate width (30 ns). The quantity q is the dead time probability in one counter, equal to the singles counting rate times the average dead time of the discriminator, taken to be 50 ns.

The validity of working only with first order corrections was checked in several experiments with the gate to the tag counters delayed by 100 ns. In these delayed coincidence experiments, mainly multiplicities 0 and 1 were observed, with very few accidental stars. The m-fold coincidence cross sections presented in the following sections will always be corrected for accidentals and dead time.

The m-fold coincidence distributions of charged particles, as measured with our 15 tag counters covering 125° of the azimuth for a total solid angle of 1.07 steradian, were then used to extract[33] the first moment <M> of the associated multiplicity M, corrected for multiple

firing of tag counters and for missing azimuthal solid angle between 15 and 60 degrees to the beam. Azimuthal symmetry of the fragment distribution was assumed, thereby neglecting possible kinematic correlations. The azimuthal efficiency Ω of a counter is then 1/15th of $125^{\circ}/360^{\circ}$, which is 0.023. According to Ref. 33, the m-fold coincidence probabilities can be expanded in terms of Ω as linear combinations of averaged binomial coefficients $\left\langle \binom{M}{j} \right\rangle$, namely

$$P_R(m) = (-)^{N+m} \binom{N}{m} \sum_j (-)^j \left\langle \binom{M}{j} \right\rangle \Omega^j \left[\sum_{x=1}^{N} (-)^x \binom{m}{N-x} x^j \right] . \quad (2)$$

This makes use of Eqs. (A.1) and (A.3) of Ref. 33 and neglects angular correlation effects. This triangular matrix relation ($j \geq m$) can easily be inverted and the products $\left\langle \binom{M}{j} \right\rangle \Omega^j$ expressed as linear combinations of measured $P_R(m)$. The first product is $\langle M \rangle \Omega$ and gives the average associated multiplicity $\langle M \rangle$. Higher moments were not useful because the tag array total solid angle was only a small fraction of 4π.

D. Normalizations

For the angular distributions the relative normalization was done through the number of counts in the monitor which was fixed at 90°. This procedure was compared to the normalization through the integrated beam current in an ionization chamber and both agreed within 10%.

The absolute normalization was based on the evaporation fragment cross sections for proton, deuteron and alpha induced reactions on uranium.[30,31] The ^{12}C and ^{20}Ne induced evaporation fragments were measured with the same setup that was used in the previous

measurements[30] and should be accurate to about 20%. It was assumed that the integrated beam current in the ionization chamber scales with the square of the atomic number of the projectile at the same velocity.

The high energy H - He and Li - O data were normalized by matching to the ^{4}He and ^{7}Be spectra, respectively, at 90° for ^{20}Ne + U at 2.1 GeV/nucleon. The extracted absolute cross sections should be accurate to about 35%. For the lower ^{20}Ne bombarding energies and for the ^{4}He induced reactions it was assumed that the ionization chamber response was proportional to the theoretical dE/dx of the beam particle.

III. EXPERIMENTAL RESULTS

A. Evaporation-like Fragments

Figure 5 shows the 90° energy spectra of He to Be isotopes in the low energy region for ^{20}Ne bombardment of U at 2.1 GeV/nucleon. These energy spectra show a Maxwellian shape with the peak position shifting towards higher energies as the atomic number of the fragment increases. For a given element, the most neutron deficient isotope displays a more prominent high energy component.[31] This trend is most obvious in Fig. 5 for ^{6}Li and ^{7}Be. It is also observed for the He isotopes (c.f. III.B).

Figure 6a summarizes the projectile dependence of the double differential cross sections for ^{4}He at 90°. The peak cross section increases by a factor of 4.8 from 5 GeV protons to Ne of 2.1 GeV/nucleon. Along with this there is a relative increase in the higher energy component, as seen[34] in Fig. 6b, reflecting higher apparent temperatures.

A Maxwellian fit to the spectra as done previously[30,31] indicates an apparent temperature of 15 MeV for ^{7}Li produced by ^{20}Ne ions, as compared to 10 MeV obtained with 5 GeV protons. Both the increased peak cross sections and the larger high energy components lead to much larger integrated cross sections as seen in Table 3. The integrations were done by graphical extrapolation of the 90° spectra to both higher and lower energies. In going from protons to Ne ions the ^{4}He yield increases a factor of 8 and the ^{7}Be yield a factor of 18. If one estimates the total ^{4}He yield by multiplying the 90° cross section by 4π, and divides by the total reaction cross section of 4.1 barn[35], one finds that there are about 7 alpha particles produced per interaction of 2.1 GeV/nucleon Ne ions with uranium. We do not observe these alpha particles in our multiplicity tag array because their low average energy does not permit them to penetrate the scattering chamber dome.

B. Hydrogen and Helium High Energy Components

The double differential cross sections were taken in two sets of measurements with different gains of the amplifiers, one for the hydrogen isotopes, the other one for tritons and the helium isotopes. The triton spectra were used to check the relative normalization of both sets of data as based on the monitor, and they were found to agree with each other, except for the case of ^{20}Ne on U at 2.1 GeV/nucleon where normalization problems make the proton absolute cross section uncertain by a factor of 2. However the triton and He isotope relative cross sections, as well as the relative proton cross sections at the lower energies, should be correct to 20%. It was found that due to the smaller cross section, the ^{6}He spectra did not have enough statistics to make the analysis meaningful.

All the high energy data for which we have isotope resolution will be presented with energy units of MeV per nucleon. The double differential cross sections of the observed fragments are presented for the ^{20}Ne irradiation on U at 2.1 GeV/nucleon in Fig. 7, at 400 MeV/nucleon in Fig. 8, at 250 MeV/nucleon in Fig. 9. Figure 10 shows the data for ^{4}He irradiation of U at 400 MeV/nucleon and Fig. 11 the data for ^{20}Ne on Al at 2.1 GeV/nucleon. These cross sections are single fragment inclusive as no multiplicity selection by means of the m-fold coincidence information, provided by the tag array, is used at this stage.

All the energy spectra are smooth and exponentially decaying with increasing energy, being flattest for the protons and becoming steeper as the mass of the fragment increases. For a given fragment the slope of the energy spectra rapidly increases with increasing angle, and the yield of each fragment decreases as the mass or charge of the fragment increases. A deviation from this general trend is observed in the vicinity of the evaporation region where the yield is higher for ^{4}He than for ^{3}He. In turn, ^{3}He exhibits a relatively more prominent high energy cross section. In this respect, the He isotope cross sections follow the trend of neutron deficient isotope cross sections, as described in the previous section.

The proton energy spectra from ^{20}Ne on U at forward angles are extremely flat in the measured energy range. It is surprising to find that the usual kinematical argument that would predict more forward peaked angular distributions the higher the bombarding energy does not apply. In fact the trend is opposite for all the fragments. This can be seen in Fig. 12 which shows the comparison of the ^{3}He spectra for

^{20}Ne on U at three bombarding energies for two angles, 30 and 90 degrees. At 30 degrees all three energy spectra have about the same cross section while at 90 degrees the cross sections increase with higher bombarding energy.

The angular distributions for the light fragments from ^{20}Ne on U at 400 MeV/nucleon integrated over a fixed velocity window from 30 to 50 MeV/nucleon are shown in Fig. 13. They are smooth and forward peaked, becoming steeper as the mass of the fragment increases. This same behavior is observed at all other incident energies.

Figure 14 shows the angular distributions of ^{3}He fragments for the different reactions integrated over two energy windows. In the 30 to 50 MeV/nucleon window for ^{20}Ne on U the highest yield is observed at 2.1 GeV/nucleon incident energy but the cross sections converge at forward angles as was discussed before. At the highest bombarding energy the cross section changes by less than an order of magnitude from 20 to 130 degrees, while for the 250 MeV/nucleon bombarding energy it changes by more than two orders of magnitude. Similar ^{3}He angular distributions are observed in the energy window from 50 to 100 MeV/nucleon. The overall features are the same but all slopes are steeper. In general, for fixed target, projectile and incident energy, the angular distributions of all fragments become more forward peaked the higher the energy window considered.

The cross sections for all the light fragments integrated over their respective measured energy ranges and angular domains are presented in Table 4. Table 5 compares, for all the reactions measured, the cross sections of the light fragments in the velocity window from

30 to 50 MeV/nucleon. The relative abundance of clusters among the fragments is high in this window. Towards higher fragment energies proton emission becomes more predominant. Comparing the proton and He isotope yields from ^{4}He and ^{20}Ne bombardment of U at 400 MeV/nucleon incident energy, both in Table 4 and Table 5, it is obvious that the lighter projectile produces a much smaller relative cross section for clusters. This effect is not merely due to the lower total incident energy of the ^{4}He projectile since the relative proton to cluster yields stay fairly constant in the ^{20}Ne + U reaction, as the energy increases.

C. Lithium to Oxygen High Energy Components

For the reactions ^{4}He on U at 400 MeV/nucleon, ^{20}Ne on U at 400 MeV/nucleon and 2.1 GeV/nucleon the fragments from Li to O were measured with the telescope shown in Fig. 3. Typical energy spectra obtained at 60° for the different fragments are shown in Fig. 15 for ^{20}Ne on U at 400 MeV/nucleon. The differential cross sections with their statistical errors are plotted vs. laboratory energy (not energy/nucleon). Due to dead layer effects between the second and third elements of the telescope (the 3 mm and 8 mm Ge) there is a distorted region in the Li and ^{7}Be spectra. We have verified that the cross section in this region agrees with a straight line interpolation between the undistorted extremes, and have shown this interpolation as a dashed line.

The double differential cross sections are shown in Figs. 16 to 18 for ^{20}Ne at 2.1 GeV/nucleon, 400 MeV/nucleon and ^{4}He at 400 MeV/nucleon, respectively. They have in common with the energy spectra of the hydrogen and helium isotopes, the same characteristic smooth

exponential decay which becomes steeper at backward angles. In contrast with the light fragment data there is much less dependence of the yield on the mass of the fragment. For the Ne + U reaction at two energies, again the data at the lower bombarding energy has a steeper, more forward peaked angular distribution with a leveling off at the most forward angles. In Fig. 19 we compare, for one reaction, the 90° energy spectra plotted vs. energy for all the fragments measured.

D. Associated Multiplicities

Besides the measurement of single fragment inclusive spectra, the level of m-fold coincidence of charged particles as detected by the fifteen-fold scintillator array was recorded for each telescope event. The resulting distributions of m-fold coincidence, associated with light fragments observed at 90°, are compared in Fig. 20 which shows smooth curves interpolating the histograms. In the left most part of the figure, the bombarding energy dependence is illustrated. For the lower energies, 250 MeV/nucleon and 400 MeV/nucleon, the m-fold coincidence distribution is Gaussian shaped, with its peak position shifting towards large m and the peak becoming wider as the energy increases. At the highest bombarding energies, the associated multiplicity is so high that the apparent multiplicity (i.e. the level m of coincidence) shows a saturation effect due to the limited number of counters. The fall-off of the apparent multiplicity distribution towards larger m is caused mainly by having two or more particles in one paddle and not being able to differentiate them. One can see, especially at the high bombarding energy, that the requirement of having a high energy fragment at a large angle implies that the average

associated multiplicity is large, considering that the tag array covers only 8% of 4π, which should imply that such fragments are predominantly produced in near central collisions. The central part of Fig. 20 shows the projectile dependence of the apparent multiplicity, dropping sharply from ^{20}Ne to ^{4}He. The target dependence is finally depicted on the right most side of Fig. 20; the apparent multiplicity for Al is substantially lower than for U.

A quantitative analysis of the trends in these m-fold coincidence distributions by means of eqs. (1) and (2) leads to the values <M> of the mean associated multiplicity given in Table 6. These values represent the mean real multiplicity of charged particles that are emitted into the full azimuth for $15^\circ \leq \theta \leq 60^\circ$, with energies above about 50 MeV/nucleon or above 20 MeV for $\pi^{\pm}$, and in coincidence with a certain energetic fragment, identified in the telescope at 90°. The values given for the light fragments (protons to ^{4}He) refer to measurements with the Si-plastic scintillator telescope; a small increase of <M> is observed with increasing fragment mass. The heavier fragments were recorded in the Si-Ge telescope which covered somewhat lower fragment velocities, or energies per nucleon (c.f. Table 2). The corresponding associated mean multiplicities are generally a little lower, because of a different setting of discriminators in these runs. Nevertheless, there is again a slight overall increase of <M> with fragment mass observed among the fragments from Li to N.

The effects on the m-fold coincidence distribution of the angular setting of the fragment telescope, i.e., the "trigger bias", is illustrated in Fig. 21. For three incident energies of the ^{20}Ne + U reaction,

all the events with a ^{3}He fragment in the telescope were selected, for various telescope angles. Cuts were applied to the corresponding m-fold coincidence distributions, thus further selecting events with high and low multiplicities, respectively. This was done for each angle, with the levels of the cuts fixed. The ratio of the resulting numbers of high/low multiplicity events is plotted vs. telescope angle in Fig. 21. At 250 and 400 MeV/nucleon incident energy this ratio increases with the angle, indicating an increasing bias towards high multiplicity events the more backwards the observed single ^{3}He fragment is emitted. This effect reflects the fact, also observed in streamer chamber experiments,[8] that large angle emission of energetic fragments increases with the overall multiplicity of an event. If the multiplicity increases with more central impact parameter it may be concluded that intermediate energy single fragment inclusive cross sections comprise more contributions from small impact parameter events, towards larger angles. Angular distributions are, therefore, less forward peaked if central collisions are selected. This was further confirmed by adding a 16th tag counter at 150°. By selecting events which fired this counter the m-fold coincidence distribution in the other 15 counters was shifted upwards by about 0.5 units for ^{20}Ne + U at 2.1 GeV/nucleon. At 2.1 GeV/nucleon incident energy, there is a maximum at about 80° observed in the plot of high/low multiplicity event frequency. One possible explanation is the location of the tag counters at relatively small angles, which may be depleted for events with fragment emission predominantly at larger angles.

The associated m-fold coincidence distributions for p, ^{3}He and ^{7}Be fragments from Ne + U at 0.4 and 2.1 GeV/nucleon are shown in Fig. 22. They exhibit little dependence on the mass of the observed fragment.

E. Summary of Qualitative Features of the Data

In order to ease the discussion the main characteristic features of the data may be summarized in the following way:

(1) All light fragment energy spectra are smooth except for an "evaporation peak" at very low energies.

(2) The most neutron deficient isotopes exhibit spectra with a relatively higher cross section in the high energy tail.

(3) The slope of the fragment spectra in the intermediate energy range gets steeper with increasing detection angle. Angular distributions are forward peaked.

(4) The double differential cross sections at 30° are approximately independent of the incident energy. At larger angles the yield increases and the slope decreases with increasing bombarding energy.

(5) The slope of the fragment spectra in energy/nucleon at a given angle gets steeper with increase in fragment mass.

(6) The total yields of light fragments fall off with increase in mass. At energies of 30-50 MeV/nucleon cluster emission comprises a significant fraction (about 50%) of the total baryonic cross section. Towards higher energies protons become predominant.

(7) Increasing the projectile mass at a fixed incident energy per nucleon leads to a small increase in the cross section

for low energy fragments but to a larger increase at high fragment energies, especially for the heavier clusters.

(8) In Ne bombardment of U and Al targets besides the difference in overall absolute cross section, one finds for Al a depletion of cross section at back angles.

(9) For all particles detected at angles between 20° and 160° the mean associated multiplicity is high and not changing remarkably with fragment mass or energy. This observation of high average multiplicities confirms the more limited finding of Jakobsson et. al.[5] that intermediate energy He fragments are mostly associated with large stars.

(10) The mean associated multiplicity increases with the projectile mass and with the target mass.

(11) Large angle emission of energetic fragments appears to be enhanced in high multiplicity events. However, due to the small number of tag counters, and the small solid angle they cover with respect to 4π, the present 15 tag counters are inefficient for a more detailed selection of high or low multiplicities.

IV. DISCUSSION

In this section we will discuss our results in terms of models for the reaction mechanism, as developed both for the emission of nucleons and clusters in central collisions of high energy nuclei. We will first discuss double differential single fragment inclusive cross sections, and finally turn to a re-examination of the apparent features of the reaction mechanism in terms of invariant cross section plots vs. total and transverse momentum, and rapidity.

Our present data focus on central collisions. Although the cross sections are single fragment inclusive, the domains of emission angle and fragment energy inherent in the detection system select against peripheral reaction fragments (c.f. III. D). The forward cone of projectile fragmentation[1-3] with $p_\perp \lesssim p_F$ is narrower than our smallest telescope angle even at our lowest bombarding energy. The average energy flux into the angular region of 15° to 60° accompanying the observation of a fast fragment with $\theta \geq 25^\circ$ is high. A lower estimate can be obtained from the mean associated multiplicities of charged particles (Table 6); at 400 MeV/nucleon ^{20}Ne + U, the average of about 10 charged fragments with E/nucleon $\gtrsim$ 50 MeV should be accompanied by about the same number of neutral particles. Neglecting pions, and taking into account the shape of the spectra measured at these angles one finds an average energy flux of at least 2 GeV. At 2.1 GeV/nucleon incident energy the corresponding number is at least 6 GeV. These average minimum energies of emission into $15^\circ \leq \theta \leq 60^\circ$ exceed, by far, the fluxes associated with peripheral reactions.[1-3] Light fragments at intermediate energy and large angles thus represent an abundant product of central collisions,[8] and single

fragment inclusive cross sections in this domain may be used to test theories of the reaction mechanism.

A. Nuclear Fireballs

Nucleon emission in the intermediate energy region from relativistic heavy ion induced reactions has been theoretically discussed in terms of several different models including hydrodynamics,[6,12,24] cascade models,[9,10] and classical microscopic scattering models.[11] Some of these have been applied to our ^{20}Ne + U data at 250 MeV/nucleon incident energy but no clear cut conclusions have been reached.[9,12] We have previously presented a simple macroscopic model involving statistical arguments and idealized geometrical concepts, which has been called the nuclear fireball model.[14] We shall further develop this model below and discuss its agreement with the data.

When a relativistic heavy ion projectile collides with a target nucleus there should be during a primary fast stage a localization of the interaction to the overlapping domain of target and projectile densities while the rest of the two nuclei remain relatively undisturbed. On a secondary time scale, dissipation of compressional and surface energy, as well as reabsorption of pions and nucleons emitted from the primary interaction region will excite these remnants, resulting in their subsequent decay that should be characterized by moderately low energies.[36,37] This idea leads to the separation of the nucleons in the system into participants and spectators[37,38] with respect to the time scale of the fast interaction stage. The nuclear fireball model deals only with the participant nucleons, i.e. it refers to a sub-set

of the emitted particles. The model assumes that the two nuclei sweep out cylindrical cuts through each other. The projectile participants are assumed to transfer all of their momentum to the effective center of mass system of all the participant nucleons forming a fireball which moves forward in the lab at a velocity intermediate between those of target and projectile. Its average internal kinetic energy per nucleon is much higher than the binding energy per nucleon. The participant nucleon fireball is then treated as an equilibrated non-rotating ideal gas characterized by a temperature, which expands isotropically in the center of mass of the fireball with a Maxwellian distribution in energy.

This model may be expected to reproduce the energy spectra and angular distributions of proton inclusive measurements in the intermediate velocity region, as well as proton multiplicity distributions. It has to be modified for incident energies above about 1 GeV/nucleon to include effects of isobar excitation and pion emission. The velocity regions near the target and projectile will contain contributions from spectator decay which are not treated by the fireball model. Also, the expanding fireball nucleons may in part coalesce to form clusters. We will return to this effect below (Sec. IV. D) but ignore it for the present. The model, at its simplest level, is formally described below.

B. Fireball Formalism

Assuming spherical nuclei, with radii equal to $1.2\ A^{1/3}$ fm, and straight trajectories, one can calculate as a function of impact parameter, b, the participant volume of each nucleus. One thus obtains the number of participant nucleons from the target and projectile, N_t and N_P respectively, by calculating the volume of intersections of a sphere and

a cylinder (See Appendix). This geometrical concept is illustrated in Fig. 23. The number of participating protons is found from

$$N_{proton}(b) = \sum_i \left(\frac{Z_i}{A_i}\right) N_i(b) \qquad i = t, p \tag{3}$$

where Z_i and A_i are the atomic number and mass number of the target or projectile. The quantities N_p/N_t and N_{proton} are shown as a function of impact parameter for Ne on U in Fig. 24.

One can calculate the velocity of the center of mass of the participant nucleons in the lab as

$$\beta_{cm} = \frac{P_{lab}}{E_{lab}} = \frac{N_p [t_i (t_i + 2m')]^{1/2}}{(N_p + N_t)\, m' + N_p t_i} \tag{4}$$

where P_{lab} is the momentum of the system in the lab, E_{lab} is the total energy(kinetic energy plus mass) of the system in the lab, t_i is the projectile incident kinetic energy per nucleon, and m' is the mass of a bound nucleon (taken to be 931 MeV). The total energy in the center of mass of the fireball is

$$E_{cm} = [E_{lab}^2 - P_{lab}^2]^{1/2} = [(N_p + N_t)^2 m'^2 + 2N_p N_t m' t_i]^{1/2} \tag{5}$$

If one assumes that there are a sufficient number of degrees of freedom in the fireball, and that there is a mechanism to randomize the available kinetic energy, one can define a temperature τ. Assuming a relativistic ideal gas of nucleons, τ can be expressed as[39]

$$\frac{E_{cm}}{(N_p+N_t)\,\tau} = 3 + \frac{m}{\tau}\frac{K_1\left(\frac{m}{\tau}\right)}{K_2\left(\frac{m}{\tau}\right)} \tag{6}$$

where K_1 and K_2 are MacDonald functions and m is the mass of a free nucleon (taken to be 939 MeV). The use of the free nucleon mass rather than the bound nucleon mass essentially subtracts the binding energy from the available kinetic energy. The available kinetic energy per nucleon in the center of mass, ε, is

$$\varepsilon = \frac{E_{cm}}{N_t + N_p} - m \tag{7}$$

The quantities β and ε are given as a function of impact parameter for 400 MeV/nucleon Ne + U in Fig. 25. The momentum distribution of the fireball nucleons in the center of mass is given by[39]

$$\frac{d^2N}{p^2dp\,d\Omega} = \frac{N}{4\pi m^3}\,\frac{e^{-E/\tau}}{2\left(\frac{\tau}{m}\right)^2 K_1\left(\frac{m}{\tau}\right) + \left(\frac{\tau}{m}\right) K_o\left(\frac{m}{\tau}\right)} \tag{8}$$

where p and E are the momentum and total energy respectively of a nucleon in the center of mass. The nonrelativistic expressions for the above quantities are

$$\varepsilon = \frac{3}{2}\tau \qquad (9)$$

and

$$\frac{d^2N}{p^2dp\ d\Omega} = N(2\pi m\tau)^{-3/2}\ e^{-p^2/2m\tau} \qquad (10)$$

The relativistic expressions (6) and (8) were used in the calculations presented in this paper. The difference between the temperature calculated relativistically and nonrelativstically is only of the order of a few percent for the 250 and 400 MeV/nucleon incident energy cases. However, the nonrelativistic distribution function is quite different from the relativistic one in our range of proton energies.

From the above quantities in the fireball center of mass, one obtains the energy distribution in the lab using

$$\frac{d^2N}{dEd\Omega} = pE' \frac{d^2N}{p'^2dp'd\Omega'} \qquad (11)$$

where $\frac{d^2N}{p'^2dp'd\Omega'}$ is the center of mass momentum distribution, p(p') is the nucleon lab (cm) momentum, and E' is the center of mass total energy of the nucleon expressed as

$$E' = \gamma_{cm}\ (E - \beta_{cm} p \cos\theta_{lab}) \qquad (12)$$

where

$$\gamma_{cm} = 1/\sqrt{1 - \beta_{cm}^2} \qquad (13)$$

Here E and θ_{lab} are the total energy and angle in the lab, respectively.

The final lab proton inclusive spectra are calculated by summing over impact parameter and weighting each impact parameter by $2\pi b$. In Fig. 24 the weight factor, $2\pi b\ N_{proton}$ is shown for Ne + U. Note that there is an impact parameter which has the maximum weight, b_{mw}, indicated by an arrow.

A good approximation to the full fireball model calculation involving the summation of energy spectra over all impact parameters can be obtained by using the distribution from Eq. (11), normalized to unity, to calculate the lab spectra taking β and τ at the b_{mw}. The over-all normalization is then

$$A_{norm} = \int_{o}^{R_t+R_p} 2\pi b\ N_{proton}(b)\ db. \qquad (14)$$

J. Hüfner and J. Knoll have recently pointed out to us that this is equal to $Z_t \pi R_p^2 + Z_p \pi R_t^2$.

For the case of equal mass target and projectile, β, τ, and the spectral form of $\frac{d^2N}{dEd\Omega}$ are independent of b. Thus the distribution function need only be calculated once for the unique β and τ and normalized by A_{norm} to obtain the fireball prediction. The quantities β and τ at b_{mw} for the target projectile incident energy combinations for which calculations are shown are given in Table 7. The angular momentum of the fireball is small and has been neglected. The maximum value is 30 $\hbar$ for the case of 400 MeV/nucleon ^{20}Ne on U.

The above formulations were applied in the 250 and 400 MeV/nucleon incident energy cases. However, in the case of 2.1 GeV/nucleon incident energy, the model had to be modified. The temperature in this case can no longer be related to the available kinetic energy through

the ideal gas formulation because of the creation of baryonic resonances. Using the method of Hagedorn,[40] this effect was taken into account in determining a modified temperature from the lower available kinetic energy.

C. Comparison of Fireball Model Predictions with the Data

The measured proton inclusive spectra are shown in Fig. 26 along with the results of the fireball model where the points indicate the data and the solid lines the calculations. The overall agreement is good at these incident energies of 250 and 400 MeV/nucleon. Note that the lower observed cross sections for the ^{4}He induced spectra are reproduced and that there are no adjustable parameters involved. The spectra at lower proton energies probably contain contributions from proton decay of the target spectator.

One can also imagine that at small impact parameters the projectile never penetrates through the target nucleus and the available kinetic energy is shared among all the projectile and target nucleons. This effect is exhibited by hydrodynamic calculations for head-on impact.[12] This "explosion" mechanism could account for a large part of the discrepancy at lower proton energies especially at backward angles. For head-on collisions a straightforward calculation using the mass numbers of the target and projectile instead of N_t and N_p in Eqs. (4) and (5) leads to β and τ for the explosion mechanism. For 400 MeV/nucleon Ne on U, $\beta = 0.076$ and $\tau = 13.5$ MeV for the entire system. Its fragments would, therefore, be found in the low energy parts of our spectra. For non-zero impact parameter, however, the compound system can have a large angular momentum which leads to a

decrease in temperature and introduces the decay pattern of a rotating system.

In the 2.1 GeV/nucleon Ne + U case the simple model, even including the excitation of baryonic resonances,[40] fails to reproduce the trend of the data.[14] This failure may be attributed to a breakdown of the assumed complete equilibration of projectile momentum in the fireball; at such a high incident energy there may be some persistence of longitudinal momentum.[14] Alternatively, or in addition, the decay products of the target spectator, which should be much more excited by pion absorption at 2.1 GeV/nucleon, might contribute significantly to the proton cross section over the entire measured energy range. This problem may be finally solved as data over a wider range of fragment energies become available.

The fireball model can also be used to calculate multiplicity distributions. The over all distribution of the proton multiplicity is

$$\frac{d\sigma}{dN_{proton}} = -2\pi b \left(\frac{dN_{proton}(b)}{db} \right)^{-1} \qquad (15)$$

where $\frac{d\sigma}{dN_{proton}}$ is the cross section per unit proton multiplicity. An example of such a calculation for Ne on U and Ne on Al is shown in Fig. 27. This "unbiased" distribution could be compared directly with streamer chamber data.[8] The bias implicit in our measurements of associated multiplicities can be incorporated by taking into account the probability of measuring a proton in the telescope which modifies Eq. (15) to read

$$\frac{d\sigma}{dN_{proton}} = - 2\pi b \, N_{proton}(b) \left(\frac{dN_{proton}(b)}{db} \right)^{-1} \quad . \qquad (16)$$

Also, the particle which triggered the telescope is accounted for by shifting the distribution down by one unit of multiplicity. The above distribution of the associated multiplicity of protons as calculated in the fireball model, without considering cluster formation, is shown in Fig. 28 (upper part) for Ne on U. In order to compare to the m-fold coincidence distribution observed in the tag counters (Fig. 20), one must take into account the statistical probability that several protons pass through one of the fifteen counters at the same time (c.f. II.D). Also, the efficiency of each counter must be known which is a function of the solid angle of each counter and the angular distribution of the emitted coincident protons. Finally, the lower energy cutoff due to the finite thickness of the dome through which the particles passed to reached the tag counters must be incorporated. Using the fireball model predictions for the angular distribution and the energy spectra of the coincident protons, the efficiency of each counter was calculated to be 0.0095 and 0.012 for 250 and 400 MeV/nucleon Ne on U, respectively. These efficiencies can be regarded as upper limits since the production of clusters (see next section) will lower the multiplicity. The efficiencies which reproduced the experimental distributions are 0.006 and 0.009 for 250 and 400 MeV/nucleon Ne on U respectively. The result of this calculation is shown in Fig. 28 (lower part), where the experimental and calculated distributions are normalized to unity. The agreement between the shapes of the calculated and experimental

curves is good. However, the m-fold coincidence distributions are relatively insensitive to the detailed shape of the associated multiplicity distribution. In order to gain more information about the shape of the distribution, more counters covering a larger fraction of the total solid angle are required.

D. Light Nuclei Emission

The first attempt to explain the emission of high energy light nuclei in relativistic heavy ion collisions was by final state interactions, or coalescence of emitted nucleons.[29] In this model, if any number of protons and neutrons corresponding to a bound nucleus are emitted in a reaction with momenta differing by less than a coalescence radius p_o, these nucleons are assumed to coalesce and form a nucleus.[41,42] The cross sections for the emission of light nuclei are then simply related to the cross sections for the emission of nucleons at the same momentum per nucleon, namely

$$\frac{d^2\sigma_A}{p^2 dp d\Omega} = \frac{1}{A!}\left(\frac{4\pi\, p_o^3\, \gamma}{3\sigma_o}\right)^{A-1}\left(\frac{d^2\sigma_1}{p^2 dp d\Omega}\right)^{A}. \qquad (17)$$

Both cross sections σ_A, for emission of a light nucleus formed with A nucleons, and σ_1, for emission of a single nucleon, are evaluated at the same momentum per nucleon p with Lorentz factor γ, and σ_o is the total reaction cross section. Our proton data have been used to calculate the light fragment cross sections from Eq. (17); the results have been compared with our experimental data,[29] the only adjustable parameter

being p_o. In Fig. 29 such a comparison is shown for d, t, ^{3}He and ^{4}He from the reactions of Ne on U at 250 and 400 MeV/nucleon, and the corresponding values of p_o are listed in Table 8. The agreement between this simple calculation and our data is rather impressive, the largest discrepancy being for ^{3}He fragments at the lowest energies and at forward angles. The values of the parameter p_o are remarkably uniform and of reasonable magnitude since they are smaller than the Fermi momenta of the clusters. It should be noticed that this simple phase space calculation does not explicitly include many factors, like spin and isospin couplings, integration over configuration space (not only momentum space) and time. All these factors are hidden in the p_o value. In Fig. 30 it is shown that a similar calculation leads to a similar agreement with our data for heavier fragments, namely the lithium isotopes (our data include all isotopes, but the calculation has been done assuming mass 6) and ^{7}Be, with a p_o of the same order of magnitude as that found from the light fragments. For the heaviest fragments, ^{9,10}Be to 0, the overlap between the energy per nucleon range of these data and the range of our proton data is too small to make useful comparisons.

The starting point for the derivation of Eq. (17) is the consideration of a coalescence sphere of radius p_o centered at a momentum per nucleon p_c. The a priori probability for finding one primary nucleon in this sphere is

$$P = \frac{4\pi\, p_o^3\, \gamma_c}{3\sigma_o \bar{M}} \frac{d^2\sigma(p_c)}{p^2 dp d\Omega} \quad , \tag{18}$$

where $\overline{M}$ is the average nucleon multiplicity. The probabilities for finding m primary nucleons inside this sphere are simply given by the binomial distribution

$$P_{\overline{M}}(m) = \binom{\overline{M}}{m} P^m \ (1-P)^{\overline{M}-m} \tag{19}$$

if kinematic phase space correlations can be neglected, which is always valid if $m \ll \overline{M}$, restricting the applicability of this approach to nuclear fragments small compared to the total multiplicity of the reaction. If P is small and $m \ll \overline{M}$, this binomial distribution becomes a Poisson distribution

$$P_{\overline{M}}(m) = \frac{(\overline{MP})^m}{m!} \exp(-\overline{MP}) \ . \tag{20}$$

If furthermore $\overline{MP}$ is small, this leads simply to Eq. (17). In fact for most of the data analyzed this way in Ref. 29, this last assumption is valid. But it is less valid at forward angles and small energy per nucleon. For example $\overline{MP}$ is about 0.52 for p_o = 120 MeV/c and p_c = 310 MeV/c (an energy of 50 MeV/nucleon), where $\frac{d^2\sigma}{dEd\Omega}$ = 80 mb/sr-MeV. For full consistency within this model the exponential factor in Eq. (20) should be taken into account, together with a sum rule stating that the total number of nucleons within the coalescence sphere is conserved. It is much more difficult to analyze our data this way since the exponential factor introduces a difference between the primary nucleon spectrum and the final nucleon spectrum obtained by depleting the primary one by the cross section for the light nuclei. For each value of p_o, a primary nucleon spectrum has to be guessed that can reproduce both nucleon and

light nuclei spectra. This procedure leads to smaller values of p_o than in Table 8 but the main effect is to destroy the simple dependence (Eq. 17) of light nuclei cross sections on nucleon cross sections, which has been shown to be approximately correct in Figs. 29 and 30.

Equation (17) says that the cross section in momentum space for emitting a light nucleus consisting of A nucleons is roughly proportional to the A^{th} power of the cross section for emitting a single nucleon at the same momentum per nucleon. This simple, experimentally verified result is by itself a strong indication in favor of the validity of an alternative, thermodynamic model for these relativistic heavy ion reactions, such as the nuclear fireball model, discussed previously to explain the proton inclusive double differential cross sections, and naturally extended to the emission of light nuclei in Refs. 26 and 27 through the use of a chemical potential.[43] In such a model the double differential cross section in momentum space for emitting any nucleus consisting of A nucleons decreases exponentially with the total kinetic energy E of the nucleus, like $\exp(-E/T)$ where T is the temperature. Hence with respect to the kinetic energy per nucleon E/A it behaves like

$$\left[\exp - \frac{E/A}{T}\right]^A \qquad (21)$$

which is proportional to the A^{th} power of the cross section for emitting a single nucleon at this energy per nucleon E/A. This thermodynamic model gives the same relation between single nucleon and light nuclei

cross sections as the coalescence model (Eq. 17) . But the problem occurring in the coalescence picture at large values of $\overline{MP}$ is avoided in the thermodynamic model since only the concentrations of various nuclear species in the total momentum space obey the laws of chemical equilibrium. At a given temperature only the yield of nucleons can be affected, but not the shape of their energy spectrum.

In fact the coalescence picture looks exactly like a thermodynamic model applied to a coalescence sphere in momentum space. But the coalescence spheres are not insulated from each other and, until the time of free expansion of the system, there can be a flow of nucleons and nuclei between them. Thus the number of nucleons inside a coalescence sphere need not be conserved, but only the total number of nucleons in the reaction, which suppresses the effect of the exponential term in Eq. (20).

There is interesting physical information in the thermodynamic model, since the yields of different nuclear species measured in relativistic heavy ion collisions can be used to obtain the fireball freeze-out density[26,27] ρ_F , namely the density below which the fireball expands freely.

When the density is small enough that quantum statistics effects can be neglected, and when the temperature is small enough that relativistic effects can be neglected, the chemical equilibrium formula can be written (following the formalism as outlined in Ref. 26) as

$$n(Z,N) = \frac{G(Z,N)}{2^A} A^{3/2} \exp\left[\frac{Q(Z,N)}{\tau}\right]\left[\frac{2\pi\hbar^2}{m_N\tau}\right]^{3(A-1)/2} [n(0,1)]^N [n(1,0)]^Z \qquad (22)$$

where $n(Z,N)$ is the concentration of nuclei consisting of Z protons and N neutrons ($A = Z+N$), $G(Z,N)$ their spin degeneracy, $Q(Z,N)$ their binding energy (positive if bound) and m_N the nucleon mass. If this equilibrium occurs at the freeze-out density ρ_F, the total number $\mathcal{N}(Z,N)$ of various nuclear species can be expressed as

$$\mathcal{N}(Z,N) = \frac{G(Z,N)}{2^A} A^{3/2} \exp\left[\frac{Q(Z,N)}{\tau}\right]\left[\left(\frac{2\pi\hbar^2}{m_N\tau}\right)^{3/2} \rho_F\right]^{A-1} \frac{\left[\mathcal{N}(0,1)\right]^N \left[\mathcal{N}(1,0)\right]^Z}{\left[\tilde{\mathcal{N}}(0,1) + \tilde{\mathcal{N}}(1,0)\right]^{A-1}} \qquad (23)$$

where $\tilde{\mathcal{N}}(0,1)$ and $\tilde{\mathcal{N}}(1,0)$ are respectively the numbers of neutrons and protons contained in the fireball.

From formulae (22) and (23) it is easy to draw qualitative conclusions about the effects of including light nuclei formation inside the nuclear fireball:

(1) Contrary to what occurs in stars where such an equilibrium takes place at a lower temperature, the exponential factor $\exp [Q(Z,N)/\tau]$ has little effect on the yields of various nuclear species, due to the high temperature of the fireball.

(2) In the nuclear fireball model the temperature is calculated at every impact parameter as a function of the total available kinetic energy in the fireball center of mass, which is itself calculated from geometrical and kinematical considerations. The treatment of composite nuclei in the fireball can only decrease the number of degrees of freedom, i.e. the available kinetic energy is shared between a smaller number of particles, and the temperature is increased from the values obtained for a nucleon system in the previous section. The higher the freeze-out density ρ_F, the larger the increase in the temperature.

(3) The dependence of $\mathcal{N}(Z,N)$ upon the impact parameter b is not the same as the dependence of the neutron and proton numbers, as can be seen from Eq. (23). For equal numbers of neutrons and protons the last ratio in Eq. (23) behaves approximately like the number of nucleons. At a constant freeze-out density ρ_F the number $\mathcal{N}(A)$ is thus proportional to $\mathcal{N}(1)\ \tau^{-3(A-1)/2}$. The weight factor $b\mathcal{N}(A)$ is thus peaked at smaller impact parameters than the nucleon weight factor, since the temperature is an increasing function of impact parameter when the projectile is smaller than the

target. Hence for a projectile smaller than the target, looking for fast light nuclei would bias the experiment more towards central collisions than looking for protons only.

A thermodynamic fit to the boron data from Ne on U at 400 MeV/nucleon is shown in Fig. 31. The temperature obtained is 27 MeV and the velocity 0.06c. This is close to the velocity 0.08c of the over-all center of mass system. It could mean that these fragments, in this energy range, are preferentially emitted in the most central collisions through the explosion mechanism described in Sec. IV.C. The temperature of 27 MeV is higher than the 13.5 MeV derived there for a gas consisting of nucleons only, which is the direction the temperature should go when composite particles are taken into account in the fireball.

In summary, both the coalescence and the thermodynamic pictures, with their appropriate modifications, may account for the overall features of cluster emission. The approach of the coalescence model is semi-empirical because it relates cluster cross sections to the initial distribution of nucleons in momentum space. It does not provide information as to the mechanism that leads to this initial distribution. However its success indicates that whatever the source of fragment emission, nucleons and light clusters at intermediate energy are correlated in momentum space. The thermodynamic model, on the other hand, involves more detailed physical features of the emitting source, i.e. its overall velocity, temperature, nucleon number, and density. Furthermore if there are several different sources, the model may be applied with different sets of parameters to each of the corresponding components in the decay cross sections. It is therefore not inconsistent within this model to

to describe light clusters at intermediate energies[26,27] with high τ and β, and heavier fragments at lower energies with low values of τ and β. Thus there is more information gained from the thermodynamic model, in particular about the behavior of an excited, dilute nuclear medium, at density close to the "freeze-out" density. A complete calculation with this model needs to be done and the results tested with all existing data.

E. Invariant Cross Section Plots

The single fragment inclusive double differential cross sections have been plotted vs. energy or energy per nucleon in the preceding sections. We turn now to relativistically invariant cross section plots in order to summarize the qualitative features of the data.

The invariant cross sections at 90° in the lab for all the observed fragments from ^{20}Ne on U at 400 MeV/nucleon are plotted in Fig. 32 against the total fragment momentum. A most probable mass number was assumed for the heavier fragments where the different isotopes were not resolved. All the segments in the plot, corresponding to all the observed fragments, line up with a remarkably uniform slope over the momentum range from 250 MeV/c to about 3 GeV/c. The inverse slopes are about 140 MeV/c.

Fragments from central collisions of relativistic heavy ions may originate from several qualitatively different subsystems of the overall decaying nuclear system, such as the fireball, the target spectators, or alternatively, an explosion of the fused target-projectile system. The detailed distribution of the longitudinal and transverse momenta of all the fragments created by the interaction may be therefore inspected in order to confirm the formation of the above mentioned

subsystems in the reaction. The distribution of longitudinal motion can be analyzed in terms of the rapidity variable $y=\frac{1}{2}\ln\left[(E+p_{\parallel})/(E-p_{\parallel})\right]$ where E and $p_{\parallel}$ are the total energy and longitudinal momentum of a particle. This rapidity variable is simply shifted by a constant value if expressed in a moving frame. Invariant cross section plots like the one shown in Fig. 32, for all the measured angles, were used to obtain contour lines of constant invariant cross section in the plane of rapidity versus transverse momentum per nucleon. Such contour plots are invariant with respect to Lorentz transformations, except for a shift of the rapidity axis. Two sets of contour plots are shown in Figs. 33 and 34.

In Fig. 33 the dependence of the cross section on y and $p_{\perp}$/nucleon is compared for protons, ^{4}He, ^{7}Be and carbon fragments from Ne on U at 400 MeV/nucleon incident energy. It is clear that these fragments are not emitted isotropically from one unique moving source, which would give contour lines all centered around the rapidity of that source. In a peripheral collision[1,2] the fragments from target and projectile would be represented by two steep "mountains" symmetric about the target and projectile rapidities. It is obvious from Fig. 33 that the present data do not cover the region of projectile fragmentation. Target fragmentation products may be part of the cross section only for the lowest values of $p_{\perp}$ and y. Most of our data thus represent fragments from non-peripheral collisions.

The maximum of the invariant cross section at a given level of $p_{\perp}$ occurs at increasing values of the rapidity for increasing $p_{\perp}$. Due to the shift of the contour lines towards intermediate rapidities with

wider spacing, there is clear indication in Fig. 33 for at least two qualitatively different sources participating in the fragment emission. One source is moving slowly in the lab with a rapidity smaller than about 0.1. It accounts for the emission both of protons and clusters at small transverse momenta, $p_\perp$/nucleon $\lesssim$ 250 MeV/c (explosion of the total target and projectile system and/or target spectator decay). The other source moves with a rapidity intermediate between those of the target and projectile (fireball), and its decay products extend towards higher transverse momenta, corresponding to the highest energy and momentum transfer between the target and the projectile.

The contour lines for different fragments exhibit a striking similarity. They all have nearly the same shape in the representation of Fig. 33. Independent of any model, this suggests that, in each kinematical region, all fragments originate from a common production mechanism. Furthermore, the spacings between the contour lines are approximately A times smaller for composite fragments of mass A than for protons. This is a simple graphic check of the cross section relations obtained in the coalescence or thermodynamic models (c.f. Sec. IV.D.).

The dependence of invariant cross section contours on the incident energy is illustrated in Fig. 34 for ^{3}He fragments from Ne on U at 0.25, 0.4 and 2.1 GeV/nucleon. As the energy increases, the contours extend towards higher transverse momenta, reflecting a higher transfer of energy and momentum between target and projectile. As the rapidity gap between target and projectile widens with the incident energy the decay products of a slowly moving source become more

discernible. At the lowest incident energy the narrow total rapidity gap prevents a clear cut distinction of emitting sources whereas, at 2.1 GeV/nucleon, the fireball rapidity of 0.65 falls into a well separated region of intermediate rapidities. However, it is apparent again from Fig. 34 that our data at this incident energy do not sufficiently cover this region; in fact the fireball model could only be tested in this case with data that do not represent the main contribution of fireball decay to the total cross section. More data are therefore needed at high fragment energy, in order to crucially test the participant-spectator model for collisions of relativistic heavy ions.

V. ACKNOWLEDGMENTS

We would like to acknowledge the help of R. G. Sextro who participated in one part of the data taking, and to P. J. Johansen who contributed to the theoretical developments. We would like to thank R. D. Edwards, G. Gabor, F. S. Goulding, E. E. Haller, D. A. Landis, D. F. Malone and J. T. Walton for their help in developing the experimental apparatus. We had stimulating communications with M. Gyulassy, A. Mekjian, W. D. Myers and W. J. Swiatecki. In particular we thank W. J. Swiatecki for allowing us to include his unpublished work in the appendix. We are grateful to H. A. Grunder and the Bevalac staff for their appreciable support.

APPENDIX. CALCULATION OF THE NUMBER OF PARTICIPANT NUCLEONS

The solution of the problem of calculating the number of participating nucleons of the target and projectile nuclei as a function of impact parameter involves the calculation of the volume of intersection of a sphere and a cylinder. The exact solution to this problem appears to require numerical integrations. This method was used for all the calculations reported in Ref. 14 and this paper. An approximate analytical method had been developed and used (but not described) in Ref. 36. The relevant formulae, based on Swiatecki's unpublished notes,[38] are given below.

The number of participant nucleons in a spherical nucleus of mass number A_1 and radius R_1, aimed with impact parameter b at a spherical nucleus of mass number A_2 and radius R_2 is given by

$$N_1 = A_1 F(\nu,\beta) \tag{A1}$$

where F is a function (given below) of the dimensionless parameter ν, specifying the relative sizes of the two nuclei and of the dimensionless variable β, specifying the impact parameter,

$$\nu = \frac{R_1}{R_1 + R_2} \tag{A2}$$

$$\beta = \frac{b}{R_1 + R_2}$$

The variables ν, β range from zero to one. These limits define a square with unit side in the space of ν and β, as illustrated in Fig. 35. The following are approximate formulae for F in the four sectors of the square indicated in Fig. 35 :

$$F_I = \left[1 - (1 - \mu^2)^{3/2}\right]\sqrt{1 - (\beta/\nu)^2}$$

$$F_{II} = \frac{3}{4}\sqrt{1-\nu}\left(\frac{1-\beta}{\nu}\right)^2 - \frac{1}{8}\left\{\frac{3\sqrt{1-\nu}}{\mu} - \frac{\left[1-(1-\mu^2)^{3/2}\right]\sqrt{1-(1-\mu)^2}}{\mu^3}\right\}\left(\frac{1-\beta}{\nu}\right)^3 \quad \text{(A3)}$$

$$F_{III} = \frac{3}{4}\sqrt{1-\nu}\left(\frac{1-\beta}{\nu}\right)^2 - \frac{1}{8}\{3\sqrt{1-\nu}-1\}\left(\frac{1-\beta}{\nu}\right)^3$$

$$F_{IV} = 1.$$

The abbreviation $\mu = \frac{1}{\nu} - 1 = \frac{R_2}{R_1}$ has been used. The four sectors correspond to the following situations:

I. A cylindrical hole is gouged in the nucleus A_1 (which is larger than A_2).

II. A cylindrical channel is gouged in A_1, with a radius smaller than that of A_1.

III. A cylindrical channel is gouged in A_1, with a radius larger than that of A_1.

IV. All of A_1 is obliterated by A_2 (whose radius is larger than that of A_1).

The above approximate expressions for F are based on solutions for a number of limiting situations when analytical expressions can be derived (e.g., close to the edges of the square in Fig. 35). The expressions for F in the four sectors of the square were chosen to insure continuity along the (dashed) boundaries of the sectors, but the derivatives are not always continuous. The dependence of F on the impact parameter is illustrated in Fig. 36 for several different relative sizes of the two nuclei.

The above formulae for F were tested in a number of cases against the (exact) numerical integrations. The inaccuracies in the results of the formulae occurred mainly at intermediate values of β, with the largest inaccuracy being 6% for $\beta = 0.4$, $\nu = 0.4$.

In discussing the fate of a spectator piece an important consideration is its excitation energy. The contribution to this energy arising from the fact that the shape of the spectator is not its equilibrium shape (assumed spherical) may be estimated by multiplying the nuclear surface-energy coefficient (about 0.9 - 0.95 MeV/fm^2) by its excess surface area. This excess is the area of the spectator immediately after the collision less the surface area of a sphere of equal volume. The excess surface area for spectator 1 is given approximately by the following formulae

$$\Delta(\text{Area}) = 4\pi R_1^2 \left(1 + P - (1 - F)^{2/3}\right) \qquad \text{(A4)}$$

where

$$P_I = \left(\frac{1}{\nu}\sqrt{1-\mu^2} - 1\right)\sqrt{1-(\beta-\nu)^2}$$

$$P_{II} = \frac{1}{8}\sqrt{\mu\nu}\left(\frac{1}{\mu} - 2\right)\left(\frac{1-\beta}{\nu}\right)^2 -$$

$$- \frac{1}{8}\left\{\frac{1}{2}\sqrt{\frac{\nu}{\mu}}\left(\frac{1}{\mu} - 2\right) - \frac{\left(\frac{1}{\nu}\sqrt{1-\mu^2} - 1\right)\sqrt{(2-\mu)\mu}}{\mu^3}\right\}\left(\frac{1-\beta}{\nu}\right)^3$$

$$P_{III} = \frac{1}{8}\sqrt{\mu\nu}\left(\frac{1}{\mu} - 2\right)\left(\frac{1-\beta}{\nu}\right)^2 - \qquad \text{(A5)}$$

$$- \frac{1}{8}\left\{\frac{1}{2}\sqrt{\mu\nu}\left(\frac{1}{\mu} - 2\right) + 1\right\}\left(\frac{1-\beta}{\nu}\right)^3$$

$$P_{IV} = -1 \quad .$$

These formulae were also obtained from the notes used in connection with Ref. 36. The method used was similar to that underlying the expressions for F. We do not have available a direct check of the surface-energy formulae against numerical integrations, so the above expressions should be used with some caution regarding their accuracy.

FOOTNOTES AND REFERENCES

* This work was done with support from the U. S. Energy Research and Development Administration and from the Bundesministerium fürForschung und Technologie, W. Germany.

† Permanent address: DPhN/ME, Centre d'Etudes Nucléaires de Saclay, 91190 Gif-sur-Yvette, France.

1. D. E. Greiner, P. J. Lindstrom, H. H. Heckman, B. Cork, and F. S. Bieser, Phys. Rev. Lett. 35, 152 (1975).

2. P. J. Lindstrom, D. E. Greiner, H. H. Heckman, B. Cork, and F. S. Bieser, LBL preprint 3650 (1975).

3. H. H. Heckman, D. E. Greiner, P. J. Lindstrom, and D. D. Tuttle, "An Atlas of Heavy Ion Fragmentation Topology", LBL preprint 1976, unpublished.

4. J. Papp, J. Jaros, L. Schroeder, J. Staples, H. Steiner, A. Wagner, and J. Wiss, Phys. Rev. Lett. 34, 601 (1975), and to be published.

5. R. Kullberg and I. Otterlund, Z. Phys. 259, 245 (1973).
B. Jakobsson, R. Kullberg, and I. Otterlund, Z. Phys. 268, 1 (1974), and Z. Phys. A272, 159 (1974).

6. H. G. Baumgardt, T. U. Schott, Y. Sakamoto, E. Schopper, H. Stöcker, J. Hofmann, W. Scheid, and W. Greiner, Z. Phys. A273, 359 (1975).

7. A. M. Poskanzer, R. G. Sextro, A. M. Zebelman, H. H. Gutbrod, A. Sandoval, and R. Stock, Phys. Rev. Lett. 35, 1701 (1975).

8. R. Poe, S. Fung, B. Gorn, A. Kernan, G. Kiernan, J. Lee, J. Ozawa, B. Shen, G. Van Dalin, L. Schroeder, and H. Steiner, to be published.

9. A. A. Amsden, J. N. Ginocchio, F. H. Harlow, J. R. Nix, M. Danos, E. C. Halbert, and R. K. Smith, Los Alamos preprint LA-UR-77-152, to be published.

10. J. P. Bondorf, S. Garpman, E. C. Halbert, and P. J. Siemens, to be published (1976).

11. A. R. Bodmer and C. N. Panos, Phys. Rev. C15, 1342 (1977).

12. A. A. Amsden, G. F. Bertsch, F. H. Harlow, and J. R. Nix, Phys. Rev. Letters 35, 905 (1975), and to be published.

13. M. I. Sobel, P. J. Siemens, J. P. Bondorf, and H. A. Bethe, Nucl. Phys. A251, 502 (1975).

14. G. D. Westfall, J. Gosset, P. J. Johansen, A. M. Poskanzer, W. G. Meyer, H. H. Gutbrod, A. Sandoval and R. Stock, Phys. Rev. Letters 37, 1202 (1976).

15. G. F. Chapline, M. H. Johnson, E. Teller, and M. S. Weiss, Phys. Rev. D8, 4302 (1973).

16. R. Hagedorn, Cargèse Lectures in Physics VI, E. Schatzman ed. (Gordon and Breach 1973) p. 643, and
A. T. Laasanen, C. Ezell, L. J. Gutay, W. N. Schreiner, P. Schübelin, L. von Lindern, and F. Turkot, Phys. Rev. Letters 38, 1 (1977).

17. R. Stock and A. M. Poskanzer, Comments on Nuclear and Particle Physics VII, No. 2, p. 41 (1977).

18. W. Greiner, in Proc. 2nd High Energy Heavy Ion Summer Study, L. Schroeder (ed.), p. 1, LBL-3675 (1975).

19. T. D. Lee and G. C. Wick, Phys. Rev. D9, 2291 (1974).

20. T. D. Lee, Rev. Mod. Phys. 47, 267 (1975).

21. A. R. Bodmer, Phys. Rev. D4, 1601 (1971).

22. A. B. Migdal, N. A. Kirichenko, and G. A. Sorokin, Phys. Rev. Letters 50B, 411 (1974).

23. M. Gyulassy, V. Ruck and W. Greiner, in Proceedings of the International Workshop IV, Hirschegg, Austria, 1976, p. 115 (T. H. Darmstadt Report AED-76-015-000), and to be published.

24. J. Hofmann, H. Stöcker, U. Heinz, W. Scheid and W. Greiner, Phys. Rev. Letters 36, 88 (1976).

25. W. Busza, Proc. Intern. Conf. High Energy Physics and Nuclear Structure, 1975, p. 211 (Am. Inst. Phys.) and references therein.

26. A. Mekjian, Phys. Rev. Letters 38, 640 (1977).

27. S. Garpman, J. Bond and P. J. Johansen, to be published.

28. H. J. Crawford, P. B. Price, J. Stevenson, and L. W. Wilson, Phys. Rev. Letters 34, 329 (1975).

29. H. H. Gutbrod, A. Sandoval, P. J. Johansen, A. M. Poskanzer, J. Gosset, W. G. Meyer, G. D. Westfall, and R. Stock, Phys. Rev. Letters 37, 667 (1976), and. H. H. Gutbrod, Journal de Physique Colloque C-5, 209 (1976).

30. A. M. Zebelman, A. M. Poskanzer, J. D. Bowman, R. G. Sextro, and V. E. Viola, Phys. Rev. C11, 1280 (1975).

31. A. M. Poskanzer, G. W. Butler, and E. H. Hyde, Phys. Rev. C3, 882 (1971).

32. R. H. Pehl, F. S. Goulding, D. A. Landis, and M. Lenzlinger, Nucl. Instr. Methods 59, 45 (1968).

33. G. B. Hagemann, R. Broda, B. Herskind, M. Ishihara, and S. Ogaza, Nucl. Phys. A245, 166 (1975).

34. The 800 MeV proton data is unpublished work of G. W. Butler, J. B. Natowitz, D. G. Perry, F. Plasil, A. M. Poskanzer, and L. P. Remsberg.

35. P. J. Karol, Phys. Rev. C11, 1203 (1975).

36. J. D. Bowman, W. J. Swiatecki, and C.-F. Tsang, LBL-2908 (TID-4500-R61), unpublished report (1973).

37. R. Stock, in "Heavy Ion Collisions", Vol. I, R. Bock (ed.), North Holland 1977.

38. W. J. Swiatecki, unpublished report (1976).

39. L. D. Landau and E. M. Lifshitz, Statistical Physics (Addison-Wesley, N.Y., 1969), p. 109.

40. R. Hagedorn and J. Ranft, Nuovo Cimento 6, 300 (1968).

41. S. T. Butler and C. A. Pearson, Phys. Rev. Lett. 7, 69 (1961), and Phys. Rev. 129, 836 (1963).

42. A. Schwartzschild and C. Zupančič, Phys. Rev. 129, 854 (1963).

43. A similar thermodynamic model has already been applied to the emission of light fragments in p-nucleus reactions at 600 MeV by J. P. Alard, et al., Nuovo Cimento 30A, 320 (1975).

Table 1 Systems Measured

	Bombarding Energy	Part.	Energy Range	Angles	Tag
^{20}Ne+U	2.1 GeV/nucl	He → B	low	90°	No
		H - He	high	ang dist	Yes
		Li → O	high	ang dist	Yes
	400 MeV/nucl	H - He	high	ang dist	Yes
		Li → O	high	ang dist	Yes
	250 MeV/nucl	H - He	high	ang dist	Yes
^{20}Ne+Al	2.1 GeV/nucl	H - He	high	ang dist	Yes
^{12}C+U	2.1 GeV/nucl	He → B	low	90°	No
^{4}He+U	400 MeV/nucl	H - He	high	ang dist	Yes
		Li → O	high	ang dist	Yes
Previously Measured[a]					
^{16}O+U	1.05 GeV/nucl	He	high	ang dist	No
^{16}O+Ag	1.05 GeV/nucl	He	high	ang dist	No
^{4}He+U	1.05 GeV/nucl	He	high	ang dist	No
	700 MeV/nucl	He	high	ang dist	No

(a) See Ref. 7

Table 2 Energies covered by the Si-plastic scintillator telescope for proton to ^{4}He fragments (in MeV/nucleon), and by the Si-Ge telescope for Li to N (in MeV).

Particle	E lower (MeV/nucl)	E upper (MeV/nucl)
p	30	90 (190) [a]
d	25	60
t	15	50
^{3}He	30	100 (150) [a]
^{4}He	30	110

	E lower (MeV)	E upper (MeV) 3 mm Ge	E upper (MeV) 3+8 mm Ge
Li	63	154	490
^{7}Be	86	280	730
^{9,10}Be	90	400	1060 [b]
B	118	535	1100 [b]
C	150	910	1420 [b]
N	190	1100	1860 [b]

(a) Extended energy range beyond the punch-through energy in the 10 cm plastic, without isotope separation.

(b) Range of the telescope but not observed.

Table 3 Production cross sections (mb/sr) at $\theta_{lab} = 90^{\circ}$ from a uranium target.

Projectile / Energy / Fragment	p 5 GeV	d 2.1 GeV/nucl	α 2.1 GeV/nucl	^{12}C 2.1 GeV/nucl	^{20}Ne 2.1 GeV/nucl
^{4}He	290	400	870	1620	2250
^{6}He	7.3	11	24	50	65
^{6}Li	7.1	9	23	56	85
^{7}Li	13	20	52	104	153
^{8}Li	3.7	4.5	17	30	49
^{7}Be	1.1	1.6	5	15	19
^{9}Be	3.7	4.8	12	22	36
^{10}Be	3.7	5.9	16	26	39

Table 4 Cross sections (barns) for the different fragments integrated over the energy ranges covered in this experiment.

Reaction (MeV/nucl) \ Fragment (MeV/nucl)		p (25-190)	d (25-60)	t (15-50)	^{3}He (30-150)	^{4}He (30-110)
^{20}Ne + U	2100	-	-	8.2	3.3	2.6
	400	48	10.4	5.5	2.3	1.8
	250	39	7.1	4.0	2.2	1.8
^{4}He + U	400	12	1.7	.53	.18	.07
^{20}Ne + Al	2100	-	-	.28	.13	.05

Table 5 Cross sections (barns) for the different fragments integrated over the velocity window from 30 to 50 MeV/nucleon.

Reaction (MeV/nucl) \ Fragment	p	d	t	^{3}He	^{4}He
^{20}Ne + U 2100	10.3	-	4.3	1.6	1.3
400	9.5	5.0	2.4	0.97	1.1
250	10.6	4.5	2.4	0.94	1.1
^{4}He + U 400	3.1	0.97	0.18	0.098	0.06
^{20}Ne + Al 2100	-	-	0.18	0.08	0.03

Table 6 Mean multiplicities <M> of charged particles in the interval from 15° to 60°, asscciated with various fragments identified in the single particle telescope at 90°, for the different reactions studied. Lower energy cutoffs in <M> are about 50 MeV/nucleon for protons and clusters, and 20 MeV for pions.

Reaction (MeV/nucl) / Fragment	^{20}Ne + U 2100	^{20}Ne + Al 2100	^{20}Ne + U 400	^{20}Ne + U 250	^{4}He + U 400
p	25.6	10.1	8.0	5.5	1.6
d	26.9	10.6	8.9	5.9	1.6
t	26.5	10.6	9.2	6.3	1.9
^{3}He	29.4	11.7	9.2	6.1	1.8
^{4}He	29.4	11.5	9.5	6.3	1.9
Li	25.4		7.8		1.4
^{7}Be	26.5		8.5		1.4
^{9,10}Be	26.0		8.7		1.4
B	27.0		8.9		1.2
C	27.3		8.8		
N	27.5		8.4		

Table 7 Calculated properties of the fireball at the impact parameter with the maximum weight (b_{mw}) on a uranium target. The temperature calculated relativistically and nonrelativistically are τ_r and τ_{nr}

Projectile		β_{inc}	b_{mw}	N	ε	τ_r	τ_{nr}	β
(MeV/nucleon)			(fm)		(MeV/nucleon)	(MeV)	(MeV)	
^{20}Ne	250	0.61	4.8	64	44	28	29	0.22
^{20}Ne	400	0.71	4.8	64	74	47	49	0.27
^{4}He	400	0.71	4.7	25	51	33	34	0.17
^{20}Ne	2100	0.95	4.8	64	363	92[a]	-	0.56

[a] The temperature was calculated taking into account both relativistic effects and the excitation of baryon resonances.

Table 8 Radius p_o (MeV/c) of the momentum sphere for coalescence

Reaction (MeV/nucl)	Fragment	d	t	^{3}He	^{4}He
^{20}Ne + U	250	126	140	135	147
^{20}Ne + U	400	129	129	129	142
^{20}Ne + U	2100	106	116	106	118
^{4}He + U	400	126	127	127	132

FIGURE CAPTIONS

Fig. 1 The experimental setup consisting of a particle telescope mounted on a movable arm and a monitor telescope fixed at 90° inside a scattering chamber fitted with a 3/8" thick aluminum dome. Fifteen plastic scintillators were arranged azimuthally around the beam axis outside the chamber.

Fig. 2 Particle identifier spectra from a) the Si-plastic scintillator telescope; and b) from the Si-Ge telescope.

Fig. 3 Si-Ge telescope consisting of an array of twelve Si detectors, two thin Ge and two thick Ge detectors enclosed in a cryostat. The boron nitride had the shape of a window frame. The telescope had an active area of 20 cm^2.

Fig. 4 Simplified electronic diagram representing the fast and slow logic used with both the Si-plastic and Si-Ge telescopes. An "alive" signal was used to gate the linear signals as described in the text.

Fig. 5 The 90° energy spectra of low energy fragments from U irradiated with 2.1 GeV/nucleon ^{20}Ne ions.

Fig. 6 a) Energy spectra at 90° of ^{4}He fragments from U bombarded with different projectiles. b) Comparison of the shape of the 90° ^{4}He and ^{7}Li energy spectra, normalized at the peak cross section, for different projectiles incident on U.

Fig. 7 Double differential cross sections for the light fragments emitted from the irradiation of uranium with ^{20}Ne ions at 2.1 GeV/nucleon.

Fig. 8 Light fragment double differential cross sections from ^{20}Ne on U at 400 MeV/nucleon.

Fig. 9 Light fragment double differential cross sections from ^{20}Ne on U at 250 MeV/nucleon.

Fig. 10 Double differential cross sections for light fragments produced from the irradiation of uranium with 400 MeV/nucleon ^{4}He ions.

Fig. 11 Triton, ^{3}He, and ^{4}He double differential cross sections from the irradiation of aluminum with 2.1 GeV/nucleon ^{20}Ne ions.

Fig. 12 Comparison of the 30° and 90° ^{3}He energy spectra from the irradiation of uranium with ^{20}Ne ions at three different bombarding energies.

Fig. 13 Angular distributions for the light fragments produced in the interaction of ^{20}Ne with U at 400 MeV/nucleon, integrated over the velocity window from 30 to 50 MeV/nucleon.

Fig. 14 Cross comparison of angular distributions of ^{3}He fragments integrated for two velocity windows at different incident energies and for different projectiles and targets.

a,b,c: Ne on U at 2.1, 0.4 and 0.25 GeV/nucleon, respectively;

d: Ne on Al at 2.1 GeV/nucleon (raised by a factor of 10);

e: ^{4}He on U at 0.4 GeV/nucleon (raised by a factor of 10).

Fig. 15 Energy spectra in MeV of the high energy heavy fragments from Li to O where the lines are drawn to guide the eye. Each successive spectrum was displaced by a factor of 10.

Fig. 16 Double differential cross sections for the heavy fragments produced in the irradiation of uranium with 2.1 GeV/nucleon ^{20}Ne.

Fig. 17 Double differential cross sections of the heavy fragments from 400 MeV/nucleon ^{20}Ne on U.

Fig. 18 Some double differential cross sections for Li to B from the irradiation of U with 400 MeV/nucleon ^{4}He ions.

Fig. 19 Comparison of the energy spectra at 90° in the laboratory of proton through nitrogen fragments produced by the irradiation of uranium with ^{20}Ne ions at 400 MeV/nucleon.

Fig. 20 Comparison of the m-fold charged particle coincidence distributions associated with fragments detected in the telescope at 90°. The comparisons are shown to the left for different bombarding energies, in the center for different projectiles, and to the right for different targets.

Fig. 21 Angular distribution of the ratio of events with high associated multiplicity to the events with low associated multiplicity for Ne + U.

Fig. 22 Comparison of the m-fold coincidence cross sections associated with three different fragments: p, He and ^{7}Be for two different ^{20}Ne bombarding energies on U. The areas of these curves are the values of $d\sigma/d\Omega$ for the telescope at 90°.

Fig. 23 In the fireball model the target and projectile are assumed to make clean cylindrical cuts through each other leaving a target spectator residue, and if the impact parameter is large enough also a projectile spectator. The fireball is made up from the participant nucleons which are mutually swept out in the primary interaction.

Fig. 24 Calculated geometrical quantities as a function of impact parameter b. N_p/N_t is the ratio of projectile to target participant nucleons, N_{proton} is the number of participant protons, and $2\pi bN_{proton}$ is the weight given to each impact parameter. The solid lines represent the case of Ne on U and the dashed line an equal mass projectile-target combination. The arrow on the abscissa indicates the radius of uranium and the arrow labeled b_{mw} indicates the impact parameter with the maximum weight.

Fig. 25 Kinematical quantities as a function of impact parameter calculated in the fireball model. The velocity of the fireball in the lab is β and ε is the available kinetic energy per nucleon in the fireball

Fig. 25 (cont.) center of mass. The solid lines refer to the case of Ne on U and the dashed lines refer to any equal mass projectile target case. The incident energy in both instances is 400 MeV/nucleon.

Fig. 26 Measured proton inclusive spectra from a uranium target at 30°, 60°, 90°, 120°, and 150° in the laboratory. For ^{20}Ne at 250 MeV/nucleon 150° data were not taken. The solid lines are calculated with the fireball model.

Fig. 27 Calculated proton multiplicity distribution from the fireball model for Ne on U and Ne on Al. The maximum proton multiplicity for Ne on U and Ne on Al are 35 and 21 respectively.

Fig. 28 The upper half of the figure shows the associated multiplicity distribution for Ne on U calculated according to eq. 16. This calculation is then compared to measured distributions in the lower part. Data are associated with protons detected in the telescope at 90°. The efficiency Ω of each tag counter was adjusted to reproduce the shape of the data.

Fig. 29 Double differential cross sections for hydrogen and helium isotopes from ^{20}Ne on U compared with calculations (lines) using the coalescence formalism.

Fig. 30 Coalescence calculations (lines) compared with Li and ^{7}Be double differential cross sections. For Li a mass of 6 was used in the calculations.

Fig. 31 Comparison of boron spectra with a calculation assuming emission from an equilibrated system with temperature τ and velocity β.

Fig. 32 Invariant cross section $\frac{1}{p}\frac{d^2\sigma}{dEd\Omega}$ versus momentum p for all fragments measured at 90° from 400 MeV/nucleon ^{20}Ne on U.

Fig. 33 Contours of constant invariant cross sections in the $(y,p_\perp)$ plane for different fragments from ^{20}Ne on U at 400 MeV/nucl.; $p_\perp$ is the transverse momentum per nucleon of a fragment and y is the rapidity defined as:
$y = \frac{1}{2} \ln \left[(E + p_\parallel)/(E - p_\parallel) \right]$. The spacing between the lines corresponds to a constant factor in cross section. The thick lines are labelled by the common logarithm of the invariant cross section. Target and projectile rapidity are indicated by arrows. The rapidity of the fireball with the maximum weight is 0.28.

Fig. 34 Contours of constant invariant cross sections in the $(y,p_\perp)$ plane for ^3He fragments from ^{20}Ne on U at different bombarding energies.

Fig. 35 Definition of the sectors where the various F functions apply in β,ν space.

Fig. 36 Behavior of the F functions versus β for various values of ν.

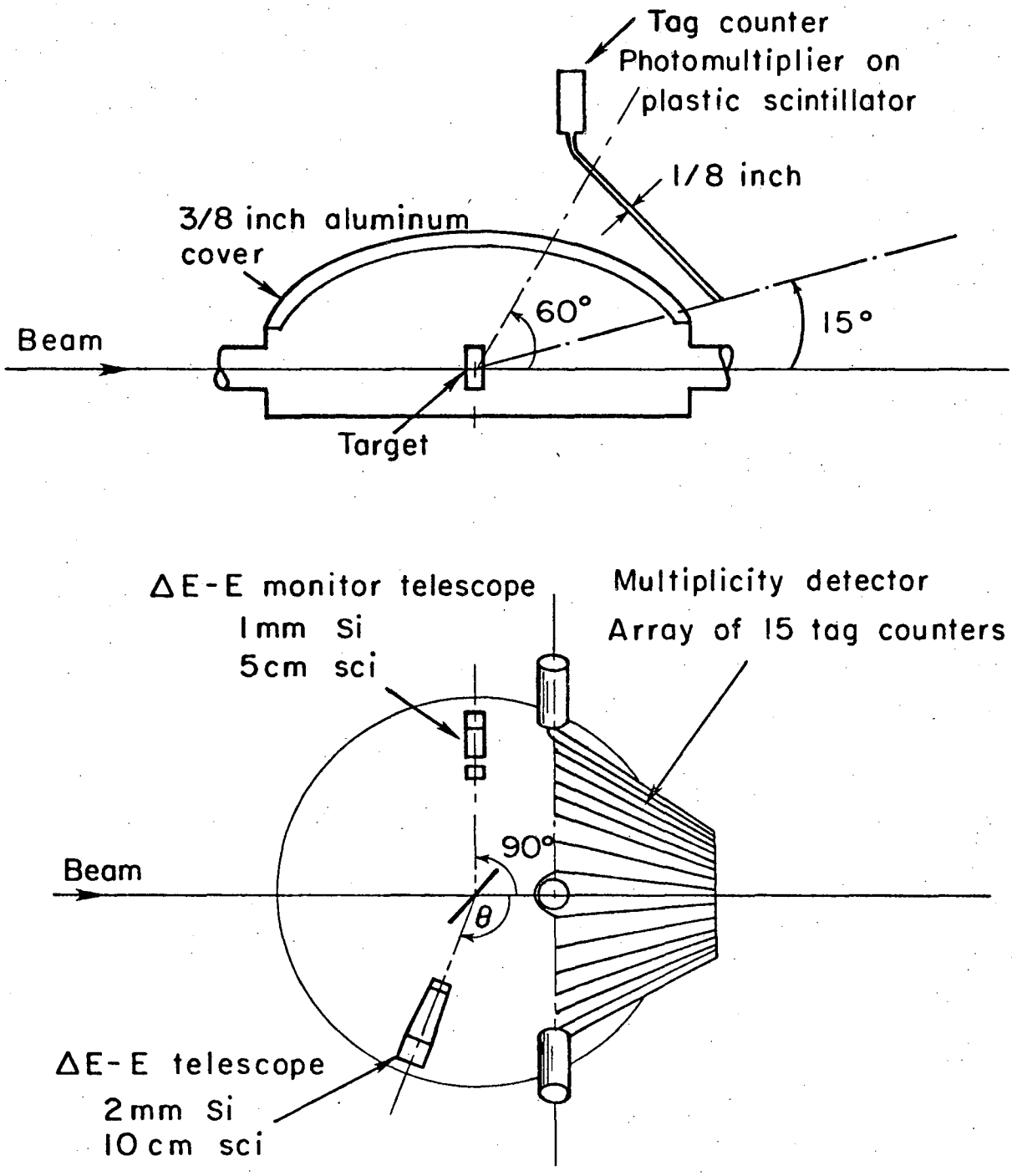
Tag counter
Photomultiplier on
plastic scintillator
1/8 inch
3/8 inch aluminum
cover
60°
15°
Beam
Target
ΔE-E monitor telescope
1mm Si
5cm sci
Multiplicity detector
Array of 15 tag counters
90°
Beam
θ
ΔE-E telescope
2mm Si
10cm sci
XBL7512-9933

Fig. 1

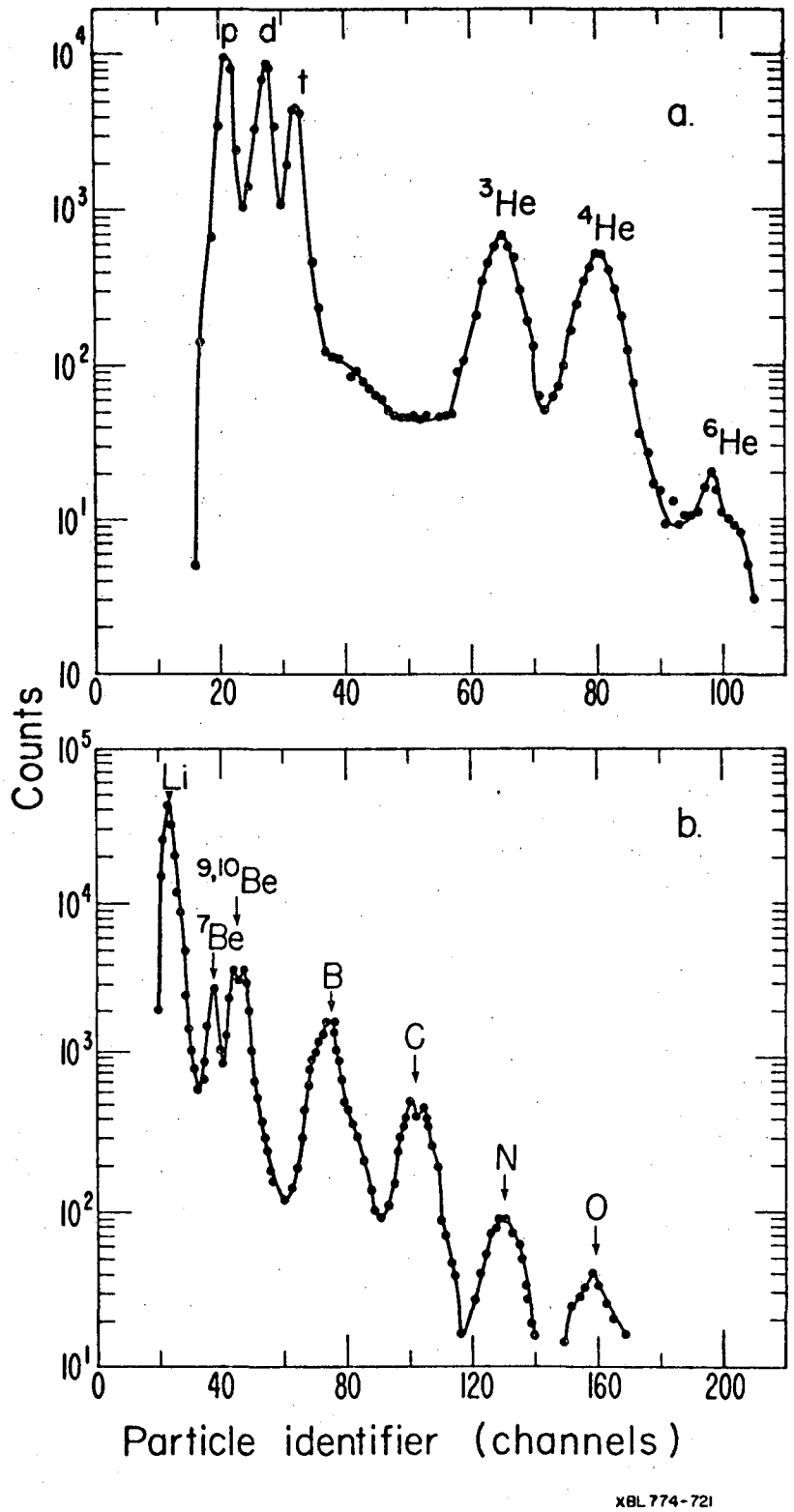

XBL774-721

Fig. 2

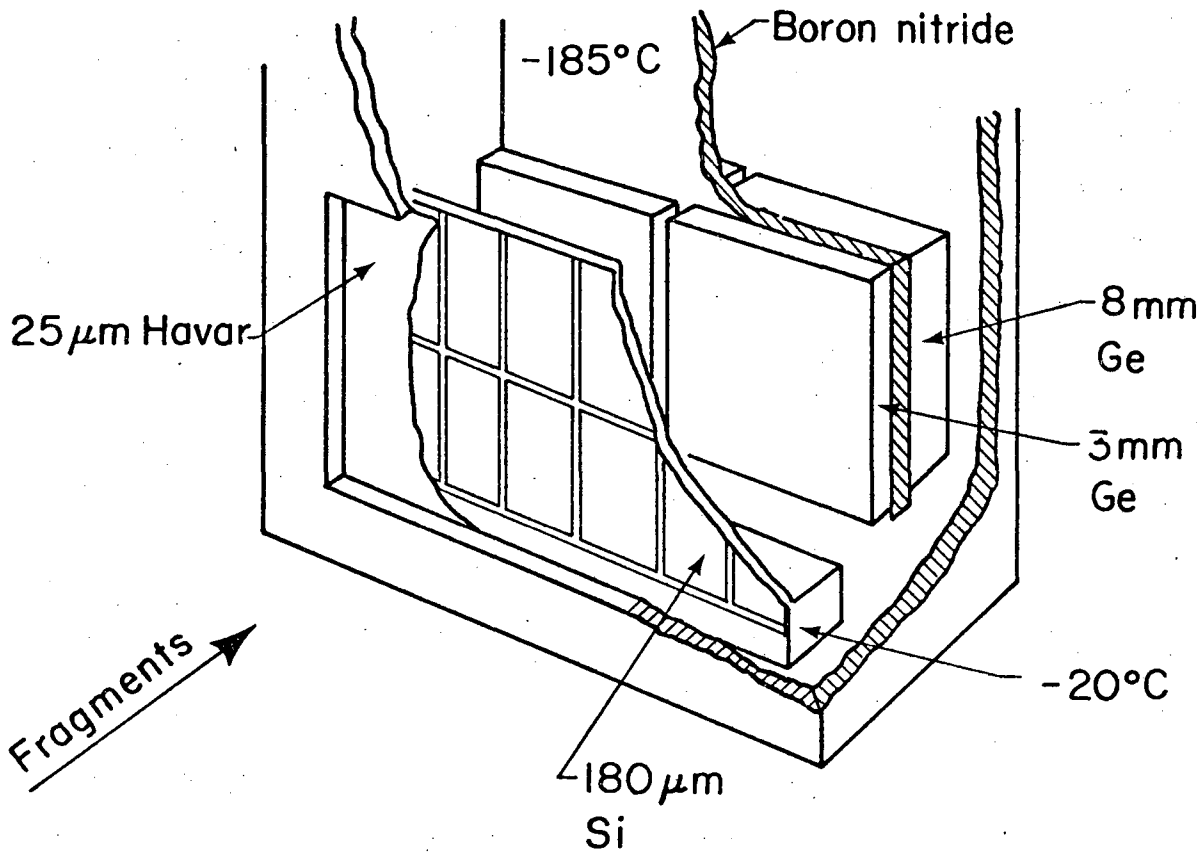

XBL 773-545

Fig. 3

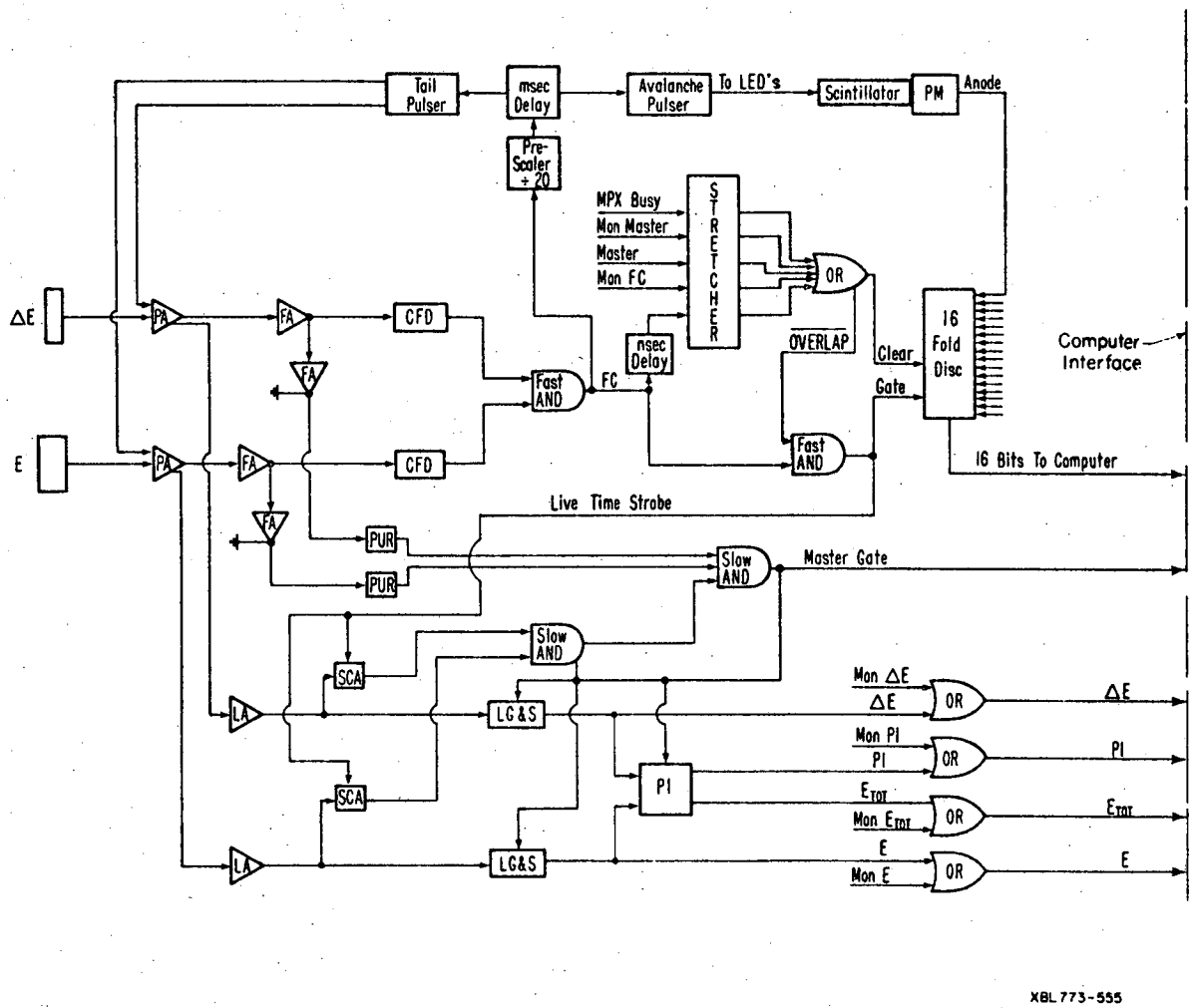

XBL 773-555

Fig. 4

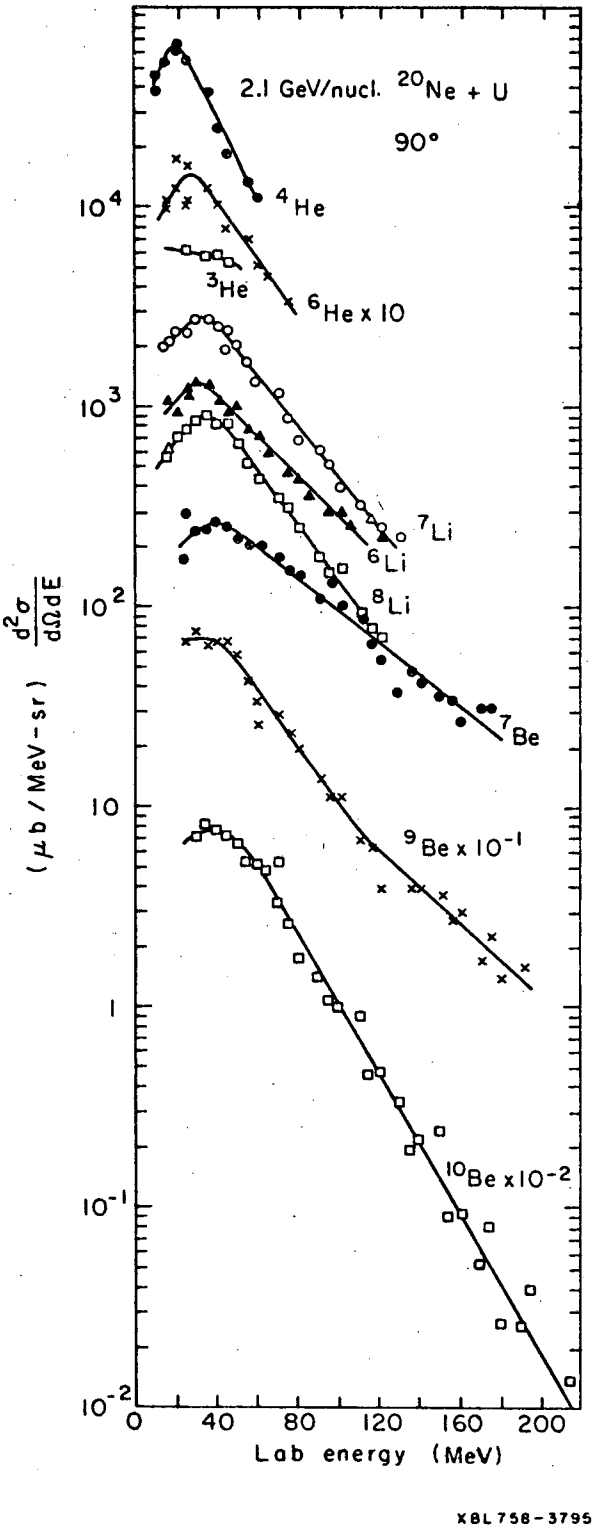
2.1 GeV/nucl. ^{20}Ne + U
90°
^{4}He
^{3}He
^{6}He x 10
^{7}Li
^{6}Li
^{8}Li
^{7}Be
^{9}Be x 10^{-1}
^{10}Be x 10^{-2}
$\frac{d^2\sigma}{d\Omega dE}$ (μb / MeV - sr)
10^{4}
10^{3}
10^{2}
10
1
10^{-1}
10^{-2}
0
40
80
120
160
200
Lab energy (MeV)
X8L758-3795

Fig. 5

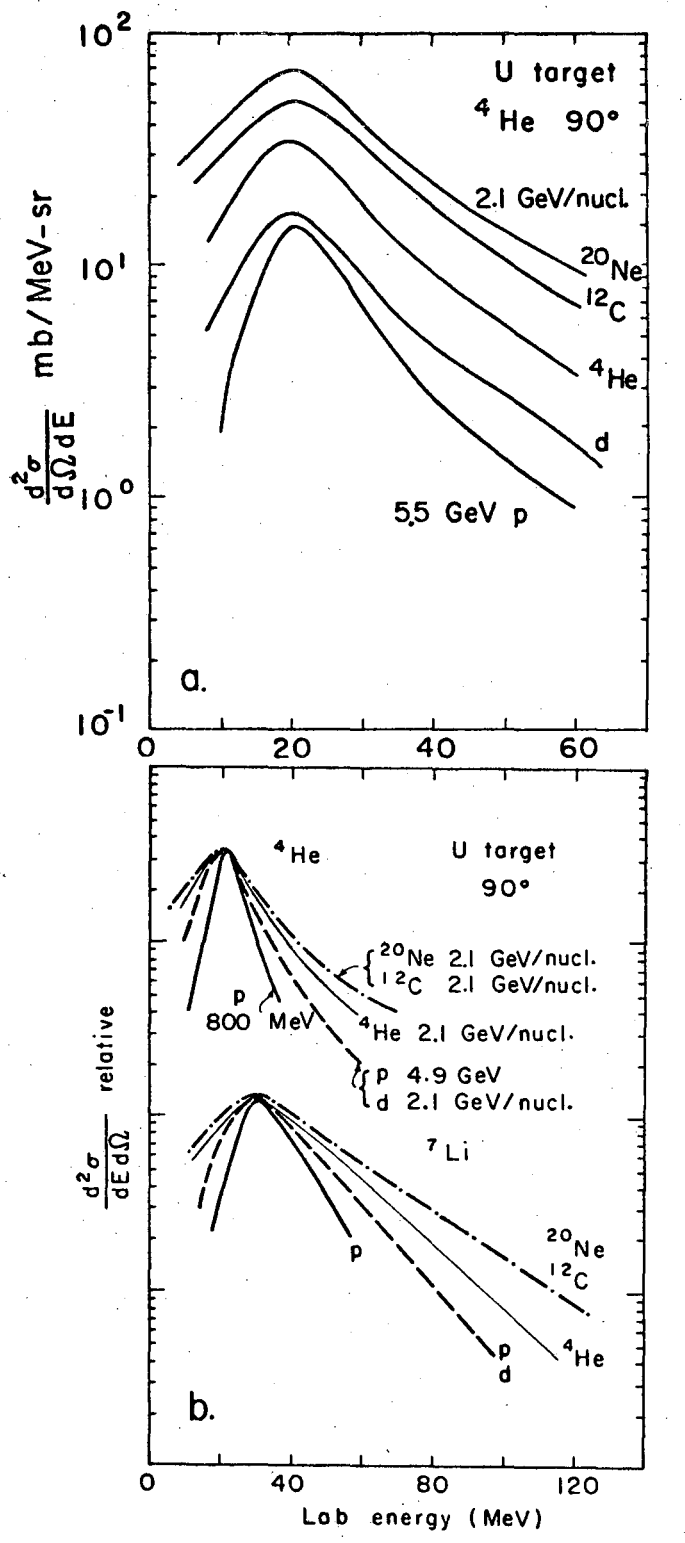

Fig.6

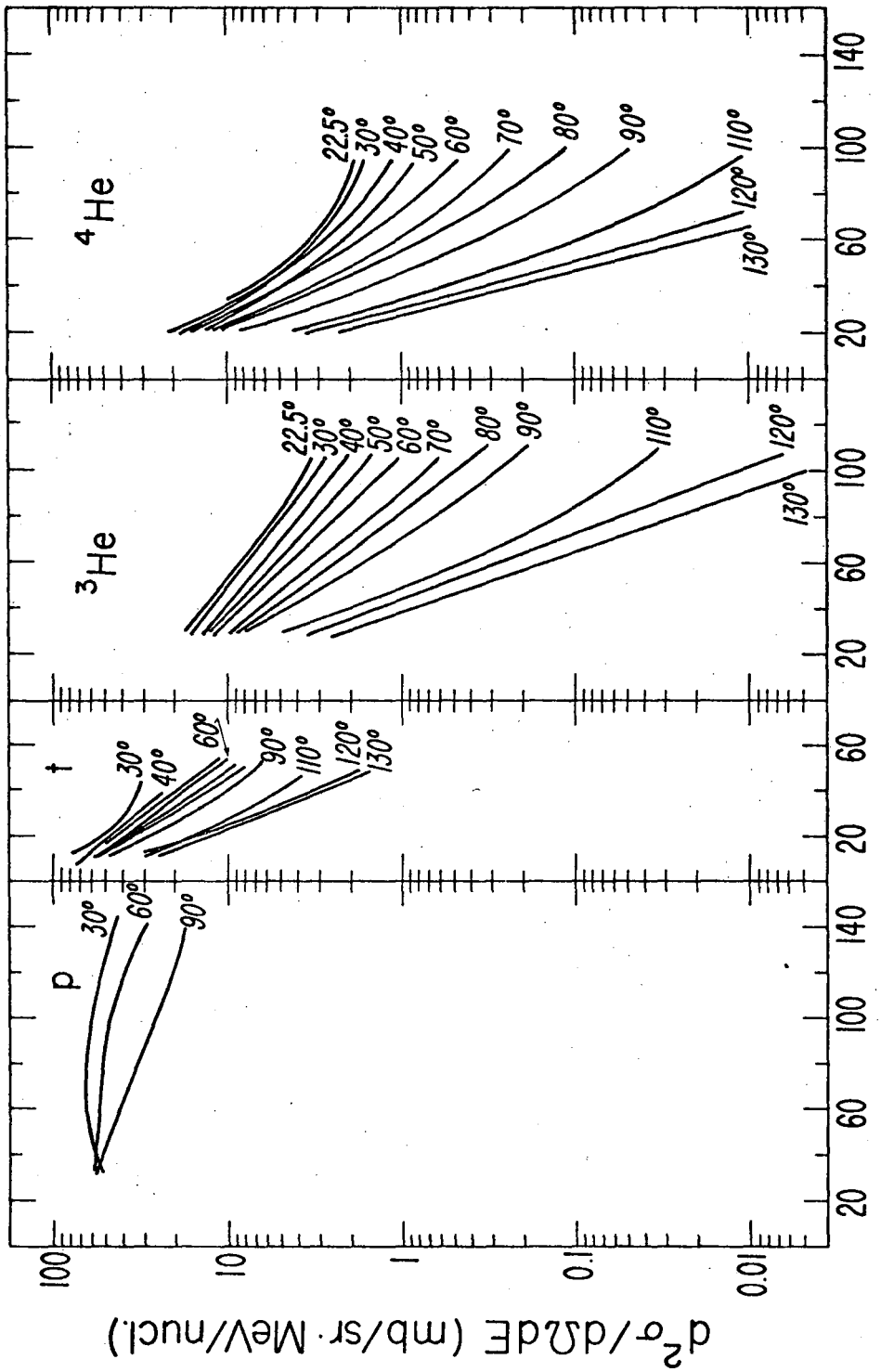

XBL 771-70

Fig. 7

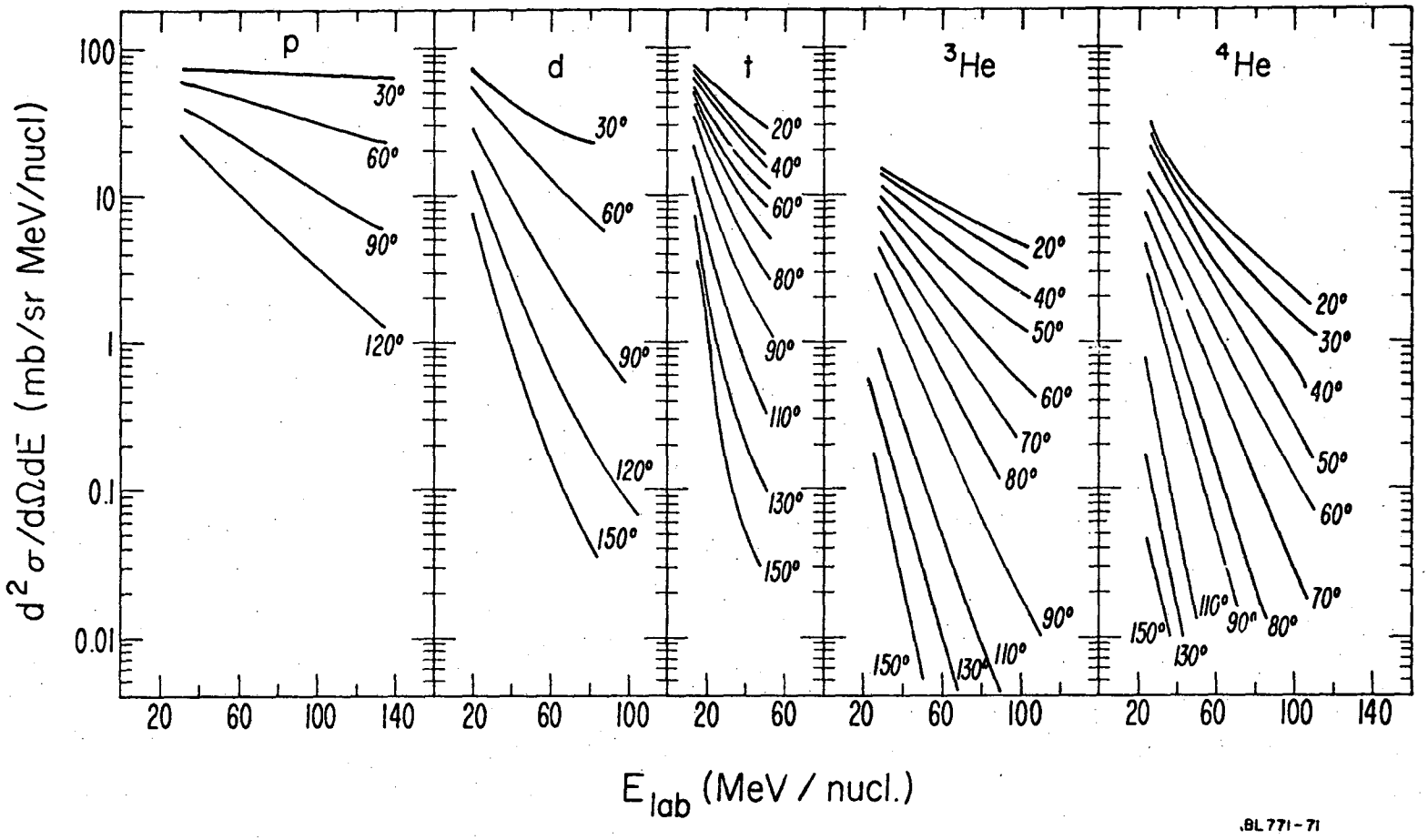

Fig. 8

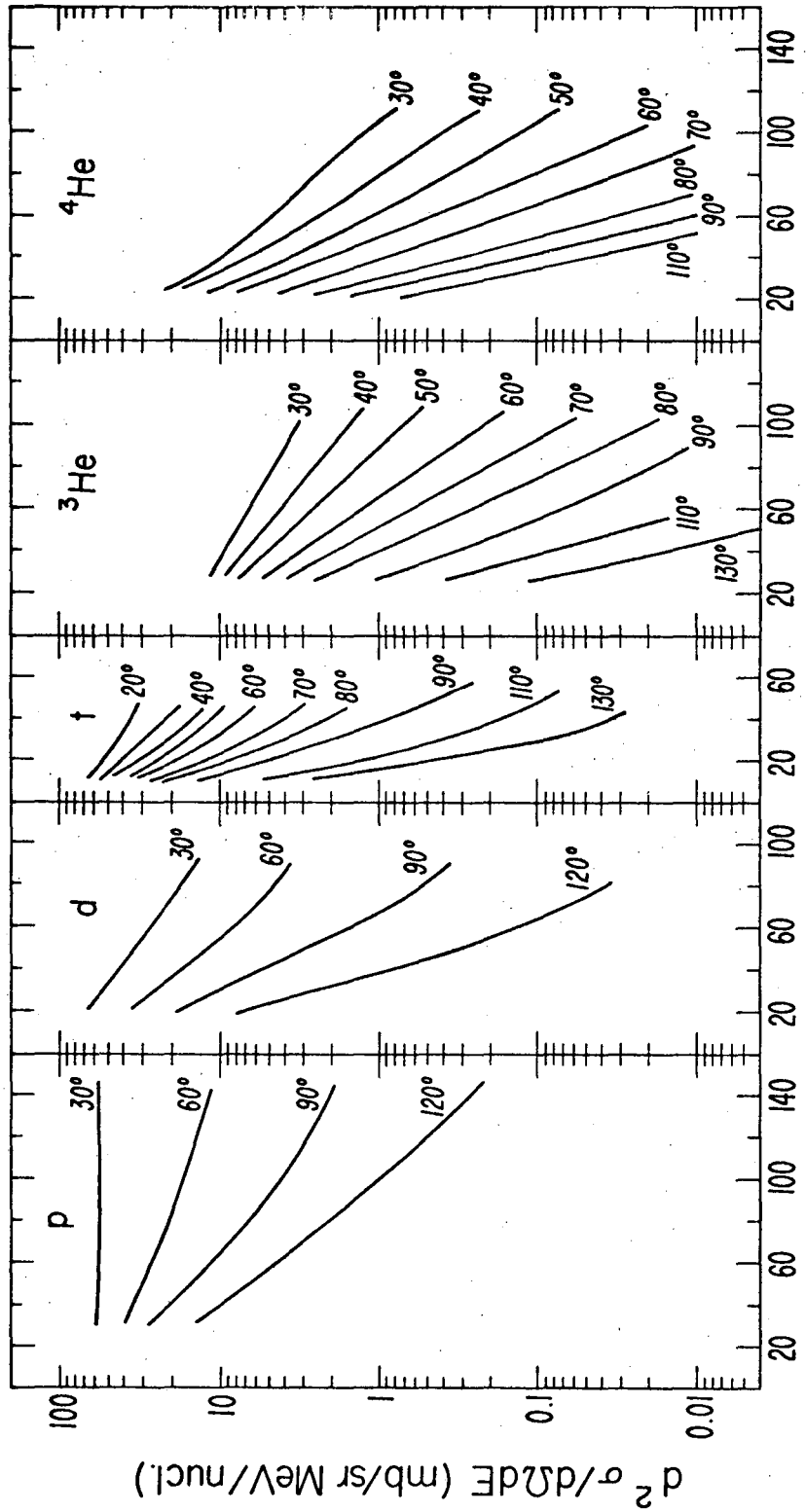
d²σ/dΩdE (mb/sr MeV/nucl.)
E_lab (MeV/nucl.)
p
d
t
³He
⁴He
30°
40°
50°
60°
70°
80°
90°
110°
120°
130°
XBL 771-69

Fig. 9

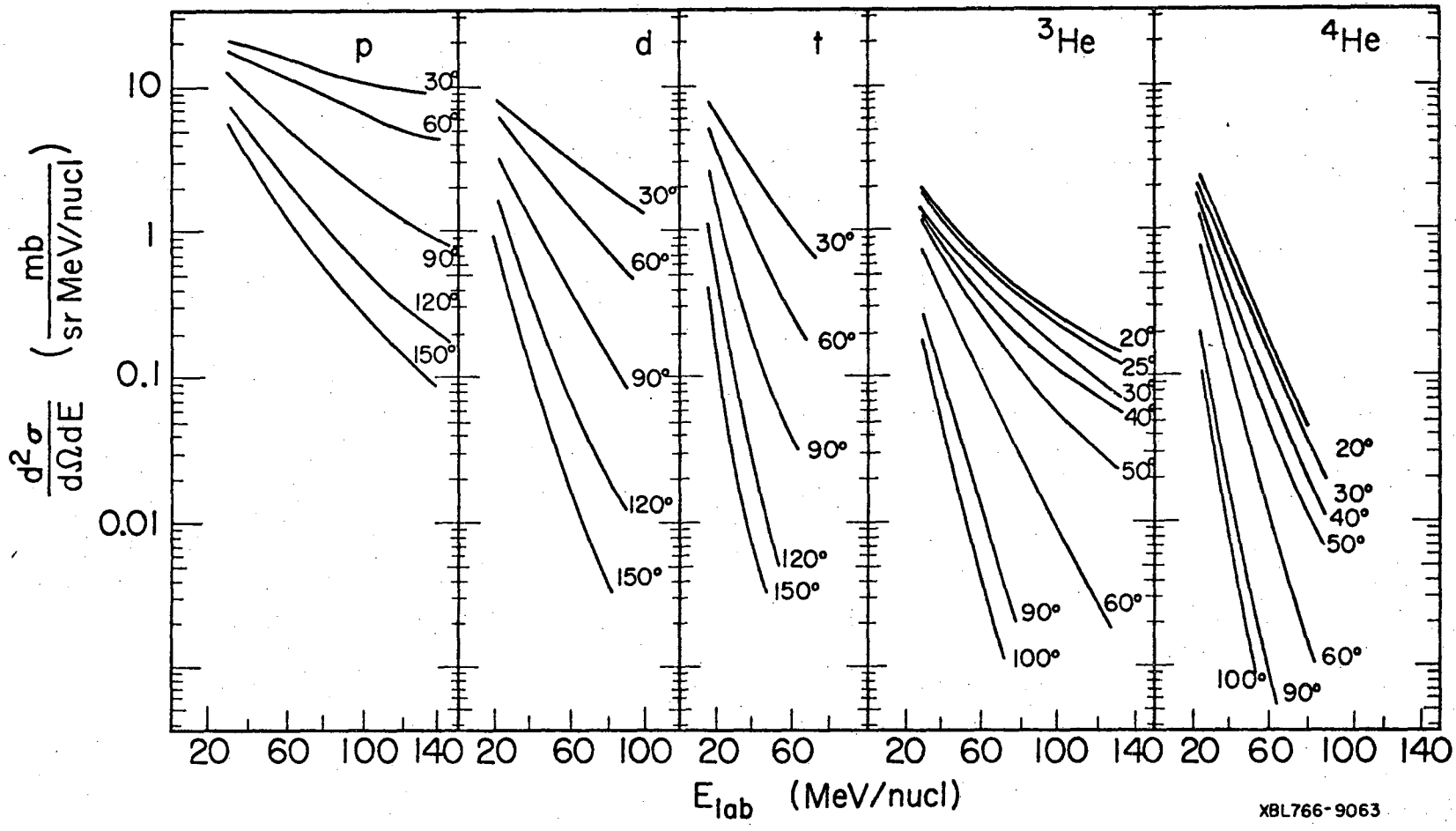

Fig. 10

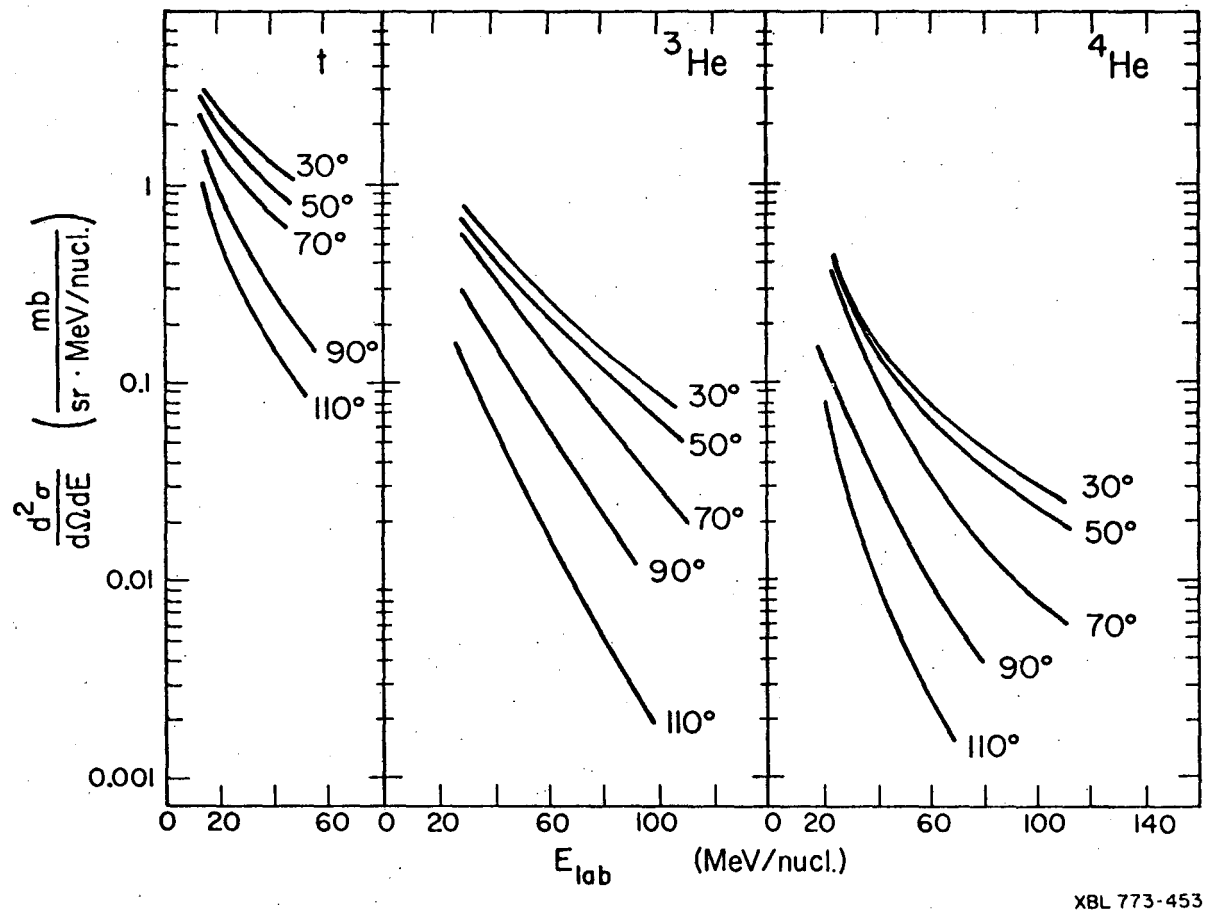
t
3He
4He
30°
50°
70°
90°
110°
1
0.1
0.01
0.001
0 20 60
0 20 60 100
0 20 60 100 140
E lab (MeV/nucl.)
d²σ/dΩdE (mb/sr · MeV/nucl.)
XBL 773-453

Fig. 11

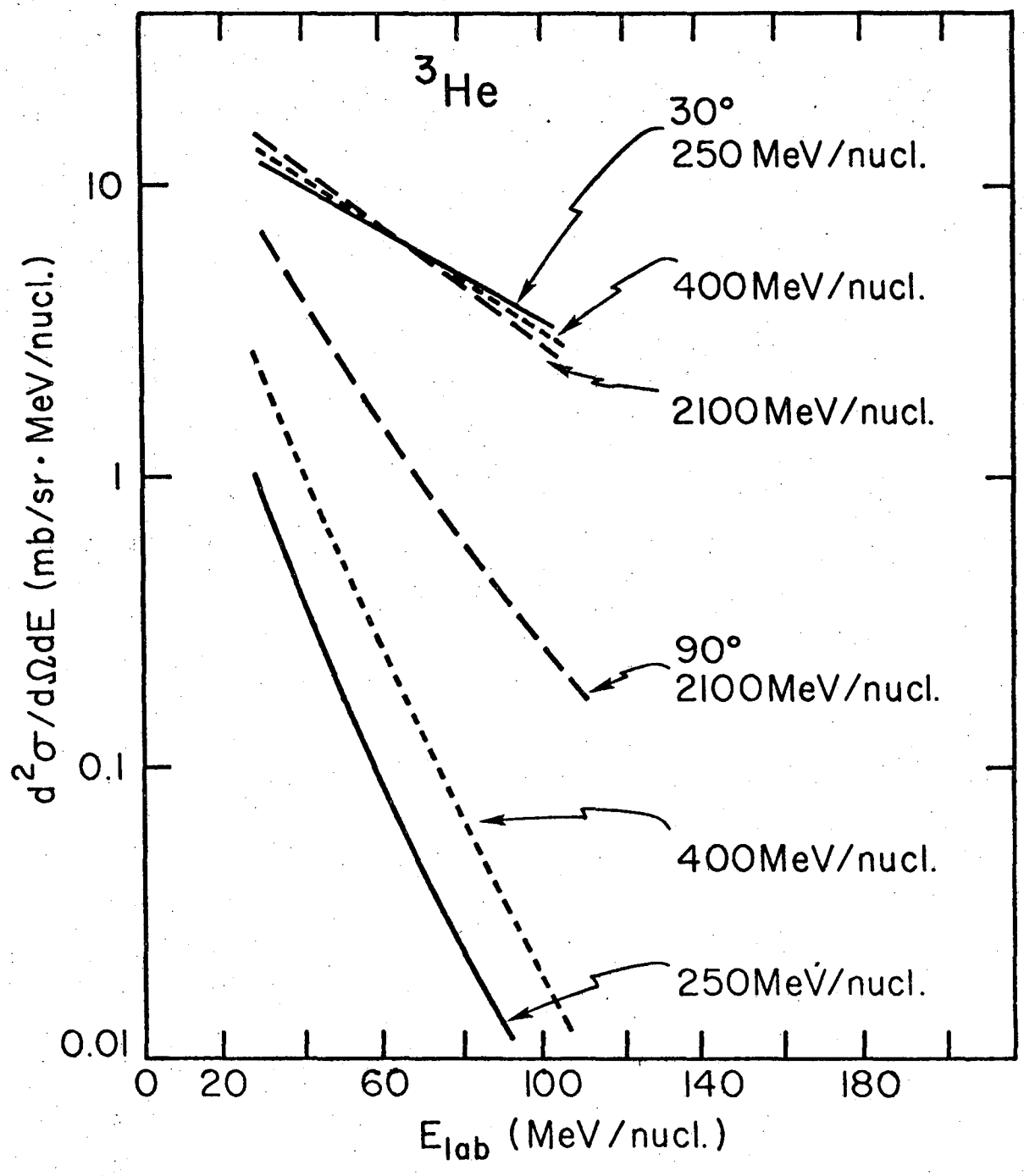

XBL 771-217

Fig. 12

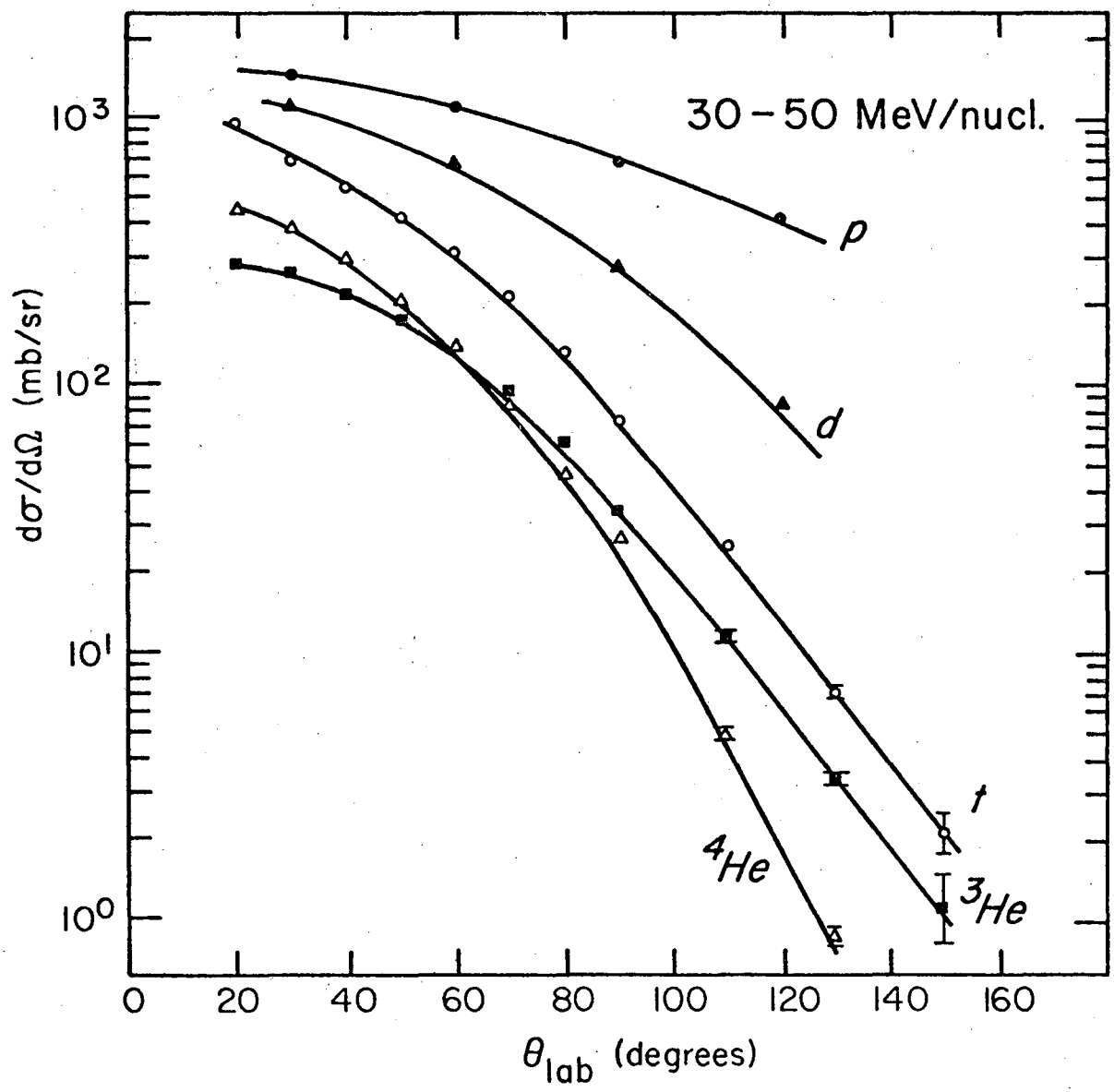
30 – 50 MeV/nucl.
p
d
t
3He
4He
10^3
10^2
10^1
10^0
dσ/dΩ (mb/sr)
0
20
40
60
80
100
120
140
160
θlab (degrees)
XBL 771-216A

Fig. 13

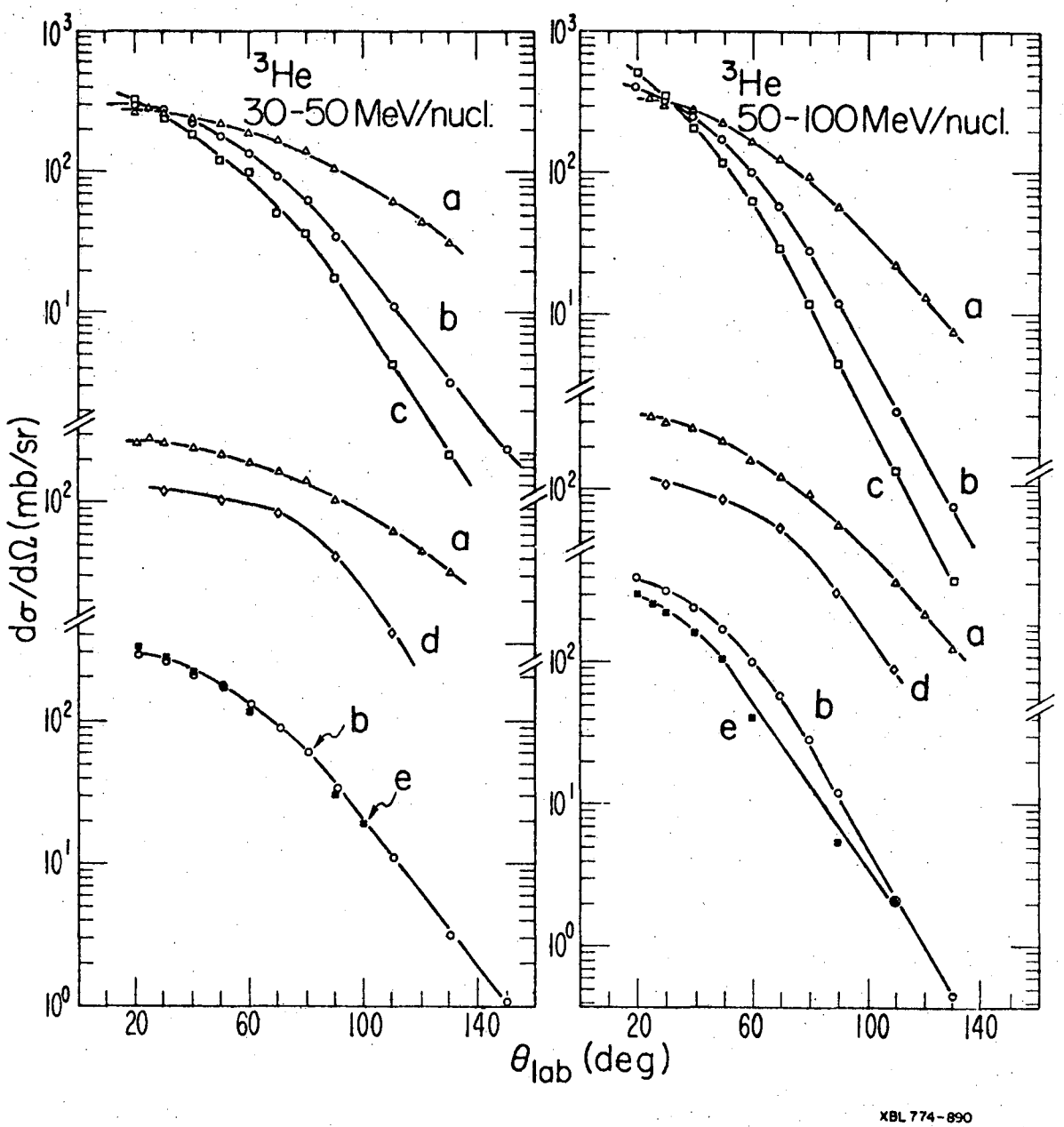

Fig. 14

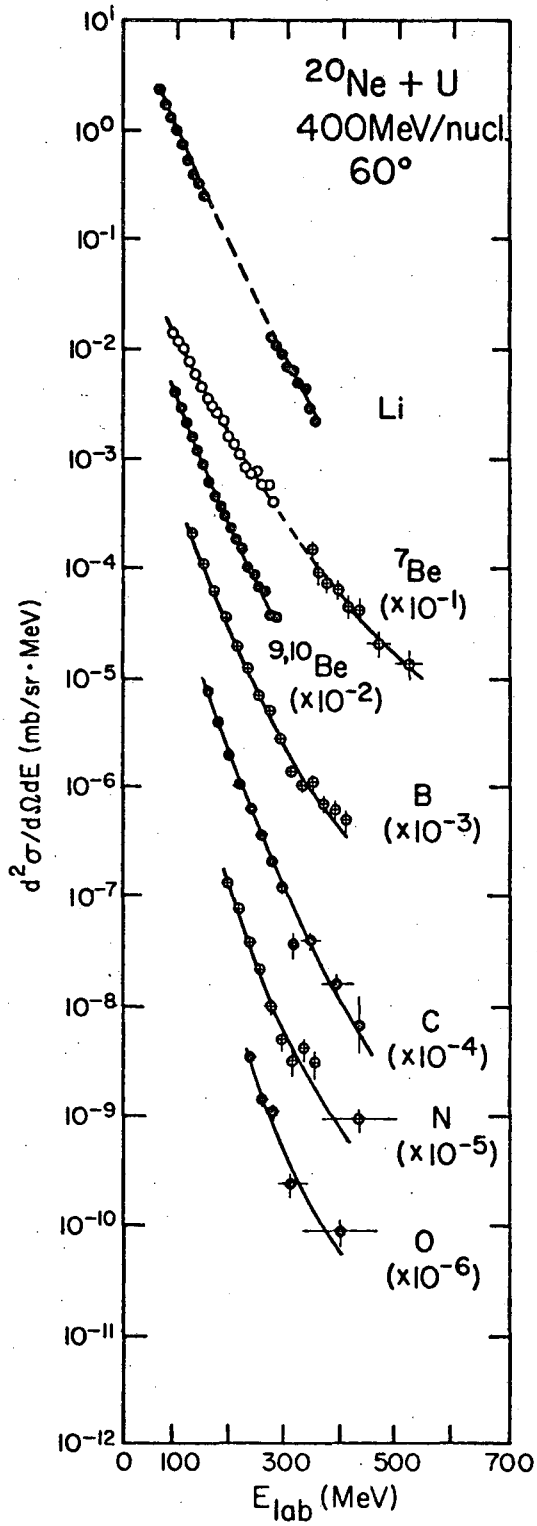

XBL 771-219

Fig. 15

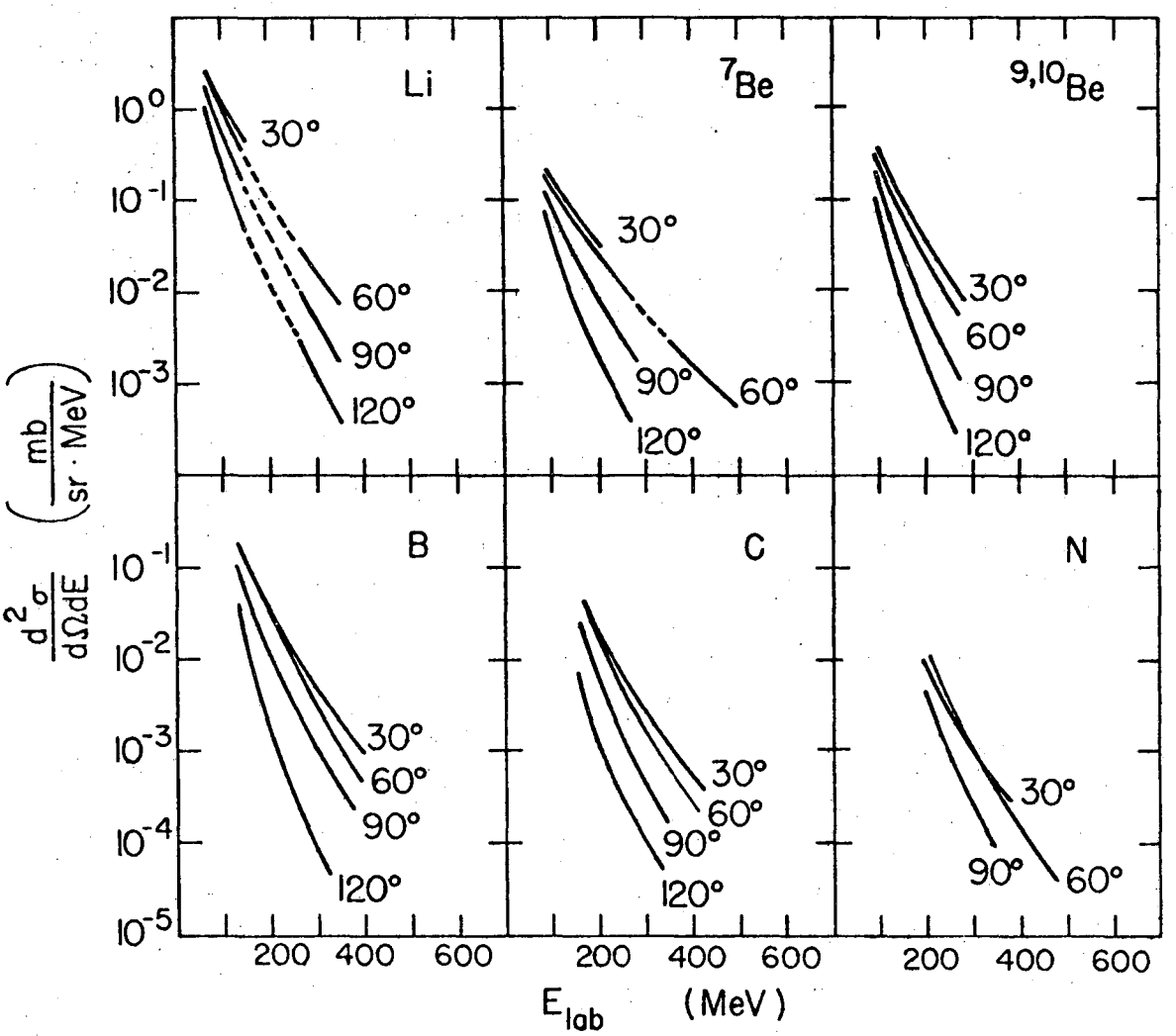

XBL 773-454

Fig. 16

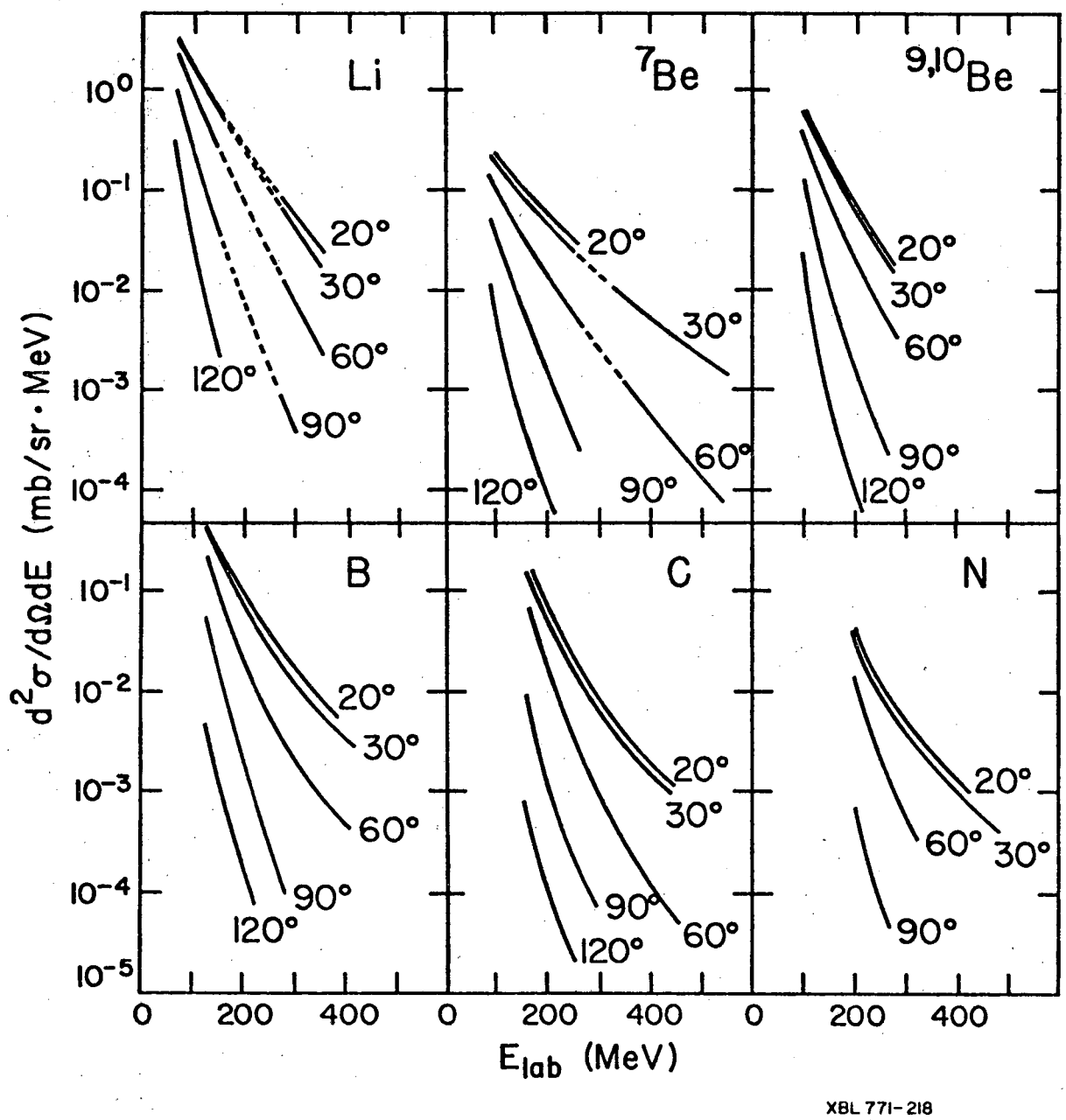
Li
7Be
9,10Be
B
C
N
20°
30°
60°
90°
120°
d²σ/dΩdE (mb/sr • MeV)
Elab (MeV)
XBL 771-218

Fig. 17

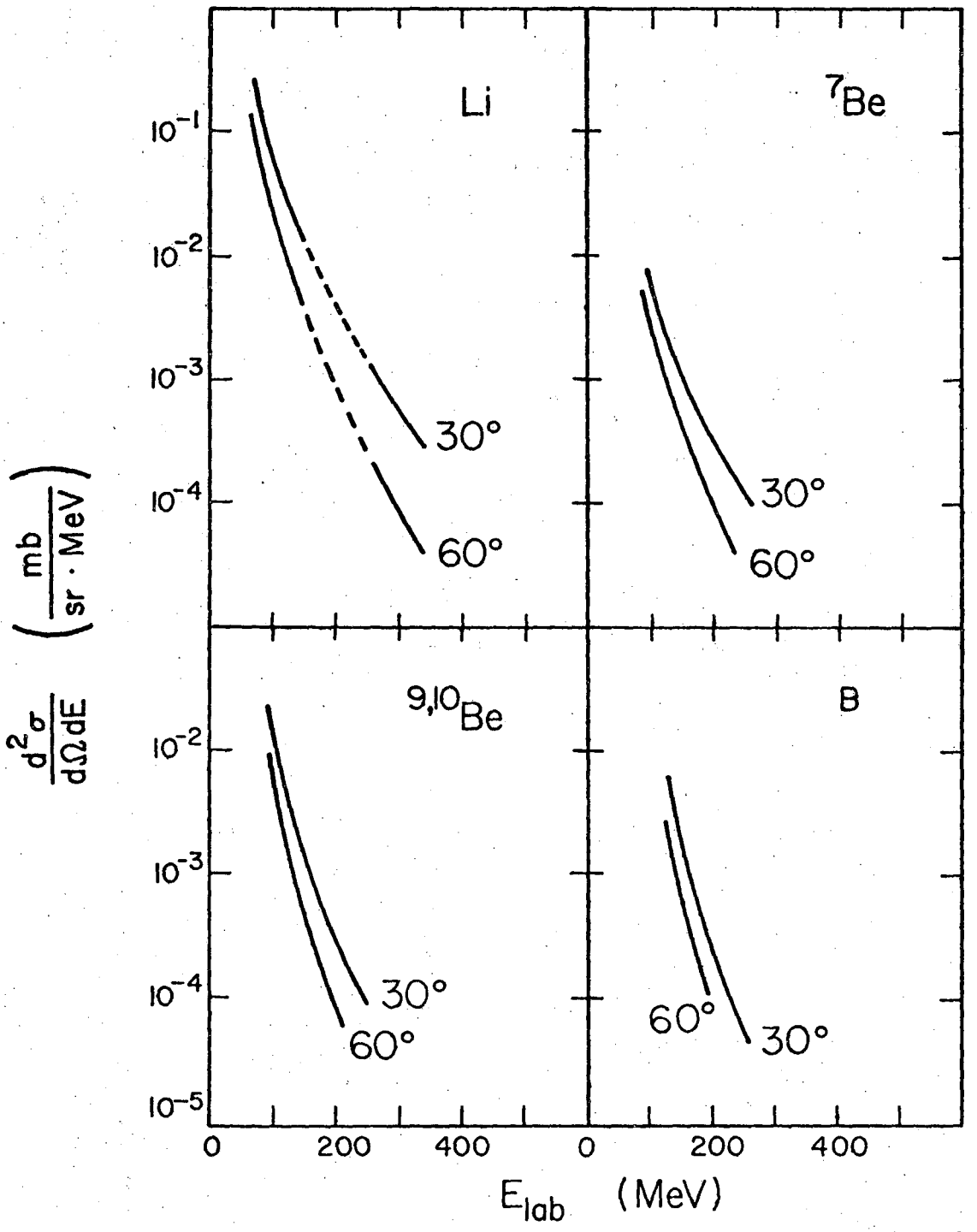

XBL 773-452

Fig. 18

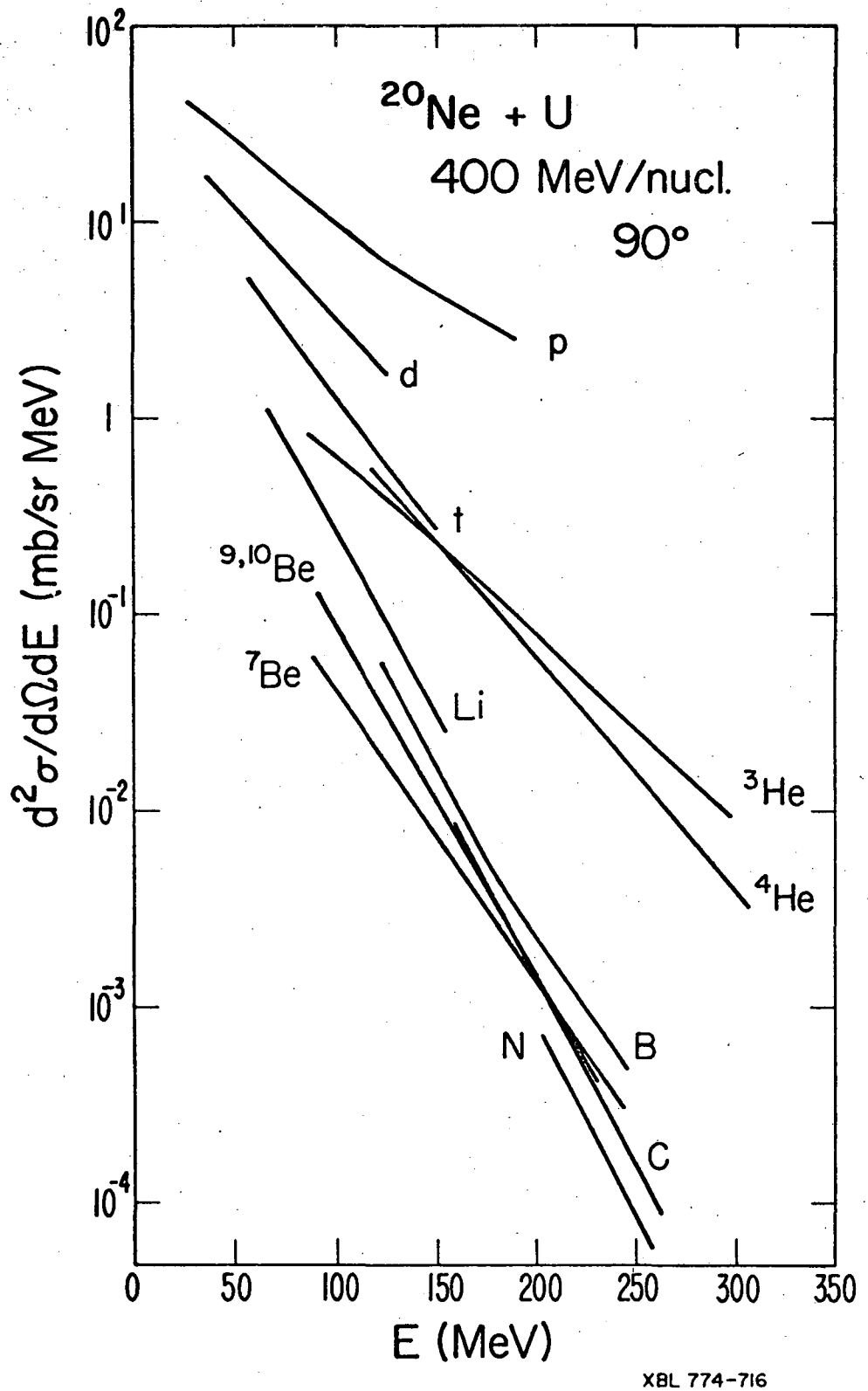
^{20}Ne + U
400 MeV/nucl.
90°
p
d
t
^{9,10}Be
^{7}Be
Li
^{3}He
^{4}He
B
N
C
$d^2\sigma/d\Omega dE$ (mb/sr MeV)
E (MeV)
10^2
10^1
1
10^{-1}
10^{-2}
10^{-3}
10^{-4}
0
50
100
150
200
250
300
350
XBL 774-716

Fig. 19

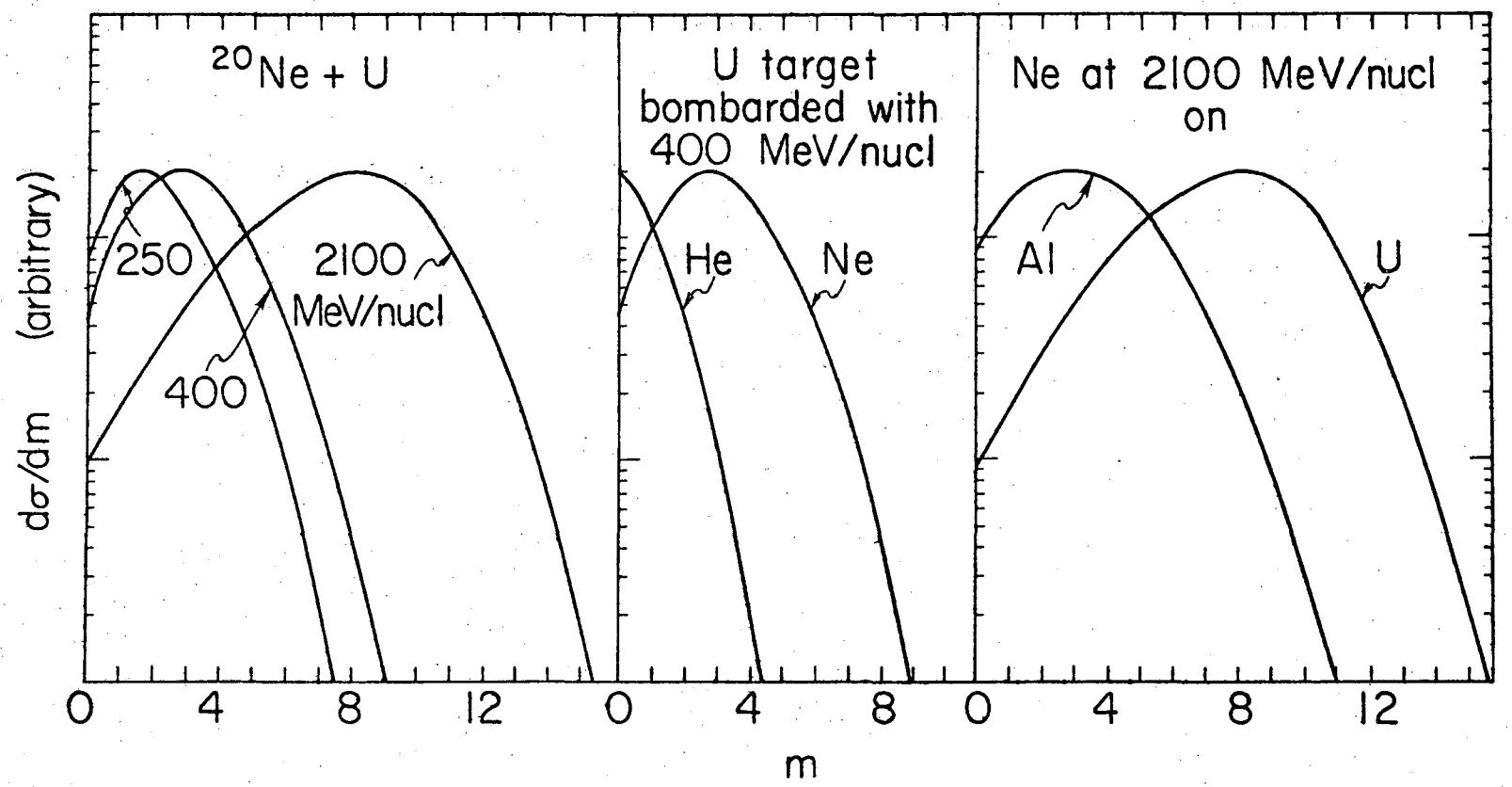

XBL 766-2956

Fig. 20

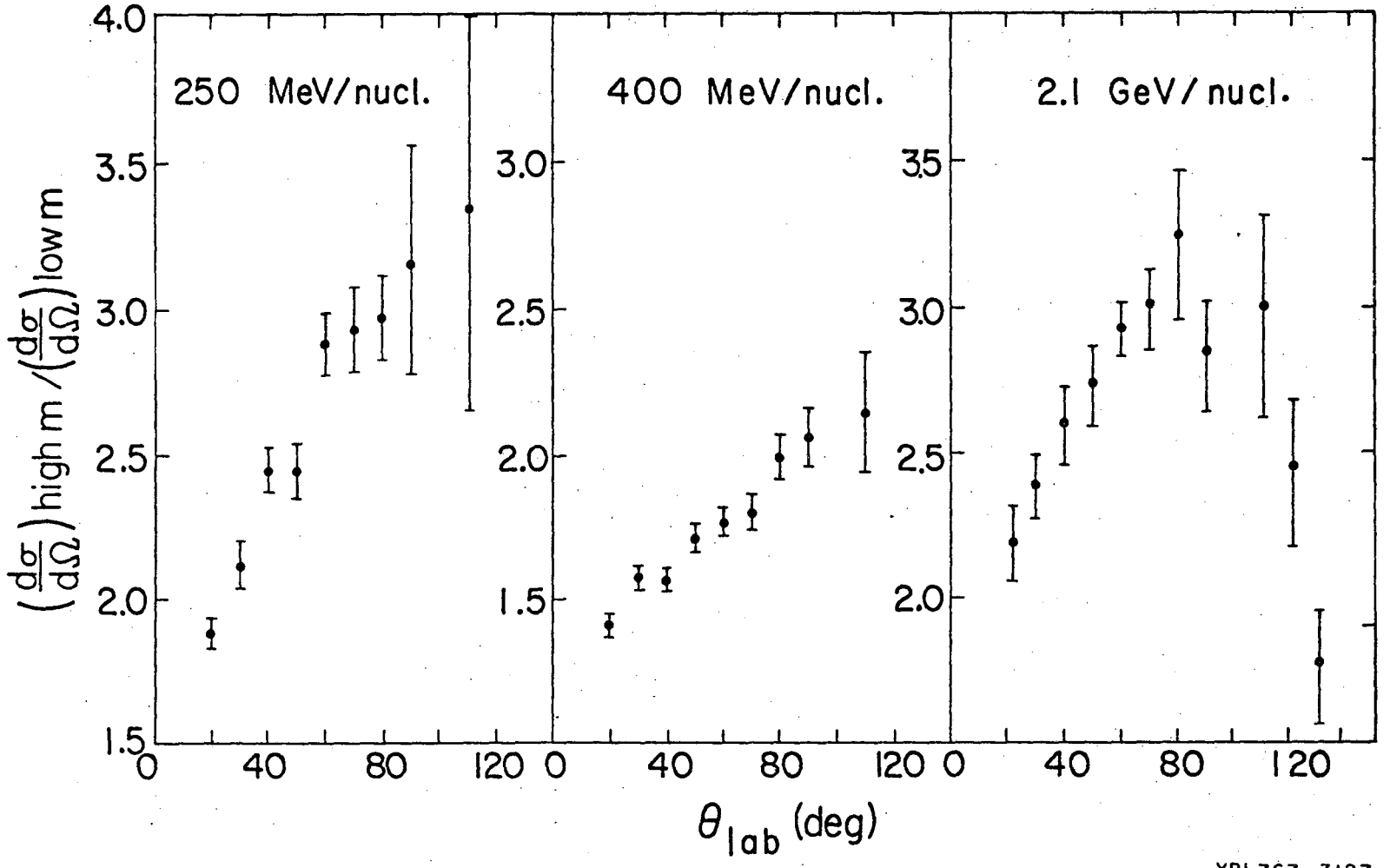

XBL767-3127

Fig. 21

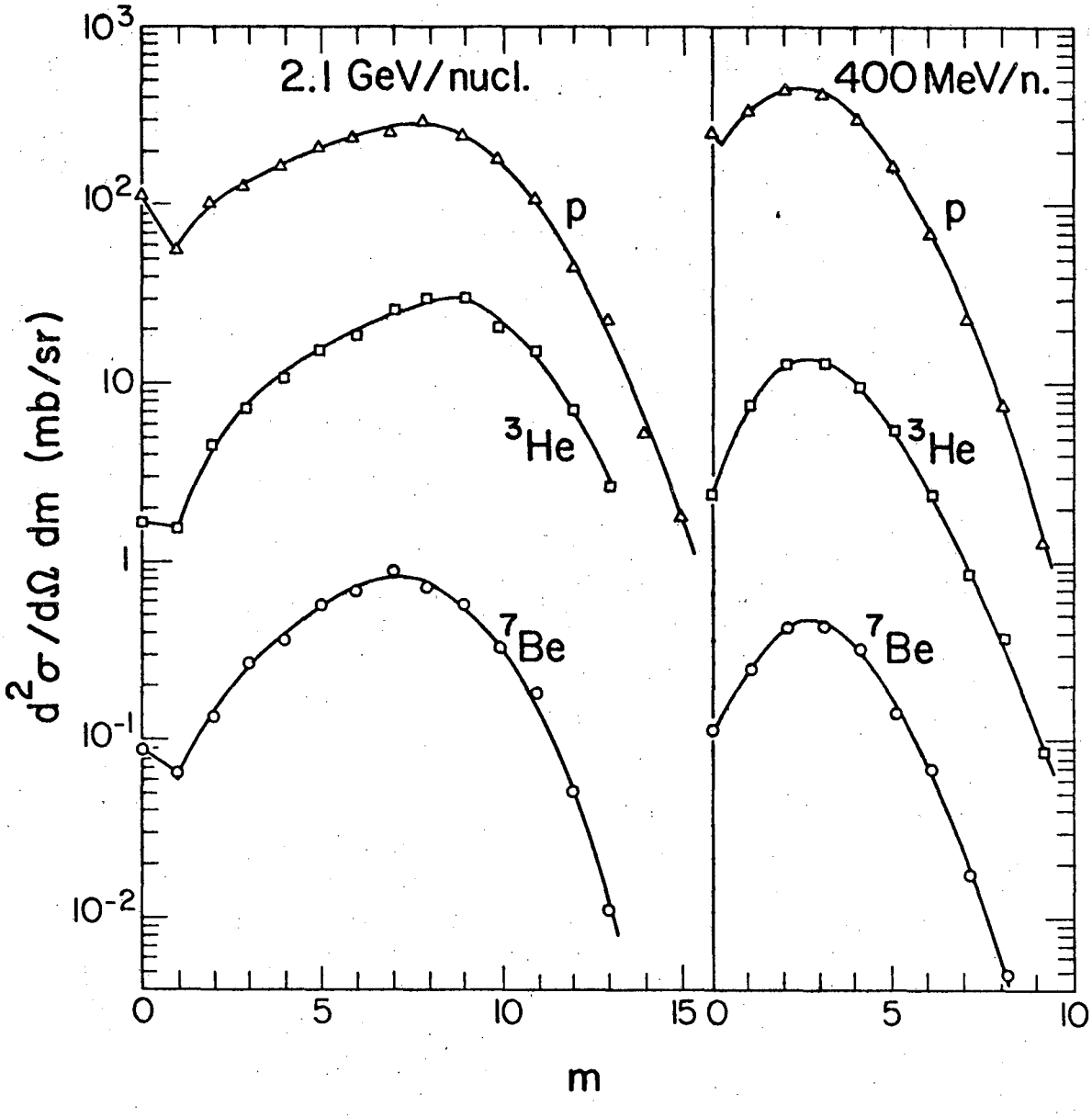

Fig. 22

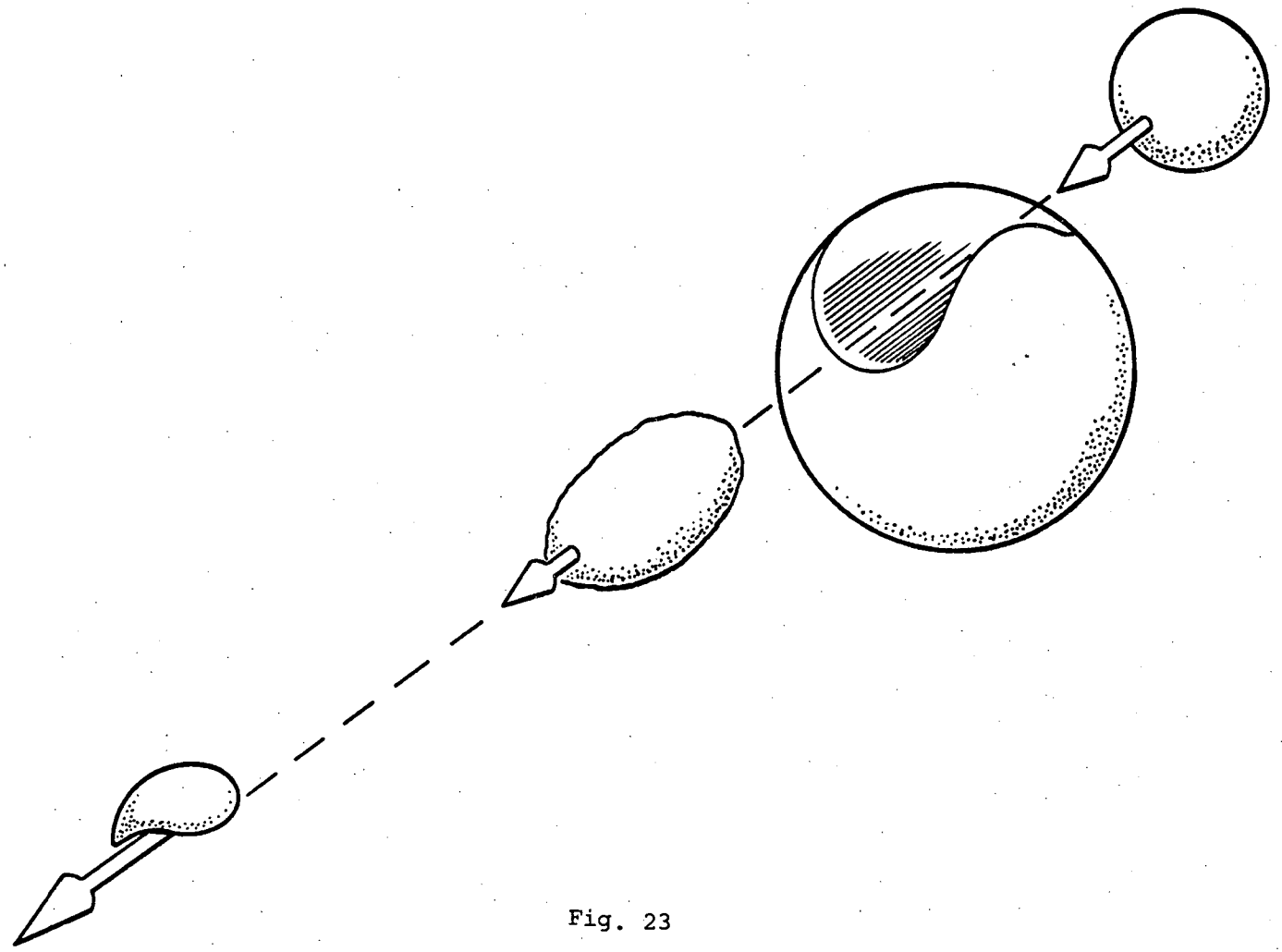

Fig. 23

XBL7610-4265

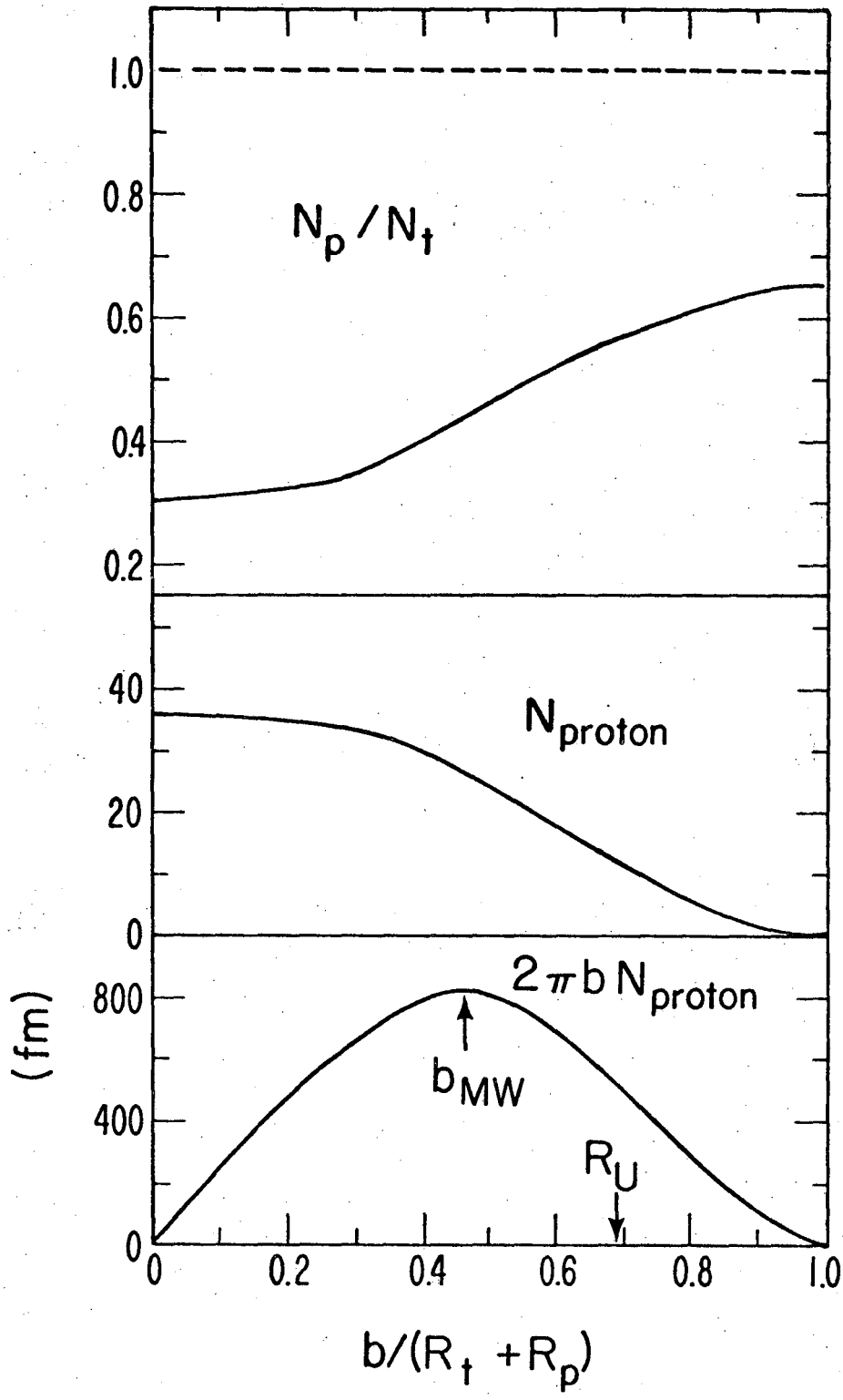

XBL 774-719

Fig. 24

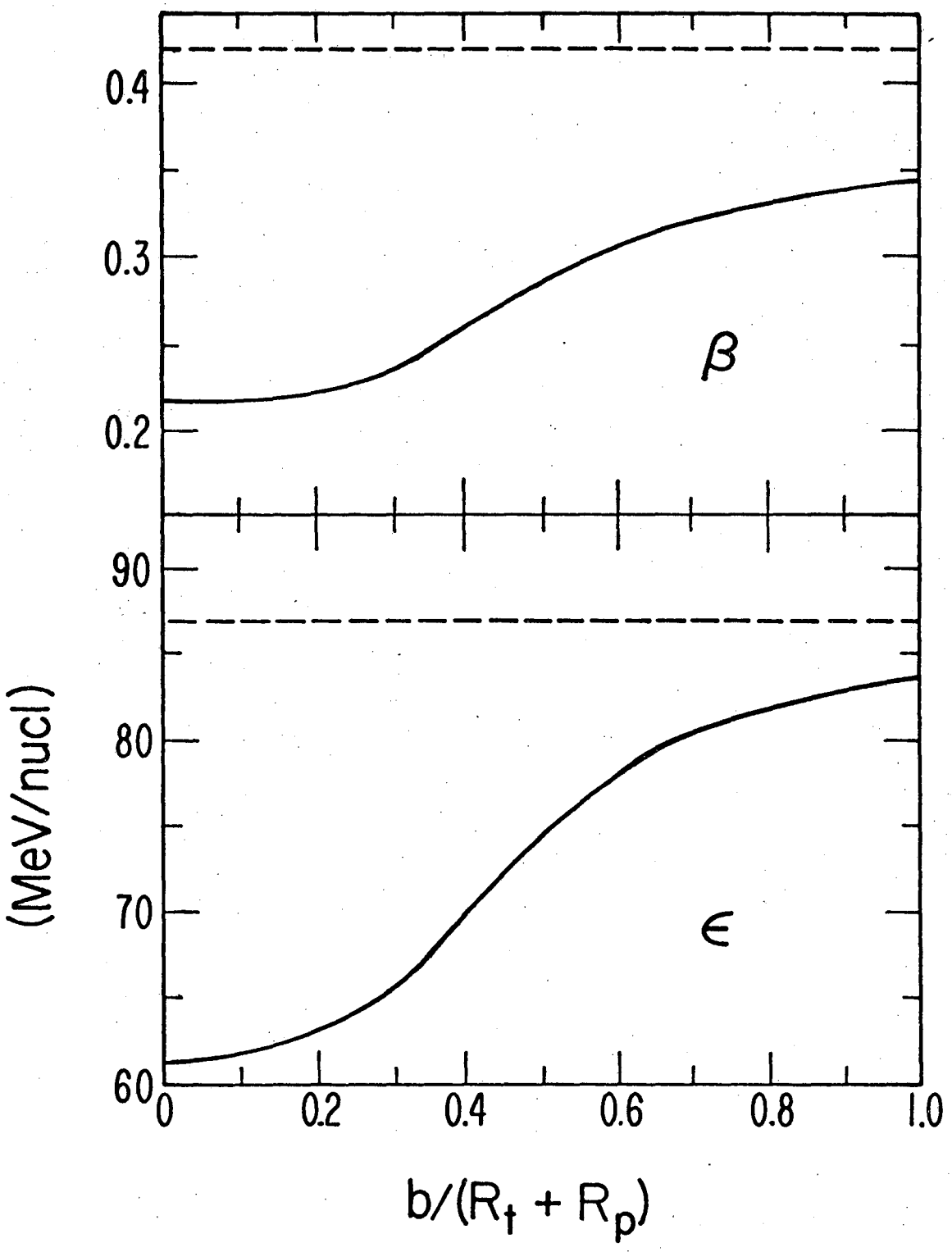

XBL 774-717

Fig. 25

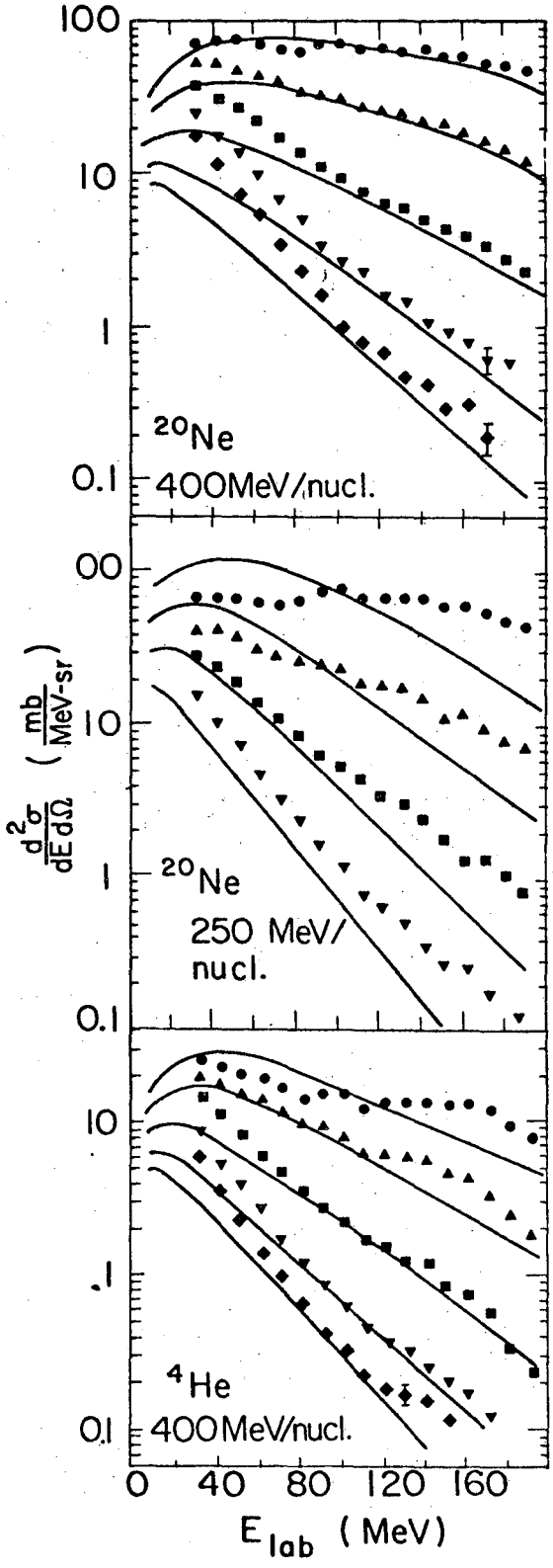

XBL 768-3873

Fig. 26

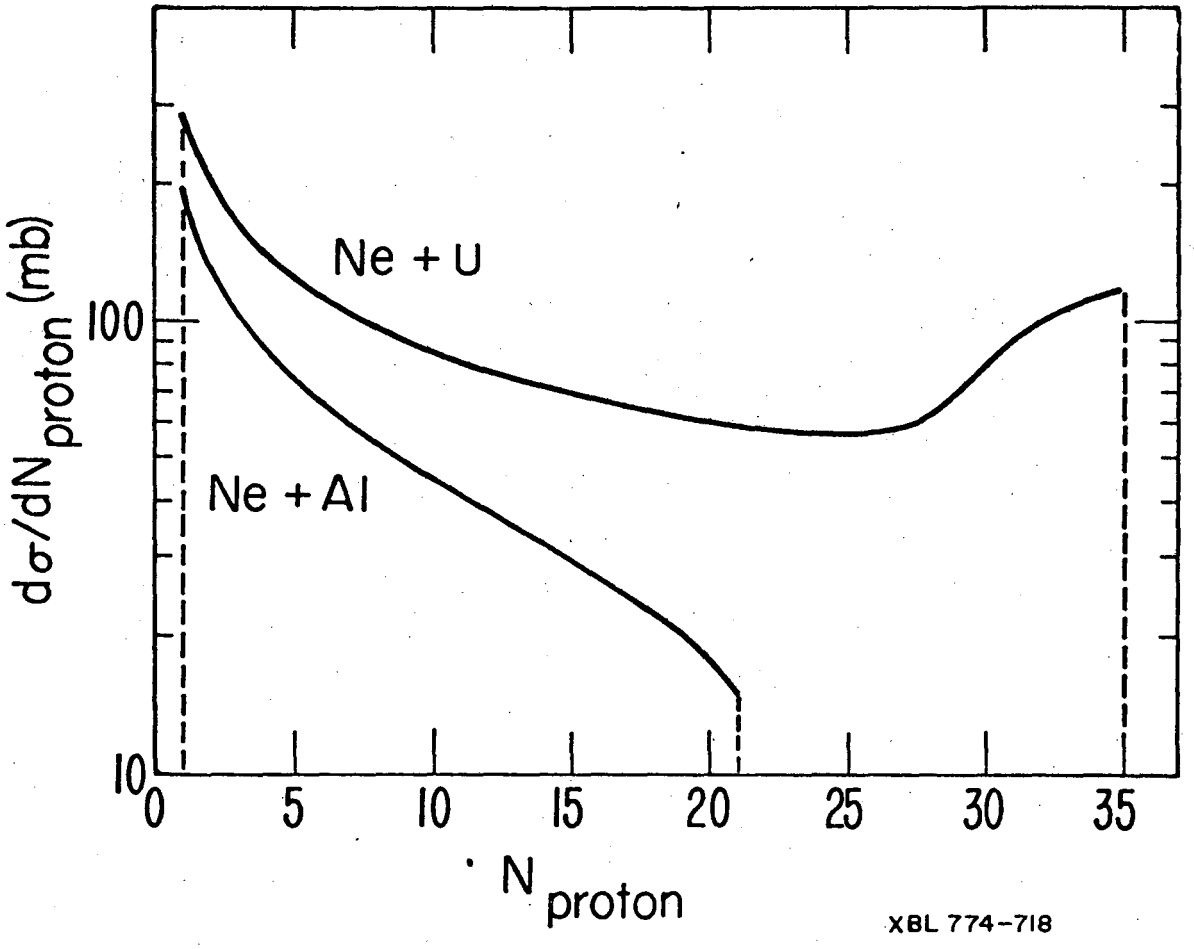
Ne + U
Ne + Al
100
10
0
5
10
15
20
25
30
35
dσ/dN proton (mb)
N proton
XBL 774-718

Fig. 27

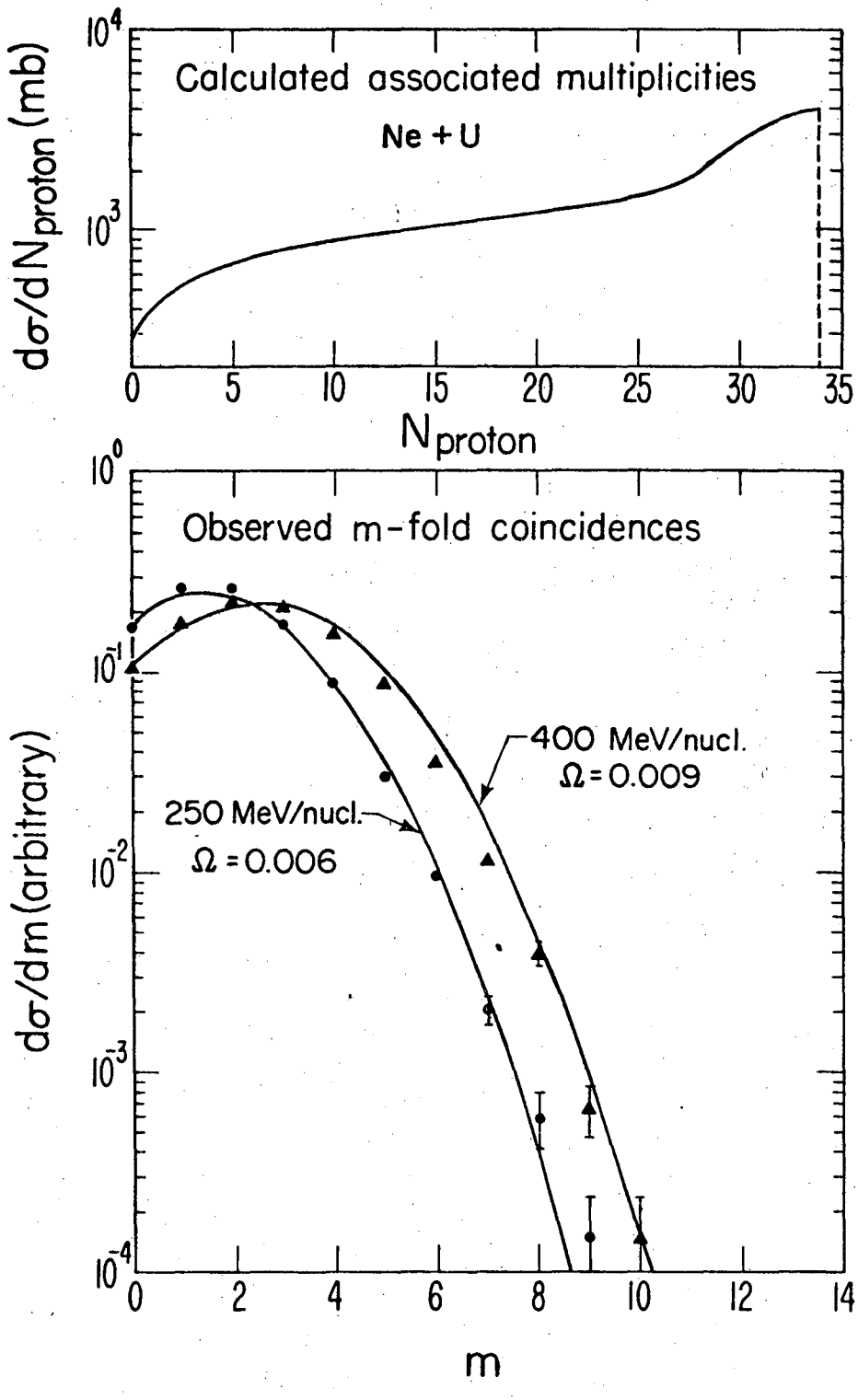

XBL 774-720

Fig. 28

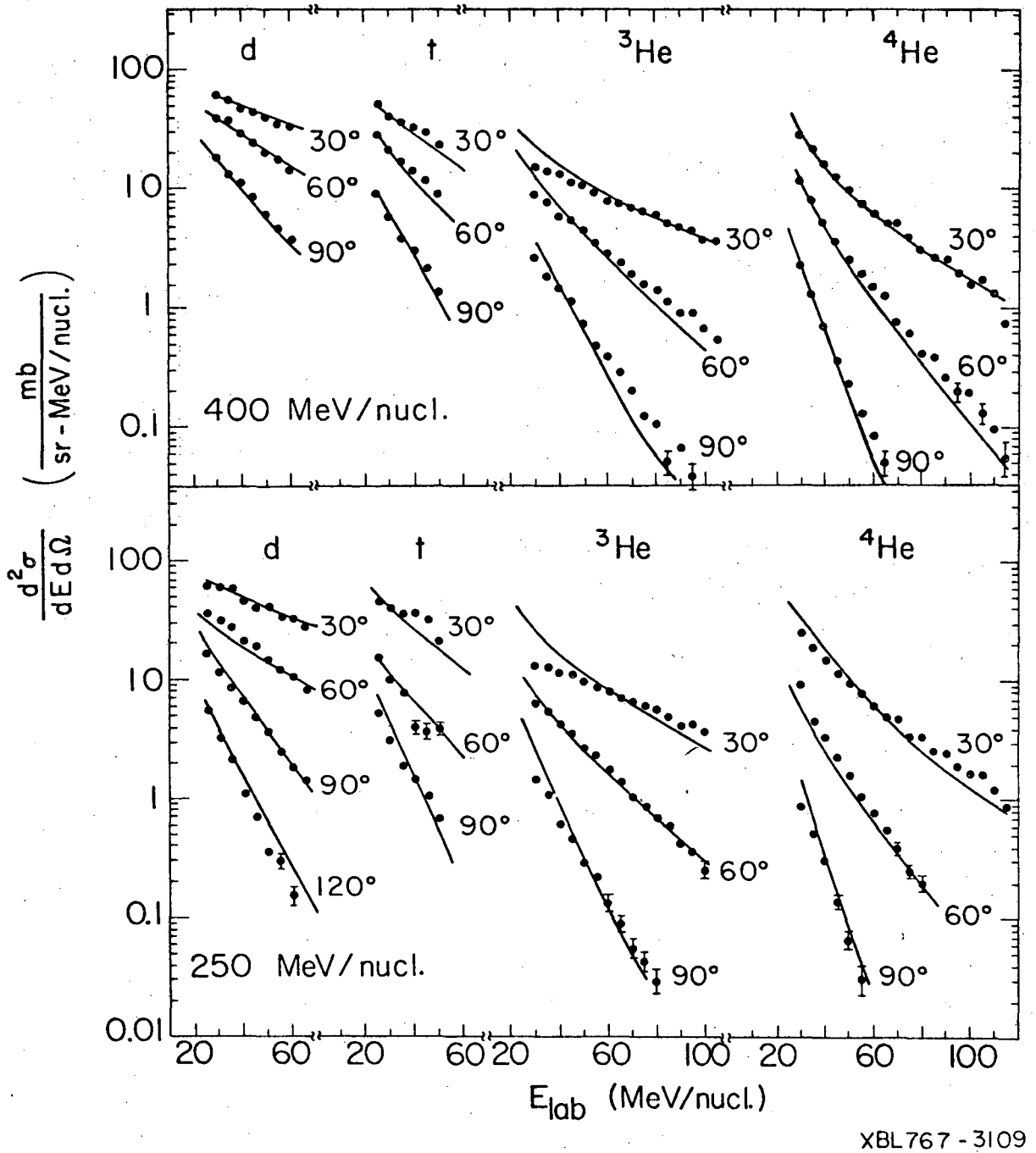
d
t
3He
4He
30°
60°
90°
120°
400 MeV/nucl.
250 MeV/nucl.
100
10
1
0.1
0.01
20
60
100
d²σ/dEdΩ (mb/sr-MeV/nucl.)
Elab (MeV/nucl.)
XBL767-3109

Fig. 29

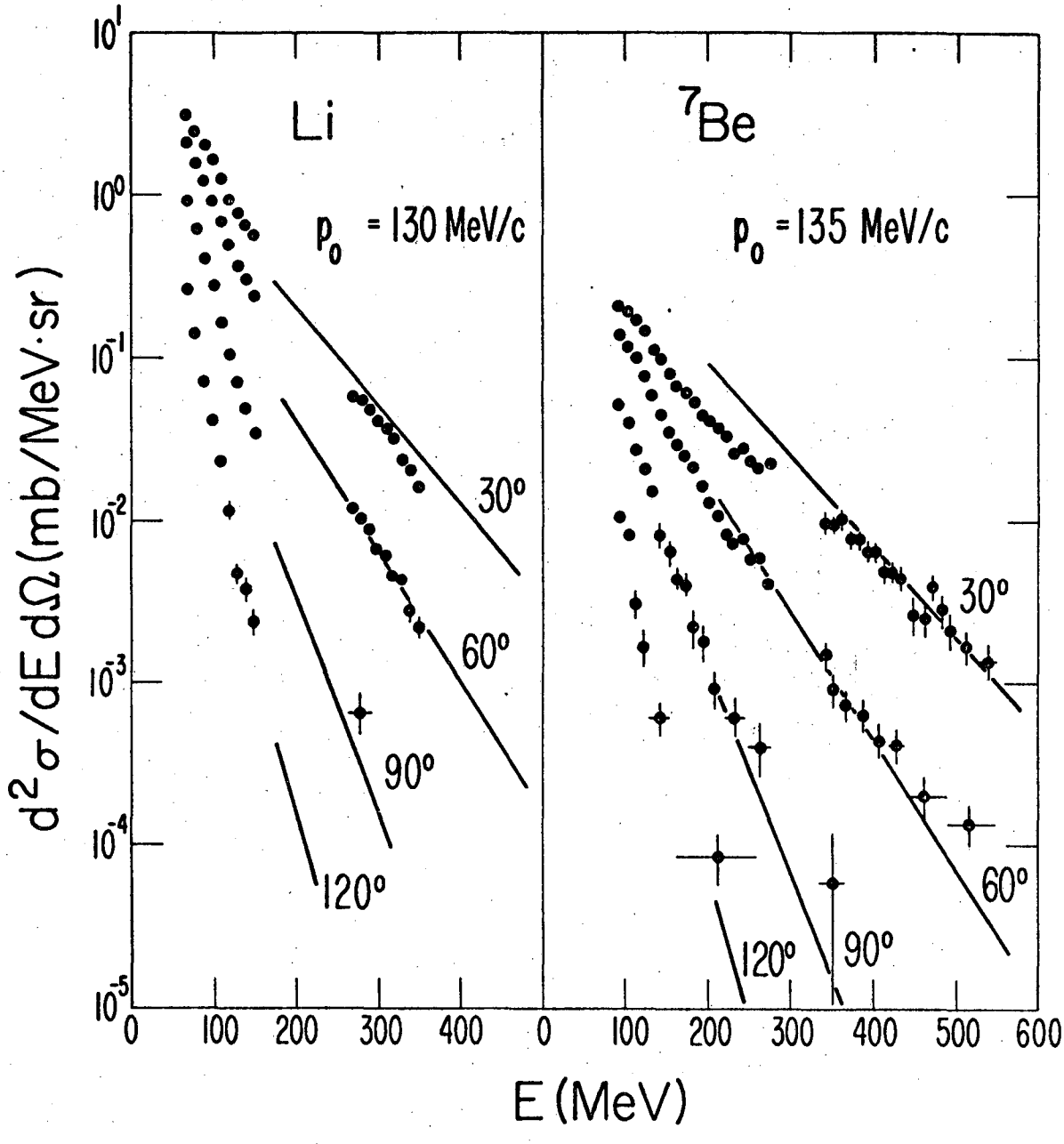

Fig. 30

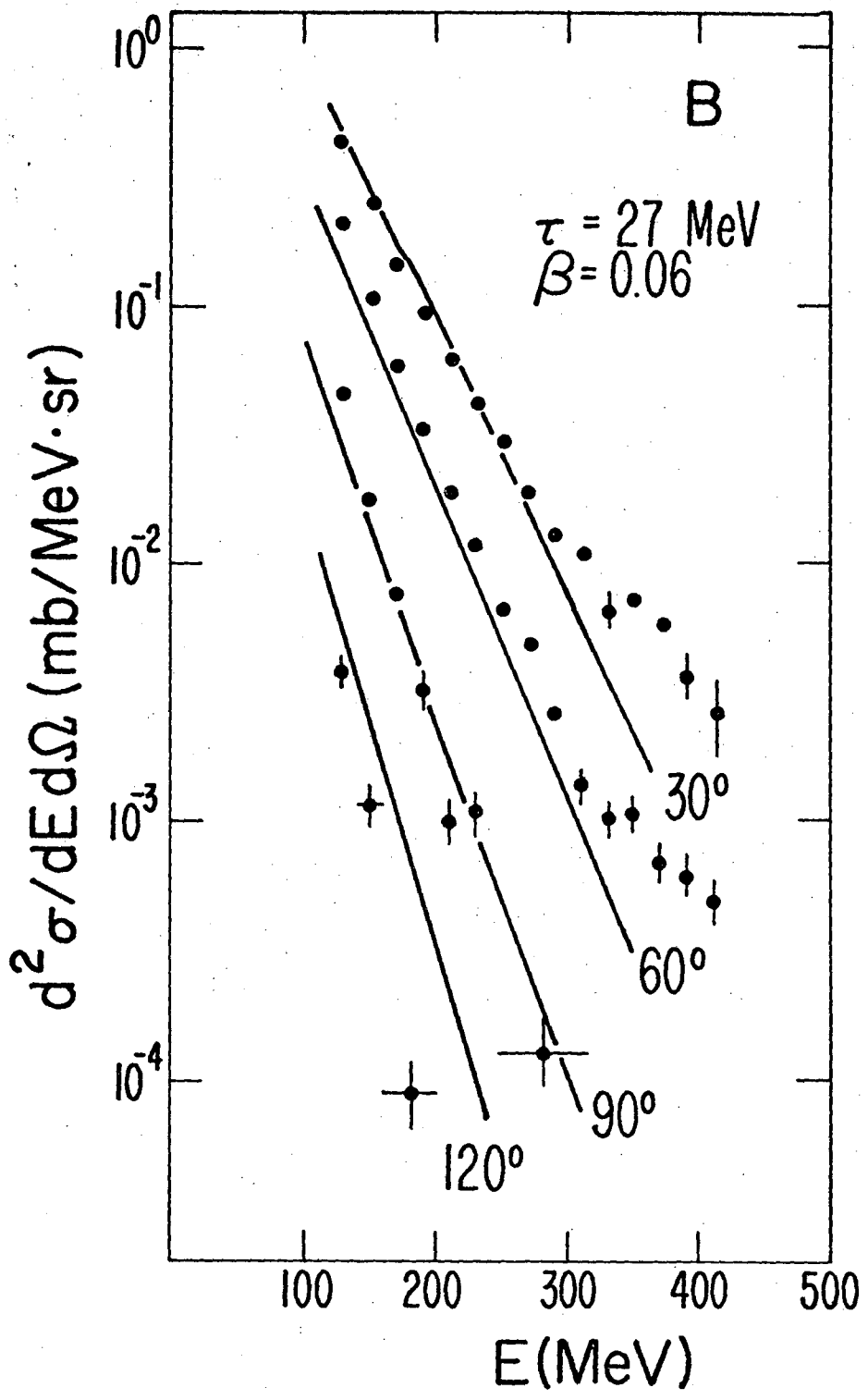

XBL 774-891

Fig. 31

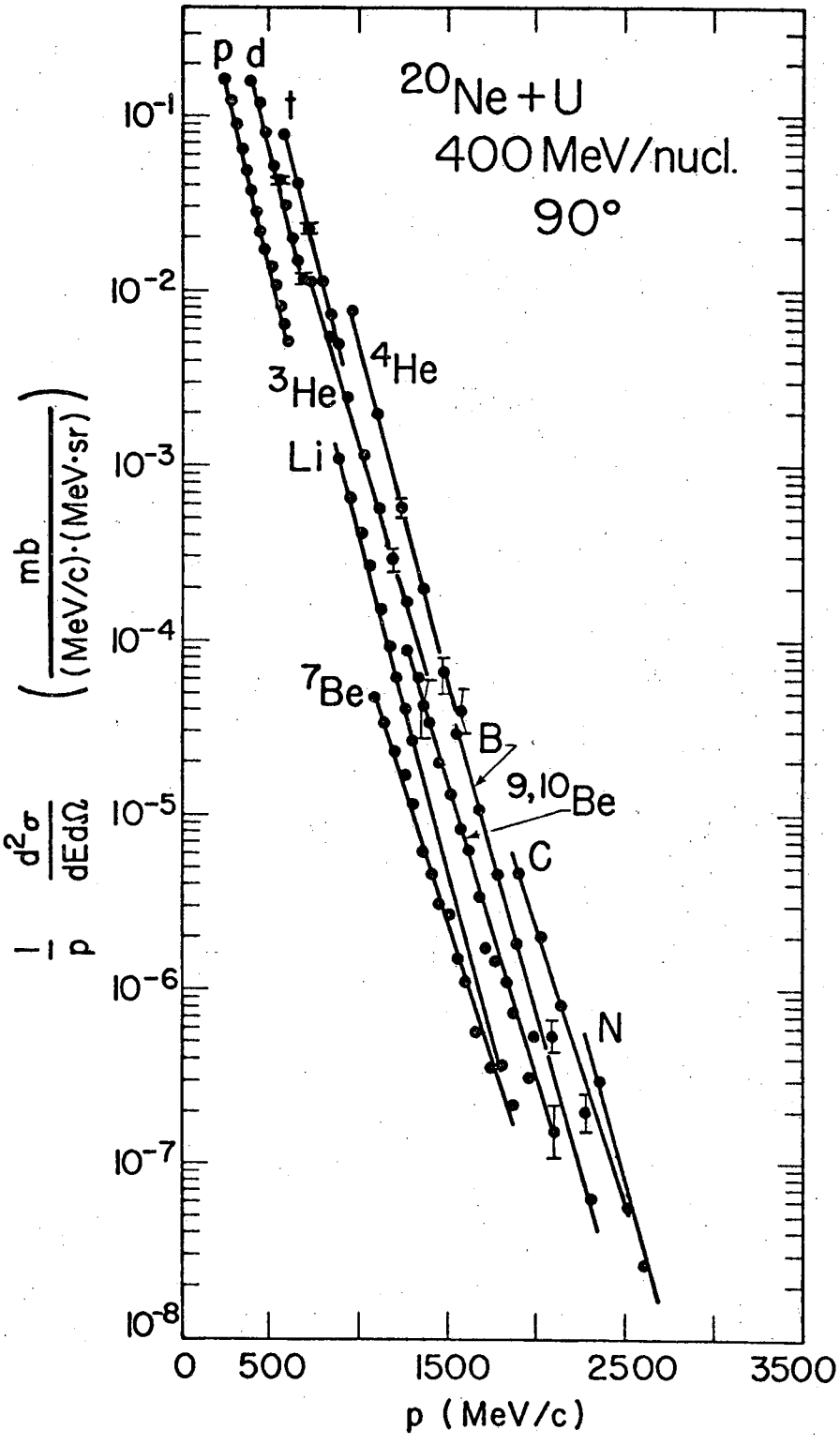

XBL 774-893

Fig. 32

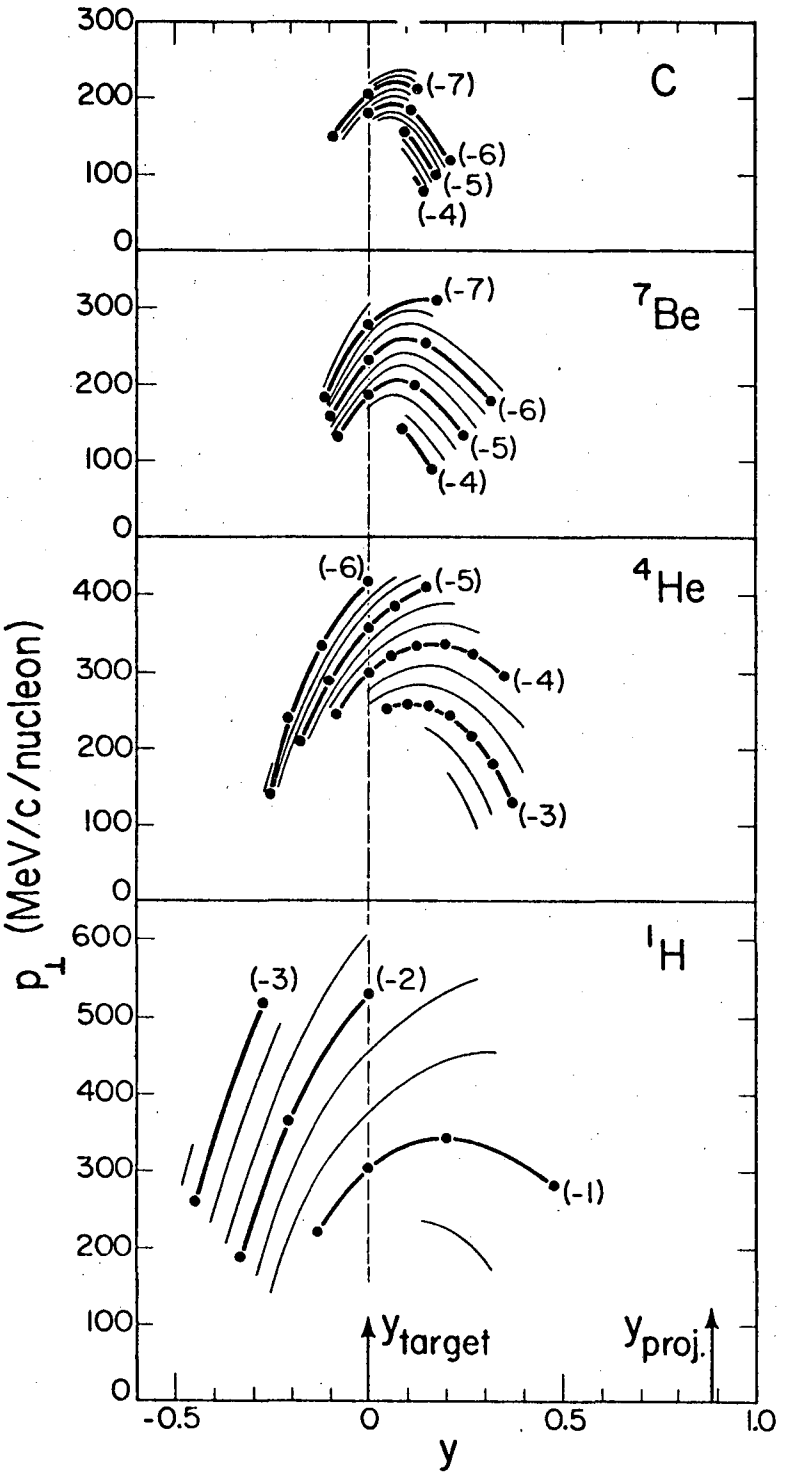
C
(-7)
(-6)
(-5)
(-4)
^{7}Be
(-7)
(-6)
(-5)
(-4)
^{4}He
(-6)
(-5)
(-4)
(-3)
^{1}H
(-3)
(-2)
(-1)
y_{target}
$y_{proj.}$
$p_\perp$ (MeV/c/nucleon)
y
XBL 775-929

Fig. 33

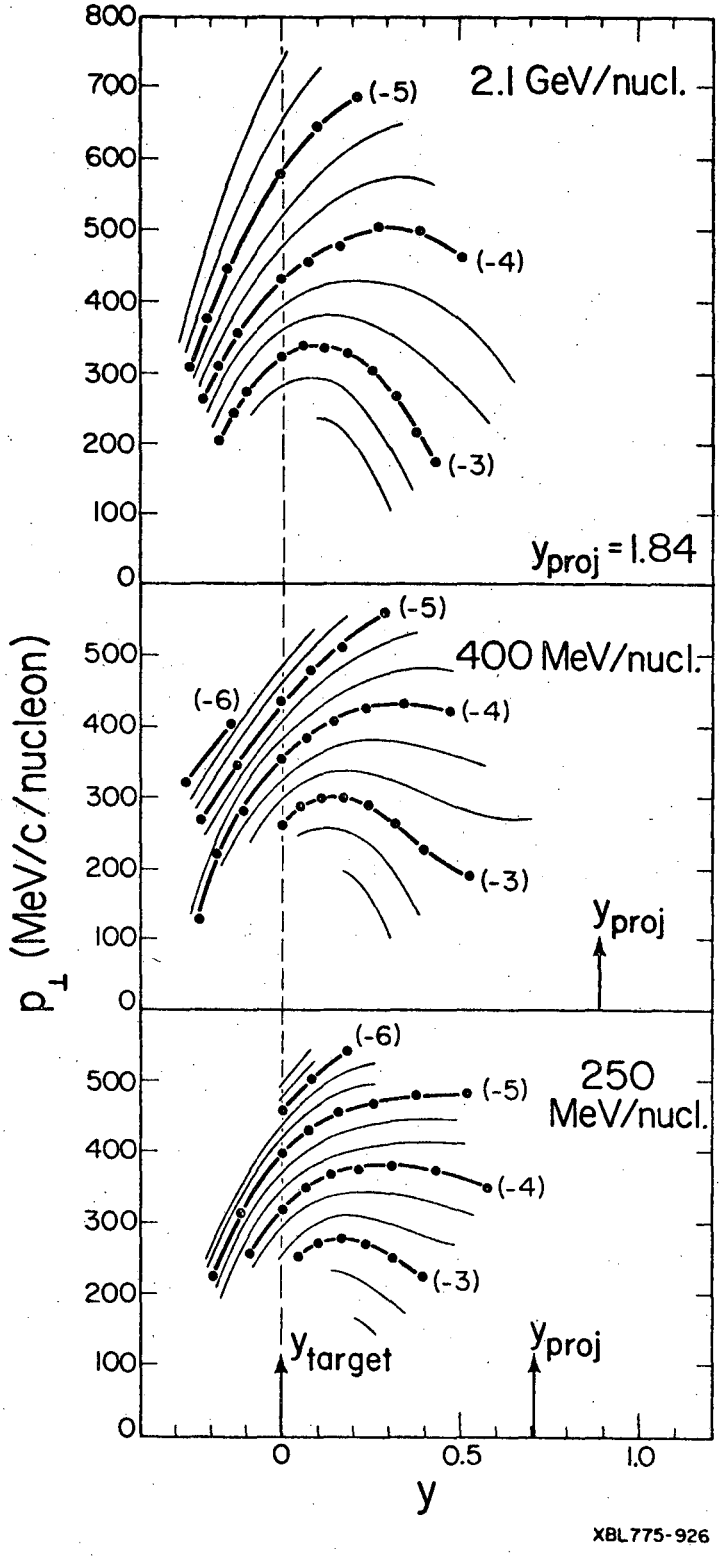

Fig. 34

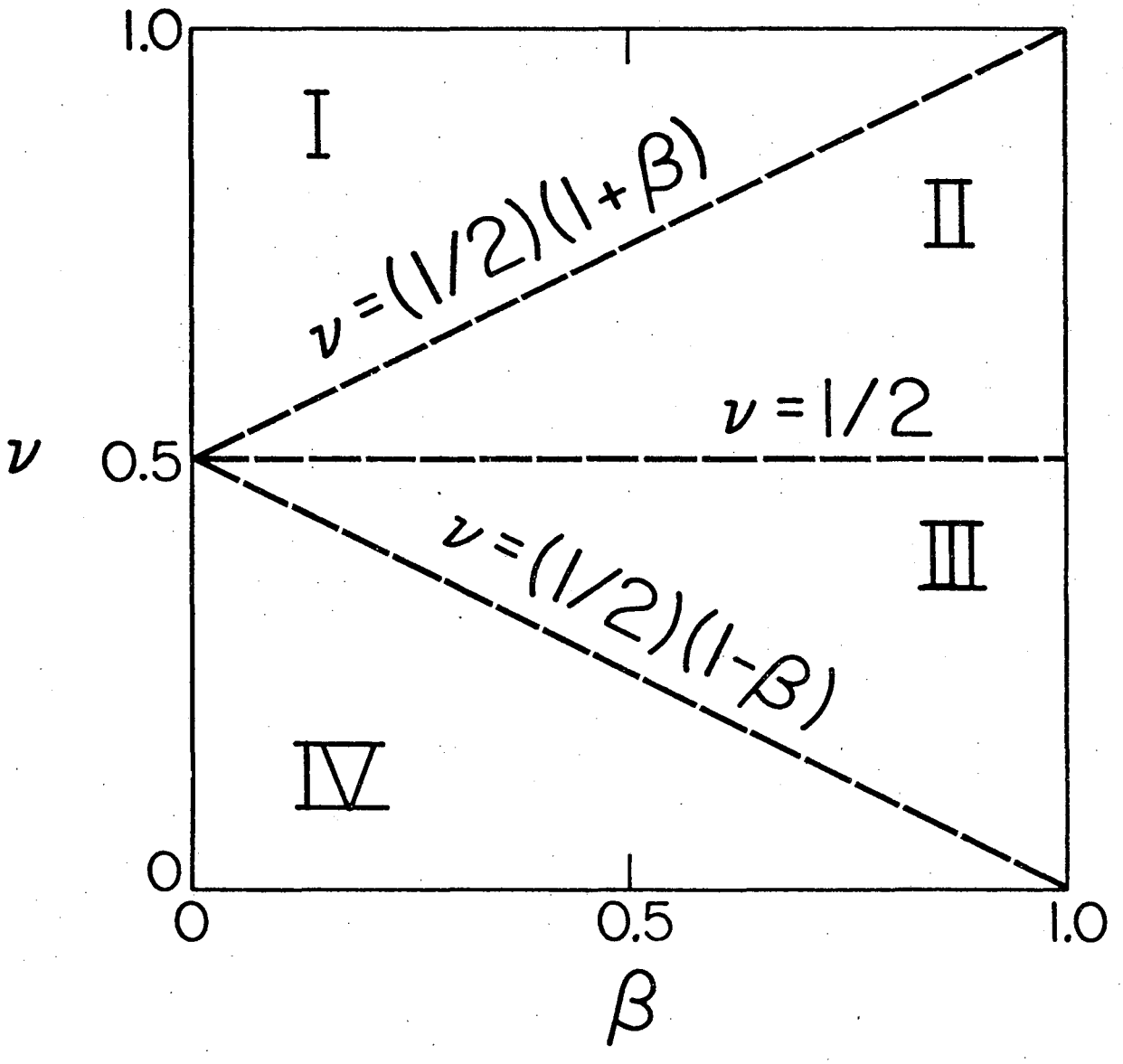

XBL775-927

Fig. 35

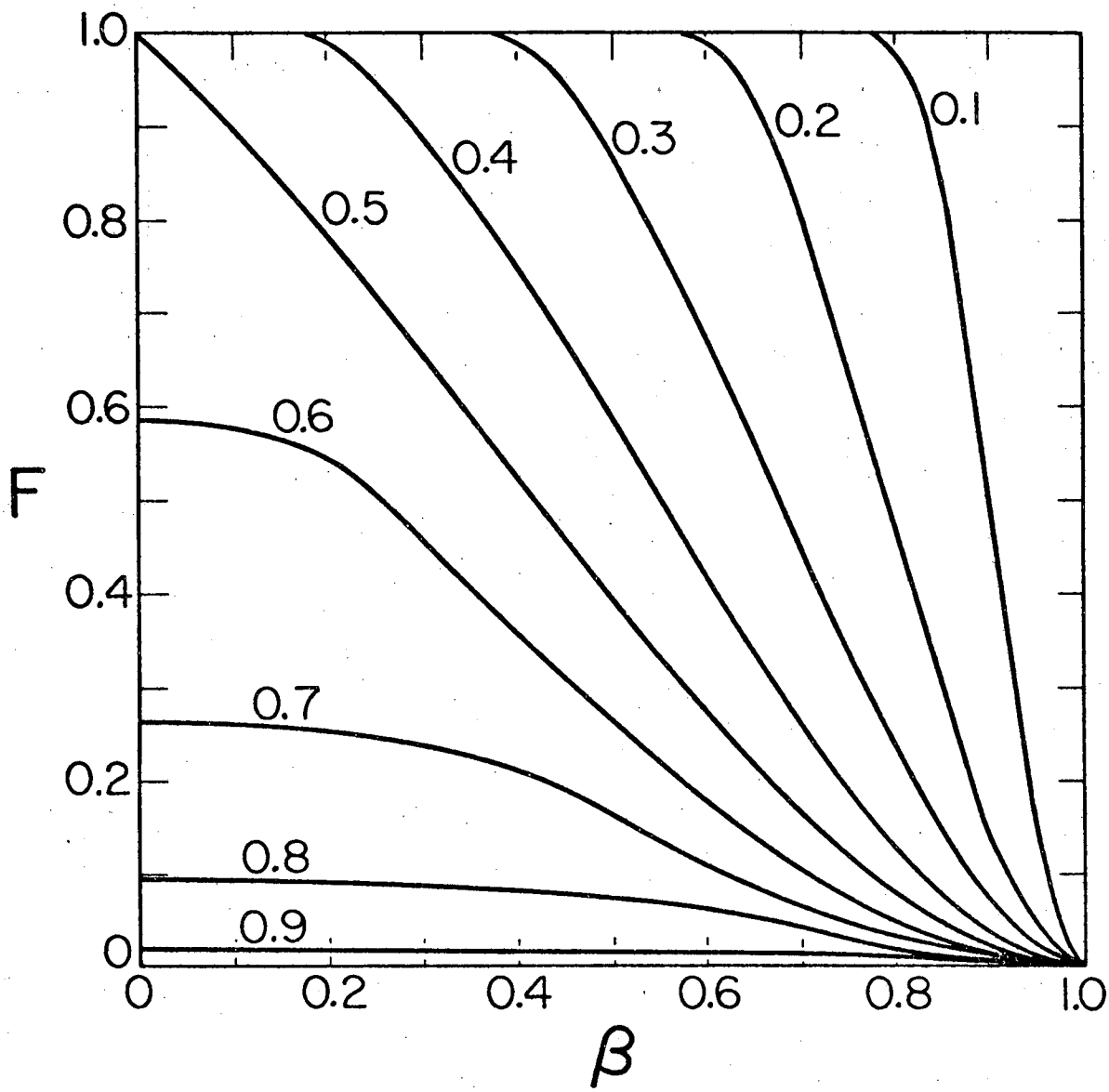

XBL 775-928

Fig. 36

TECHNICAL INFORMATION DIVISION
LAWRENCE BERKELEY LABORATORY
UNIVERSITY OF CALIFORNIA
BERKELEY, CALIFORNIA 94720